

Assembly and First Results of the KATRIN Focal-Plane Detector System at KIT

Diplomarbeit
von

Fabian Harms

An der Fakultät für Physik
Institut für Experimentelle Kernphysik (IEKP)

Erstgutachter: Prof. Dr. Guido Drexlin
Zweitgutachter: Prof. Dr. Günter Quast
Betreuer Mitarbeiter: Dr. Markus Steidl

Bearbeitungszeit: 01. Juli 2011 – 30. Juni 2012

Erklärung

Hiermit versichere ich, die vorliegende Arbeit selbstständig angefertigt, alle dem Wortlaut oder Sinn nach entnommenen Inhalte anderer Werke an den entsprechenden Stellen unter Angabe der Quellen kenntlich gemacht und keine weiteren Hilfsmittel verwendet zu haben.

Fabian Harms, Juni 2012

Zusammenfassung

Das Neutrino wurde 1930 von Pauli als Spin-1/2 Teilchen postuliert, um die Energie- und Impulserhaltung im radioaktiven β -Zerfall zu gewährleisten. Aufgrund seiner schwachen Wechselwirkung mit Materie, dauerte es 26 Jahre bis es von Reines und Cowan im „Poltergeist Experiment“ nachgewiesen werden konnte. Bis heute erfordert die Untersuchung seiner Eigenschaften sehr präzise Experimente, wodurch die absoluten Massen der drei bekannten Neutrinogenerationen nach wie vor nur in Grenzen bekannt sind. Durch die Entdeckung der Neutrinooszillationen im Superkamiokande-Detektor 1998, wurde klar, dass sich die Eigenzustände der schwachen Wechselwirkung von den Masseneigenzuständen der Neutrinos unterscheiden. Sie sind vielmehr eine Superposition dieser, was zu Oszillationen zwischen den Neutrinogenerationen führt. In weiteren Experimenten konnten die Parameter der Oszillationen inzwischen gut vermessen werden. Jedoch lässt sich anhand dieser nur eine Aussage über die Massendifferenzen zwischen den Neutrino-Masseneigenzuständen machen. Um die Absolutmassen der Neutrinos zu bestimmen, gibt es diverse unterschiedliche Möglichkeiten. Hierbei sind jedoch die meisten Ansätze modellabhängig, d.h. sie setzen gewisse theoretische Modelle zur Massenhierarchie der Neutrinos, zu ihren grundlegenden Eigenschaften (Majorana vs. Dirac Teilchen) oder auch zu ihrer Entstehung in Supernovae voraus. Neben diesen modellabhängigen Messungen besteht die Möglichkeit, die Masse des Elektron-Antineutrinos aus der Form des β -Zerfallsspektrums modellunabhängig zu bestimmen. Eine nichtverschwindende Neutrinomasse beeinflusst das Energiespektrum der beim Zerfall entstehenden β -Elektronen nahe der Endpunktsenergie E_0 . Diese Nachweismethoden setzen keine theoretischen Modelle zur Beschaffenheit der Neutrinos voraus und erlauben eine Bestimmung ihrer Masse einzig über die Annahme der Energie- und Impulserhaltung. Die bekanntesten Experimente dieser Art nutzen den β -Zerfall von molekularem Tritium und untersuchen das β -Spektrum mit Hilfe von Retardierungsspektrometern, die auf dem MAC-E-Filter-Prinzip (Magnetic Adiabatic Collimation) basieren. Die genaueste Obergrenze für die Masse des Elektron-Antineutrinos bis zum heutigen Tag wurde so durch Experimente in Mainz und Troitsk gefunden:

$$m_{\bar{\nu}_e} < 2,0 \text{ eV/c}^2 \quad (95\% \text{ C.L.}) \quad (1)$$

Das Karlsruher TRIitium Neutrino (KATRIN) Experiment hat sich zum Ziel gesetzt, die Sensitivität dieser Experimente um eine Größenordnung auf $m_{\bar{\nu}} \leq 200 \text{ meV/c}^2$ (90% C.L.) zu übertreffen. Hierfür nutzt KATRIN eine fensterlose gasförmige Tritiumquelle (WGTS), aus der die β -Elektronen des Tritiumzerfalls magnetisch-adiabatisch über eine Transportstrecke in zwei Retardierungsspektrometer geführt werden. Die Transportstrecke besteht

aus einer differentiellen Pumpstrecke (DPS2-F) und einer kryogenen Pumpstrecke (CPS), welche den Gasfluss des Tritiums von der Quelle in die Spektrometer um einen Faktor 10^{12} reduzieren. Das magnetische Führungsfeld der Elektronen wird über die gesamte Länge des Experiments durch supraleitende Solenoide bereitgestellt, welche einen magnetischen Flussschlauch von 191 Tcm^2 definieren. Das erste (Vor-) Spektrometer sortiert die β -Elektronen aus der Quelle vor; Nur Elektronen mit kinetischen Energien 200 eV nahe der Tritium-Endpunktsenergie von 18,6 keV können seine Analysierebene passieren. Das anschließende Hauptspektrometer misst die „longitudinale“ kinetische Energie der Elektronen mit einer Auflösung von:

$$\Delta E = 0,93 \text{ eV} \quad (2)$$

Hinter dem Hauptspektrometer bestimmt ein Fokalebenen-Detektor (FPD) die Anzahl der Elektronen, die die Analysierebene des Hauptspektrometers bei einer gegebenen Retardierungsspannung überwinden können. In Folge der Hoch-Energie-Pass-Funktion des Spektrometers misst der FPD ein integriertes β -Spektrum des Tritiumzerfalls. Trotz der unübertroffenen Rate von $10^{11} \beta$ -Elektronen pro Sekunde, die in der WGTS entstehen, trägt nur ein Anteil von $2 \cdot 10^{-13}$ der Elektronen im Bereich 1 eV nahe des Endpunktes zum β -Spektrum bei. Daraus resultiert auf dem FPD eine Zählrate von wenigen mHz auf dem FPD. Deshalb ist eine hohe Untergrundreduzierung die Hauptherausforderung von KATRIN. Zudem muss der FPD eine hohe Detektionseffizienz für keV-Elektronen vorweisen, um die statistischen Unsicherheiten des Experiments zu minimieren. Das FPD-System wurde von den KATRIN-Kooperationspartnern in Seattle (Washington, USA) entwickelt, gebaut und auf seine Anforderungskriterien hin getestet. Nach dem Transport zum KATRIN-Experiment an den Campus Nord des Karlsruher Instituts für Technologie (KIT), wurde es im Rahmen dieser Diplomarbeit gemeinsam mit den amerikanischen Kollegen aufgebaut und auf seine Leistungsfähigkeit getestet. Zudem wurden in einer Messperiode im Frühjahr 2012 Daten mit dem System genommen. Erste Ergebnisse anhand der Daten werden in dieser Arbeit präsentiert und zum Teil mit Monte-Carlo-Simulationen verglichen.

Abbildung 1 gibt einen Überblick über die verschiedenen Untersysteme des FPD, deren Funktion und Betriebsverhalten am KIT wie folgt zu beschreiben ist:

- **Magnete:**

Das magnetische Führungsfeld der β -Elektronen wird innerhalb des FPD-Systems durch zwei supraleitende Solenoide erzeugt. Zum einen dem Pinch Magneten am Ende des Hauptspektrometers, der eine nominelle magnetische Flussdichte von 6 T liefert, und zum anderen dem Detektor Magnet, der ebenfalls ein Feld von 6 T erzeugen kann, im Normalbetrieb aber nur 3,6 T liefert. Abgesehen von einem, vermutlich durch den vorhergehenden Transport bedingten Quench des Detektor Magneten direkt nach seiner Inbetriebnahme im Sommer 2011, laufen die Magnete am KIT stabil. Sie wurden beide gemeinsam auf 6 T betrieben. Zudem wurde die magnetische Flussdichte in der offenen Bohrung des Pinch Magneten (Pinch Magnet bei 6 T und Detektor Magnet bei 3,6 T) mit Hilfe einer nuklearmagnetischen Resonanzprobe auf ihre Stabilität hin untersucht. Dabei wurde ein Abfall des Feldes von 0,0015% pro Monat im fortlaufenden autonomen Betrieb gemessen, deutlich geringer als die Designanforderung von 0,1% pro Monat.

- **Vakuum System:**

Um die Wahrscheinlichkeit einer Streuung der β -Elektronen mit Restgas zu minimieren, wird der Druck in den Spektrometern und im Strahlrohr des FPD-Systems auf 10^{-11} mbar (Ultrahochvakuum) reduziert. Dies geschieht im Falle des Detektor-Systems mit Hilfe einer Kryo- und einer Turbomolekularpumpe. Am KIT wurde so ein Druck von $3 \cdot 10^{-10} \text{ mbar}$ erreicht. Es ist absehbar, dass der Zieldruck nach der

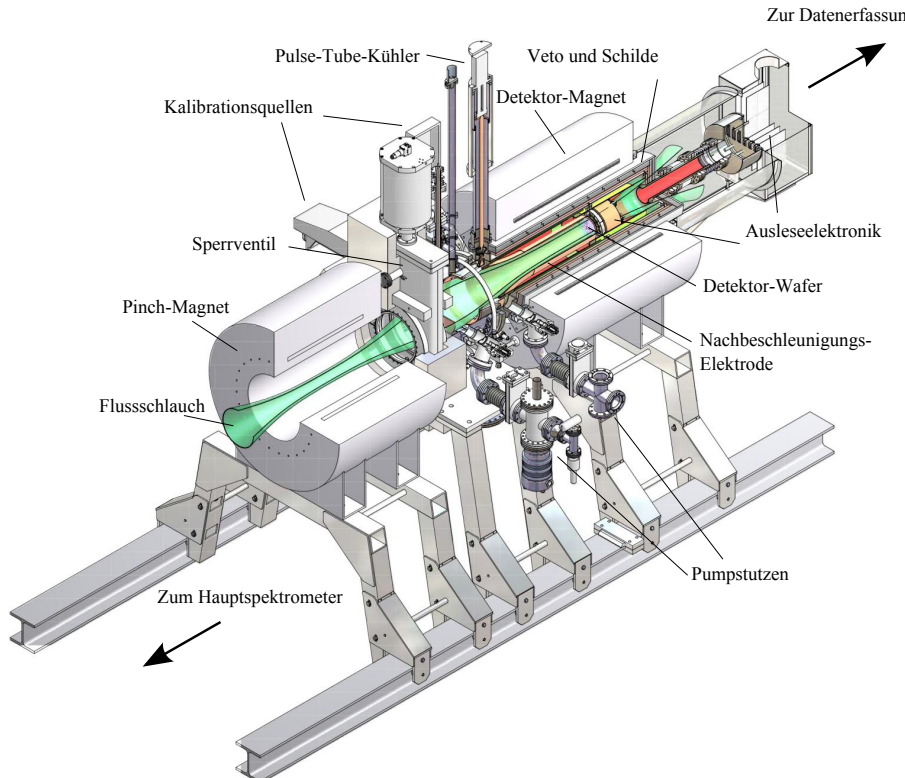


Abbildung 1.: Schematische Darstellung des FPD-Systems [1] (mod.) .

Installation verschiedener Upgrades des Systems und nach einem längeren Ausheizen des Strahlrohrs im Sommer 2012 erzielt wird. Die Ausleseelektronik des Detektors befindet sich, räumlich vom Detektor-Wafer getrennt, in einer zweiten Vakuumkammer, die das Strahlrohr umschließt. In dieser wurde der Zieldruck von 10^{-6} mbar (Hochvakuum) bereits erreicht.

- **Nachbeschleunigungs-Elektrode:**

Da in dem für KATRIN relevanten Energieband nahe des Tritium Endpunktes von 18,6 keV mehrere Fluoreszenz-Linien zu erwarten sind, ist eine Nachbeschleunigungs-Elektrode im FPD-System verbaut. Sie bildet die Wand zwischen den zwei Vakuumkammern und erlaubt es, das relevante Energieband um bis zu 30 keV zu höheren Energien zu verschieben. Am KIT war ein stabiler Betrieb der Elektrode bislang nur bei Spannungen bis 8 kV möglich. Darüber kam es zu Spannungsoverschlägen. Beim Einbau der Upgrades des Systems wurde als Grund für diese Überschläge ein loses Gasket ausgemacht und beseitigt. Zudem wurde die durch hohe mechanische Beanspruchung verformte Elektrode durch eine neue, mechanisch Robustere ersetzt. Daher ist davon auszugehen, dass nach der erneuten Inbetriebnahme des Systems im Sommer 2012 Spannungen bis zu 30 kV möglich sind.

- **Kühlsystem:**

Um die Restströme im Detektor-Wafer möglichst klein zu halten und ein Überhitzen der Ausleseelektronik zu vermeiden, wird diese, wie auch der Wafer und die Nachbeschleunigungs-Elektrode, mittels eines Pulse-Tube-Kühlers aktiv gekühlt. Während der Wafer in Seattle so bei Temperaturen von ~ 0 °C betrieben wurde, war am KIT eine höhere Temperatur von ~ 10 °C festzustellen. Die Operationsverstärkermodule waren im normalen Betriebsmodus ~ 40 K wärmer als in Seattle. Bei Messungen zum Wärmeeintrag der Ausleseelektronik in das Vakuumsystem wurde eine erhöhte Leistung von 17,4 W im Vergleich zum Designwert von 15 W gefunden.

den. Da bei der Installation des FPD-Systems am KIT eine neue Generation von Operationsverstärkernmodulen verbaut wurde, liegt die Ursache für den höheren Wärmeeintrag vermutlich in deren Betriebsverhalten. Die Module werden im Laufe der Installation der Systemupgrades durch neue ersetzt, wodurch eine Verringerung des Wärmeeintrags nach erneuter Inbetriebnahme des Systems zu erwarten ist. Zudem wird das Kühlssystem des FPD aufgrund der höheren Wärmekapazität der neuen Nachbeschleunigungselektrode durch ein leistungsfähigeres System ersetzt.

- **Detektor und Ausleseelektronik:**

Der Detektor des FPD-Systems besteht aus einer in 148 Pixel segmentierten PIN-Diode, auf Basis eines einzigen n-intrinsisch dotierten Silizium-Wafers. Der Wafer hat eine Dicke von $503\ \mu\text{m}$ und, inklusive eines Vorspannungs- und eines Abschirm-Rings, einen Durchmesser von 125 mm. Seine sensitive Fläche hat eine Ausdehnung von 90 mm, was gerade dem Querschnitt des magnetischen Flussschlauches am Ort des Wafers entspricht. Die vom Hauptspektrometer kommenden β -Elektronen treffen auf die nicht-segmentierte, n++ dotierte Frontseite des Wafers, während die Segmentation auf seiner Rückseite in Form von p-dotierten, mit nicht-oxidierendem TiN überzogenen Pixeln realisiert ist. Je zwölf der flächengleichen Pixel ($44\ \text{mm}^2$) sind in konzentrischen Kreisen angeordnet. Im Zentrum des Wafers befinden sich weitere vier sogenannte „Bulls-Eye“ Pixel. Um den elektrischen Kontakt mit der Ausleseelektronik zu realisieren, pressen mit Gold überzogene, sogenannte „Pogo-Pins“ von der Rückseite auf den Wafer. Diese sind wiederum mit 184 ebenfalls mit Gold überzogenen Pins verbunden, die mit L21-Borosilikatglas in einen Durchführungsflansch eingefasst sind. Dieser trennt den Ultrahochvakuumbereich des Strahlrohrs von der Hochvakuumkammer mit der Ausleseelektronik. Er garantiert so eine niedrige Kapazität sowie eine Unterdrückung der Kontaktmikrophonie zwischen dem Wafer und den Operationsverstärkern. Um β -Elektronen, die durch radioaktive Zerfälle in den Glasdurchführungen entstehen, vom Wafer abzuschirmen, wurden kleine Kupferschilde, sogenannte „DONUTS“ entwickelt, welche über die Pogo-Pins geführt werden können. Nach ihrer Installation im Sommer 2012 wird eine Reduzierung des intrinsischen Detektoruntergrunds bis zu einer Größenordnung erwartet. Auf der Rückseite des Durchführungsflansches sind die Pin-Durchführungen direkt mit den 24 Operationsverstärkernmodulen verbunden, die kreisförmig angeordnet sind und die Signale von sechs bzw. sieben Detektorpixeln verstärken. Hinter diesen Modulen befinden sich zwei kreisförmige Verteilerdecks, von denen aus die verstärkten Detektorsignale über einen Kabelbaum zu einem weiteren Durchführungsflansch geleitet werden. Dieser verbindet die Hochvakuumkammer mit der Atmosphärenseite, wo die Signale in einer weiteren Stufe nochmals verstärkt werden. Da die bis zu diesem Punkt beschriebene Ausleseelektronik auf dem Nachbeschleunigungspotential liegt, werden die Signale an dieser Stelle optisch umgewandelt und über Glasfaserleiter aus dem Hochspannungsbereich heraus zur Datenerfassung (DAQ) geleitet.

Während der für diese Arbeit relevanten Messdauer waren einige Auslesekanäle des Detektorquadranten zwei innerhalb des Kabelbaums nicht korrekt verkabelt, weshalb 13 Auslesekanäle ausfielen. Zudem zeigten 11 Kanäle einen hohen Rauschpegel bzw. ein Übersprechen untereinander. Während der Installation der neuen Ausleseelektronik im Sommer 2012 ist eine Vielzahl von Tests geplant, um eine korrekte Verkabelung sicherzustellen. Daher ist mit einer deutlich höheren Anzahl funktionsfähiger Kanäle während der nächsten Datennahme zu rechnen.

- **Datenerfassung und Slow Controls:**

Um die Signalpulse vom Detektor aufzunehmen, zu digitalisieren und zu analysieren, nutzt das FPD-System eine zweistufige DAQ-Elektronik. Sie besteht aus einer ersten Triggerstufe in Form von acht FLT-Karten. Jede dieser Karten ist in der

Lage, die analogen Daten von 24 Auslesekanälen aufzubereiten und mit Hilfe von 12-Bit-Analog-Digital-Wandlern mit einer Abtastrate von 20 MHz zu digitalisieren. In einer zweiten Trigger-Stufe (SLT-Karte) werden die ADC-Kurven in einem Buffer mit 64 Seiten gespeichert. Dies garantiert einen totzeit-freien Betrieb bei Raten bis 70 kHz. Um den unterschiedlich hohen Raten je nach Messart Rechnung zu tragen, kann zwischen verschiedenen Aufnahmemodi gewählt werden. Um die Energie und den Zeitpunkt eines Events auf dem Detektor aus den ADC-Kurven zu extrahieren, nutzt das DAQ-System zwei Trapezfilter. Die Datenerfassung kann von einem Computer mit Hilfe des objektorientierten Programmablaufs „ORCA“ gesteuert werden, das eine Kontrolle und Datenerfassung in Echtzeit ermöglicht. Die aufgenommenen Daten können hiermit zur weiteren Analyse in ROOT-Dateien gespeichert werden. Alle Geräte, die nicht direkt mit der Signalauslese des Detektors betraut sind, werden über das auf Labview basierende Programm „Slow Controls“ gesteuert. Es kommuniziert direkt mit einem kompakten Field-Point von National Instruments und erlaubt eine Fernbedienung von Druckluftmotoren, Pumpen, etc. .

- **Kalibrationsquellen**

Um den Detektor im autonomen Betrieb, d.h. ohne Verbindung zum Hauptspektrometer, zu kalibrieren und Testmessungen durchzuführen, sind mehrere Kalibrationsquellen im System installiert. Hervorzuheben sind hierbei eine ^{241}Am -Quelle, sowie eine Titanscheibe, die sich jeweils in das Strahlrohr einführen lassen ohne das Vakuum zu brechen. Mit Hilfe der ^{241}Am -Quelle lässt sich die Detektorantwort auf monoenergetische γ -Photonen untersuchen. Während der für diese Arbeit relevanten Messperiode stand jedoch nur eine niederaktive Quelle mit $< 3,7 \text{ MBq}$ zur Verfügung, was z.B. eine regelmäßige Kalibration des Detektors sehr zeitaufwändig gestaltete. Bis zur nächsten Messperiode mit dem Detektor ist daher eine Quelle mit höherer Aktivität (18,5 MBq) unabdingbar. Die Titanscheibe, welche auf Hochspannungen bis über 20 kV gesetzt werden kann, sendet bei Beleuchtung durch UV-Licht Photoelektronen aus. Damit kann die Detektorantwort auf monoenergetische Elektronen gemessen werden. Zur Beleuchtung der Scheibe wird eine UV-Leuchtdiode genutzt, die sich in einem optischen Aufbau befindet und von außen durch ein Quarz-Fenster in die Ultrahochvakuumkammer scheint. Am KIT konnte die Optik des Aufbaus wegen räumlicher Beschränkungen nicht korrekt justiert werden, was eine inhomogene Beleuchtung der Scheibe zur Folge hatte. Dies beeinflusst die Statistik für ca. zwei Drittel der Pixel in allen Messungen mit Photoelektronen. Der optische Aufbau wird derzeit überarbeitet. Bei der nächsten Datennahme ist daher eine bessere Illumination der Scheibe zu erwarten. Um die Linearität der Detektorelektronik zu vermessen, ist im optischen Aufbau zusätzlich eine rote LED verbaut. Die Zuordnung der verschiedenen Detektorkanäle kann mittels direkter elektronischer Pulse in die Vorverstärkermodule und die FLT-Karten des DAQ vollzogen werden.

- **Veto-System:**

Außer von einem passiven Schild aus niederaktivem Kupfer und Blei ist der Detektor des FPD-Systems von einem aktiven Vetsystem umgeben, das aus sechs St.-Gobain-Bicron-408 Plastik-Szintillatorplatten besteht. Diese dienen zur Messung des durch kosmische Myonen induzierten Untergrunds im Detektor. Die Lichtsignale aus den Szintillatorplatten werden über Glasfaserkabel zu 32 Multi-Pixel-Photon-Counters (MPPCs) geführt, welche im Geiger-Modus betrieben werden. Dadurch wandeln sie die Lichtpulse in elektrische Signale um und verstärken sie. Die MPPCs werden mit Hilfe von zwei wassergekühlten Peltier-Elementen bei Temperaturen unter $-16 \text{ }^{\circ}\text{C}$ betrieben, um hohe Dunkelzählraten zu vermeiden. Sie befinden sich in einer geschlossenen Stickstoffatmosphäre innerhalb der sogenannten „Veto-Box“. Während sich die MPPCs im oberen gekühlten Teil der Box befinden, ist die Verstärkerelektronik des

Vetos im unteren Teil montiert und mit den MPPCs über elektrische Durchführungen verbunden. Die Verbindungen wurden im Rahmen dieser Arbeit um eine zusätzliche Erdung für jeden MPPC ergänzt, um Oszillationen in den Auslesesignalen zu vermeiden und einen stabilen Betrieb der MPPCs zu gewährleisten. Zudem wurde das Wasserkühlssystem der Peltier-Elemente verbessert, da es hier zu Temperaturinstabilitäten gekommen ist. Damit ist die Grundlage geschaffen, um im Sommer 2012 erste Effizienz- und Koinzidenzmessungen mit dem Veto durchzuführen.

Während der Datennahme mit dem FPD-System im Frühjahr 2012 wurde das Betriebsverhalten des Detektors mit Hilfe der verschiedenen Kalibrationsquellen genau untersucht. Im Folgenden werden die ersten Ergebnisse dieser Messungen vorgestellt:

- **Linearität der Detektorelektronik:**

Um die Linearität der Ausleseelektronik des FPD-Systems zu untersuchen, wurde die Ultrahochvakuumkammer mit dem Licht einer roten LED geflutet. Trifft dieses Licht auf den Wafer generiert es dort Elektron-Loch Paare, deren Anzahl, und somit die Höhe des Signal Pulses, proportional zur Intensität des eingestrahlten Lichts ist. Es wurde eine maximale Abweichung von 5% zum linearen Verhalten gemessen, was für das System mehr als ausreichend ist.

- **Messungen mit der ^{241}Am -Quelle:**

Um eine Konvertierung von ADC-Kanälen zu Energien zu ermöglichen, wurde die Detektorantwort auf γ -Photonen der ^{241}Am -Quelle an den 59.54 keV γ -Peak im Americium-Energiespektrum angepasst. Aufgrund der geringen Aktivität der verfügbaren Quelle war eine regelmäßige Kalibration jedoch nicht möglich, was z.B. eine systematische Unsicherheit in der Totschicht-Bestimmung des Wafers zur Folge hat. Die Energieauflösung des Detektors für γ -Photonen wurde bei 59.54 keV zu $\Delta E = 1,637 \pm 0,004$ keV (FWHM) bestimmt. Dieser Wert entspricht dem gemittelten Ergebnis für 129 Pixel, die eine Antwort auf die Photonen lieferten.

- **Energieauflösung des Detektors für Elektronen:**

Bei Nutzung der Titanscheibe zur Bestimmung der Energieauflösung für mono-energetische Elektronen reduziert sich die Anzahl der verwendbaren Pixel aufgrund der oben beschriebenen Inhomogenität der Scheibenbeleuchtung auf 63. Hier konnte eine gemittelte Energieauflösung von $\Delta E = 1,8 \pm 0,2$ keV (FWHM) für 18,6 keV Elektronen bestimmt werden. Die erhöhte statistische Unsicherheit folgt aus Wechselwirkungen der Elektronen in der Totschicht des Wafers, die das Energiespektrum zu niedrigeren Energien hin verzerrten. Es ist zu erwarten, dass sich die Betriebstemperaturen des Wafers und der Ausleseelektronik nach der Installation der neuen Vorverstärkermodule und des neuen Kühlssystems im Sommer 2012 verringern. Dies wird zu geringeren Restströmen im Wafer und somit zu einer verbesserten Energieauflösung führen.

- **Untergrund durch Auger-Elektronen:**

Während der Messungen mit der Titanscheibe auf Hochspannung wurde ein bis dato unbekannter Untergrundeffekt entdeckt. Auch ohne Beleuchtung der Scheibe mit UV-Licht war eine Untergrundrate von über 300 Hz auf dem Detektor zu beobachten. Detaillierte Messungen zu diesem Effekt konnten eine Theorie bestätigen, die ihn mittels der Emission von Auger-Elektronen aus der Titanscheibe erklärt. Es ist zu erwarten, dass dieser Effekt nach einem Umbau der Scheibenaufhängung bei weiteren Messungen im Sommer 2012 nicht mehr auftritt.

- **Totschicht-Bestimmung:**

Um die Eigenschaften des Detektors und die durch ihn in das KATRIN-Experiment induzierten systematischen Unsicherheiten besser zu verstehen, ist die Kenntnis der

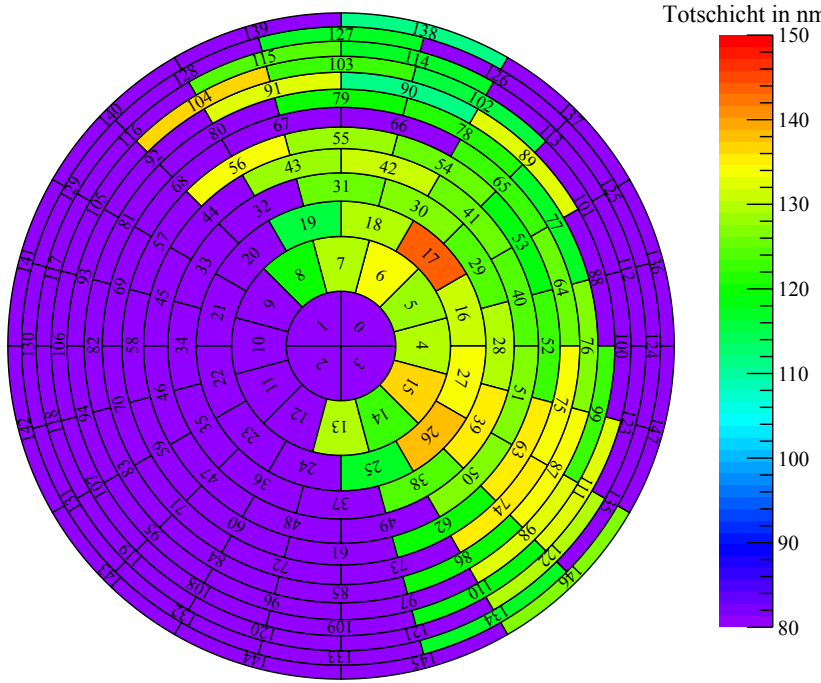


Abbildung 2.: **Die Verteilung der Totschicht pro Pixel** wurde mittels eines χ^2 -Vergleichs zwischen gemessenen Daten und Simulationen bestimmt. Ungefähr zwei Drittel der Pixel (lila) mussten aus verschiedenen Gründen von der Analyse ausgeschlossen werden. Aus darstellerischen Gründen wird auf eine Angabe von Unsicherheiten verzichtet. Die statistischen und systematischen Unsicherheiten der Totschicht-Ergebnisse können in Tabelle A.3 im Anhang eingesehen werden.

Detektor-Totschicht enorm wichtig. Diese wurde durch einen Vergleich zwischen der Detektorantwort auf monoenergetische Elektronen und Simulationen von Elektronen in Silizium bestimmt. Dabei wurde das Programm Paket KATRIN-Electrons-in-Silicon (KESS) benutzt. Dieses wurde innerhalb der Kooperation speziell zur Simulation von niedrigerenergetischen Elektronen im keV-Bereich in Silizium entwickelt. Der Vergleich wurde mittels eines χ^2 -Tests durchgeführt, wobei das simulierte Spektrum mit der experimentell bestimmten Energieauflösung des Detektors verschmiert wurde. In Abbildung 2 ist eine Übersicht der Totschichten für alle Detektorpixel zu sehen, bei denen eine Analyse möglich war. Es ist gut zu erkennen, dass ein Großteil der Pixel aufgrund der schlechten Beleuchtung durch die UV-LED, einer fehlenden Energiekalibration oder großen systematischen Unsicherheiten durch eine Schwankung in den Kalibrationsergebnissen ausgeschlossen werden mussten. Das gemittelte Ergebnis für die Totschicht des Detektors ist

$$\lambda_{\text{Global}} = \left(126,4 \pm 0,8 \text{ (stat.)} {}^{+0,2}_{-1,2} \text{ (syst.)} \right) \text{ nm.} \quad (3)$$

Es liegt damit leicht höher als der vom Hersteller angestrebte Wert von 100 nm.

Nach dem Aufbau und der Inbetriebnahme des FPD-Systems in der KATRIN-Hauptspektrometerhalle konnten die Betriebseigenschaften des Systems im Zuge dieser Arbeit genau untersucht und erste Messungen mit dem System durchgeführt werden. Weitere Messungen sind im Sommer 2012 nach dem Einbau diverser System-Upgrades geplant, bevor das FPD-System im Herbst 2012 mit dem Hauptspektrometer verbunden wird.

Contents

Erklärung	iii
Zusammenfassung	v
List of Figures	xv
List of Tables	xvii
1. Introduction	1
2. Neutrinos	3
2.1. Neutrinos in the Standard Model	3
2.2. Neutrino Oscillations	5
2.3. Determination of the Neutrino Mass	8
2.3.1. Model-Dependent Measurements	9
2.3.2. Model-Independent Measurements	11
3. The KATRIN Experiment	15
3.1. Main Components	15
3.1.1. Source	16
3.1.2. Transport Section	17
3.1.3. Spectrometers and the MAC-E Filter Principle	18
3.1.4. Focal-Plane Detector	20
3.2. Sensitivity	21
3.2.1. Systematic Uncertainties	21
3.2.2. Statistical Uncertainties	22
4. Physics of Semiconductor Diode Detectors	23
4.1. Semiconductors	23
4.1.1. The Band-Gap Model	23
4.1.2. The p-n Junction	26
4.2. Silicon PIN-Diode Detectors	27
4.2.1. The FPD Wafer	28
4.2.2. The Veto MPPCs	29
4.3. Simulation of Low-keV Electrons in Silicon	31
5. Assembly and Performance of the Focal-Plane Detector System at KIT	35
5.1. Background Requirements for the FPD System and the Figure of Demerit .	35
5.2. Main Components and their Performance	37
5.2.1. Magnets	37
5.2.2. Vacuum System	39
5.2.3. Post-Acceleration Electrode	40
5.2.4. Cooling System	40

5.2.5. Detector and Readout Electronics	42
5.2.6. Data Acquisition System and Slow Controls	45
5.2.7. Calibration Sources	47
5.2.8. Veto System	50
6. First Measurements and Results	53
6.1. Linearity	53
6.2. Energy Resolution	56
6.2.1. ^{241}Am -Source	56
6.2.2. Electron Disc	59
6.3. Auger Background	60
6.3.1. Theory of Background Production	62
6.3.2. Background Measurements and Results	63
6.4. Dead-Layer Determination	65
6.4.1. Simulation	65
6.4.2. Analysis	65
6.4.3. Dead Layer Results	70
7. Conclusion	73
Bibliography	77
Appendix	83
A. Measurement Tables	83
Danksagung	93

List of Figures

1.	Schematische Darstellung des FPD-Systems	vii
2.	Verteilung der Totschicht pro Pixel	xi
2.1.	Mass Hierarchy of the Neutrino Mass Eigenstates	8
2.2.	Energy Spectrum of the (Neutrinoless) Double β -Decay	10
2.3.	Influence of the Antineutrino Mass on the β -Decay Energyspectrum of Tritium	12
3.1.	Setup of the KATRIN Experiment	15
3.2.	Illustration of the MAC-E Filter Principle	18
3.3.	Schematic View of the FPD System	21
4.1.	Simplified Illustration of the Energy Band-Gap in a Semiconductor	24
4.2.	Mask of the FPD Pixel Pattern	28
4.3.	Schematic Draft of the FPD Wafer	29
4.4.	Dark Rate Spectrum of MPPC (#8)	30
4.5.	Comparison of a Geant4 Simulation with a KESS Simulation	32
4.6.	Comparison of KESS Simulation with Penelope08 & Experimental Data	32
5.1.	Picture of the FPD System Installed at KIT	36
5.2.	Drift of the Pinch-Magnet's Field with Time in Persistent Mode	38
5.3.	Draft of the FPD Vacuum System without the Pumpstation	39
5.4.	Picture of the New Post-Acceleration Electrode	41
5.5.	Picture of the Detector Wafer's Segmented Backside	43
5.6.	Schematic View of the Detector Feedthrough-Flange	44
5.7.	Picture of the Vacuum Electronics	45
5.8.	Response for the Two Trapezoidal Trigger Stages of the DAQ System	46
5.9.	Schematic View of the FPD's Calibration Sources	48
5.10.	Detector Rates with Electron Disc at 18.6 keV & Illuminated	49
5.11.	Picture of the Veto Readout Electronics	50
5.12.	Picture of the New Signal Feedthrough for the Veto	51
5.13.	Power Outputs of Peltier Cooler B	52
5.14.	Stability of the First Photoelectron Peak Positions with Time	52
6.1.	The Linearity of the FPD Electronics	54
6.2.	Distribution of the Linearity Slopes and Offsets for 125 Pixels	55
6.3.	^{241}Am Spectrum with a Gaussian Fit of the 59.54-keV Peak for 129 Pixels .	57
6.4.	Compton Scattering in the ^{241}Am Source Holder	58
6.5.	Global Spectrum of 18.6-keV Electrons	59
6.6.	Energy Dependence of Detector Response Resolution for Electrons	60
6.7.	Background Rates on the Detector with the Electron Disc at High Voltage .	61
6.8.	Energy Spectrum of the Electron Disc Background for Pixel 103	62
6.9.	Splitting of the First Background Peak of Pixel 103	64
6.10.	Simulated Detector Response for 15.12-keV Electrons	66

6.11. Flow-Chart of the Dead-Layer Analysis Procedure	67
6.12. Measured vs. Simulated Detector-Response Spectrum of Pixel 54	68
6.13. χ^2 Dependency on Dead Layer for Pixel 53 at an Energy of 15.12 keV	69
6.14. Energy Dependency of the Global Detector Dead Layer	70
6.15. Dead Layers of the Detector Pixels	71

List of Tables

2.1. Leptons in the Standard Model of Particle Physics	5
2.2. Experimental Results for the Neutrino Oscillation Parameters	7
4.1. Properties of Intrinsic Silicon and Germanium	25
4.2. Properties of the FPD Veto MPPCs	31
5.1. Heat Input by Low Voltage Power Supplies into the Vacuum System	42
6.1. Auger Transition Lines of Titanium	63
6.2. Fit Results for the Double-Peak Structure of the Auger Background	63
A.1. Voltage Settings of the Linearity Measurements	83
A.2. Energy Calibration Results with the ^{241}Am Source	84
A.3. Dead-Layer Results per Pixel	87
A.4. Measurements with the Electron Disc at Different Voltages	91
A.5. Overview of the Excluded Pixels in the Dead-Layer Analysis	92
A.6. Overview of the Detector-Response Simulation Settings in KESS	92

1. Introduction

For more than 80 years particle physicists have tried to determine the properties of neutrinos. Due to their exclusive weak interaction with matter, it requires high-precision measurements to study these properties and currently the masses of the three neutrino flavours are only known as limits. Since the exact knowledge of the neutrinos' absolute mass scale is of great importance for cosmology and particle physics, various ways to measure their masses are approached. In chapter 2 of this thesis an overview of the neutrinos' characteristics and the different approaches to measure their masses is given.

The KARlsruhe TRIumf Neutrino (KATRIN) experiment is a next generation model-independent neutrino mass measurement. Located at the Campus North of the Karlsruhe Institute of Technology (KIT) it precisely investigates the tritium β -decay spectrum close to its endpoint energy of 18.6 keV to derive the absolute mass of the electron anti-neutrino. KATRIN is expected to have an one order of magnitude higher sensitivity of $m_{\bar{\nu}} \leq 200 \text{ meV}/c^2$ (90% C.L.) compared to earlier experiments of this kind. The experiment with its different subsystems and its sensitivity is described in chapter 3.

Even with an unsurpassed rate of 10^{11} β -electrons per second from tritium decays in its high-intensity source, the signal rate in the Region of Interest (ROI) of KATRIN can be as low as 0.01 counts per second. Therefore, a total background rate of 10 mHz or smaller has to be achieved and a detector which provides a high detection efficiency is of great importance for the success of the experiment. The Focal-Plane Detector (FPD) system of the KATRIN experiment is based on a semiconductor PIN-diode wafer and fulfills these criteria. An overview of the physics of such detectors is given in chapter 4.

The FPD system was designed, built and tested in Seattle, Washington, USA by the KATRIN collaborators and subsequently shipped to KIT in summer 2011. The main objectives of this thesis are the assembly of the system in the KATRIN main spectrometer hall and the detailed investigation of its performance. A description of its different subsystems and the findings gained during the assembly process is given in chapter 5. This includes an outlook on numerous upgrades which are planned to be installed to the system in 2012. In addition, first measurements with the system, performed at KIT, are part of this thesis. A discussion on the results of these is given in chapter 6. In this context, some of the data is compared with Monte Carlo simulations of the detector response to low-keV electrons.

2. Neutrinos

The KATRIN experiment will probe the neutrino mass with an unsurpassed sensitivity of $m_{\bar{\nu}} \leq 200$ meV/c² (90% C.L.) via a precision measurement of the tritium β -decay spectrum close to its endpoint of 18.6 keV by kinematic means. In this chapter a short historical overview including the discovery of the different kinds of neutrinos their properties and their role in the SM, is given in section 2.1. In section 2.2 the phenomena of oscillation between the neutrino generations, which is not supported by the SM and can only be accommodated by a nonzero neutrino rest mass is discussed. A number of different approaches to measure the neutrino mass are presented in section 2.3.

2.1. Neutrinos in the Standard Model

Neutrinos they are very small.
They have no charge and have no mass
And do not interact at all.
The earth is just a silly ball
To them, through which they simply pass,
Like dustmaids down a drafty hall
Or photons through a sheet of glass.
They snub the most exquisite gas,
Ignore the most substantial wall,
Cold-shoulder steel and sounding brass,
Insult the stallion in his stall,
And, scorning barriers of class,
Infiltrate you and me! Like tall
And painless guillotines, they fall
Down through our heads into the grass.
At night, they enter at Nepal
And pierce the lover and his lass
From underneath the bed - you call
It wonderful; I call it crass.
John Updike, "Cosmic Gall"

This poem was written by John Updike [2] and quoted by the Nobel Prize committee when it awarded the 1995 Nobel Prize in physics to Frederick Reines for the first detection of the electron antineutrino. It describes, even if wrong about the zero neutrino mass,

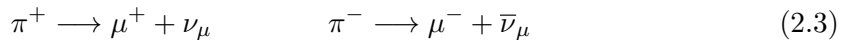
nicely the most important property of neutrinos - their weak interaction with matter. This weak interaction made the detection of (anti-)neutrinos and the investigation of their properties difficult from their postulation in 1930 until today, leaving Neutrino Physics a challenging field of science. After the discovery of the discrete energy spectra of the radioactive α - and γ -decays in the late 19th century Chadwick found the energy spectrum of the β -decay to be continuously in 1914 [3]. Since up to this point the β -decay was assumed to be a two-body decay, a continuous β -spectrum would violate the fundamental laws of energy conservation and angular-momentum conservation. It took 15 years until Pauli postulated a hypothetical uncharged spin-1/2 particle in 1930 and called it neutron. When created together with the electron in the β -decay it makes it a three-body decay and can therefore explain the shape of the β -spectrum [4]:



Pauli's work was continued by Enrico Fermi, who worked out the theoretical formulation of the β -decay in 1934 by the assumption of a point-like interaction. It was Fermi, who gave the neutrino its present name after the discovery of the neutron by Chadwick in 1932 as a part of the atomic nucleus [5]. The cross sections for the interaction of the neutrino with matter, calculated with Fermi's theory, are valid until today in the limit of low energies and are found to be small [6]. This weak interaction made an experimental discovery of the neutrino difficult and it took another 12 years until Reines and Cowan found evidence of the electron antineutrino at the Savannah River Plant nuclear reactor in their 'Poltergeist' experiment in 1956 [7]. They used two tanks, each filled with 200 liters of cadmium chloride solution ($CdCl_2$), surrounded by three 1,400 liter liquid scintillation counters to detect the electron antineutrinos coming from the nuclear reactor. The neutrinos interact with the protons of the water in the tanks by an inverse β^+ -decay:



The positrons produced in the decay react electromagnetically within the water and liquid scintillator loosing most of their kinetic energy until they annihilate with shell electrons emitting two opposed monoenergetic photons with an energy of 511 keV each. The neutron created according to formula (2.2) slows down within a few microseconds by collisions with water molecules and is captured by a cadmium nucleus, leaving it in an excited state. When the cadmium nucleus falls back to its ground state, it emits a few photons with an energy of 3 to 11 MeV. Therefore, it was possible to detect the electron antineutrino by a delayed coincidence measurement of the positron and neutron signatures provided by the scintillation counters around the tanks. With a neutrino flux of $\sim 10^{13} s^{-1} cm^2$ coming from the nuclear reactor, they were able to measure 3 events per hour with the detector and found the cross section for the reaction in equation (2.2) to be $\sigma = 1.2^{+0.7}_{-0.4} \cdot 10^{-43} cm^2$ in good agreement with Fermi's theory [7]. A second type of neutrino (ν_μ) was discovered in 1962 by Schwartz, Ledermann and Steinberger at the Brookhaven National Laboratory, when they examined the pion decay from a pion beam created by a particle accelerator:



It was found that the neutrinos created according to formula (2.3) never induced the creation of electrons or positrons but only the creation of μ^\pm , demonstrating that the muon neutrino and the electron neutrino are not identical particles [8]. The third generation of neutrinos (ν_τ), predicted by the SM of particle physics, was discovered in 2001 at the DONUT experiment at the Fermilab [9]. A combination of the Z^0 -bosons decay-width data at the LEP particle accelerator in 2004, determined the number of light neutrino generations to be $N = 3.00 \pm 0.08$ [10]. The most recent result stated by [11] is $N = 2.92 \pm 0.05$.

Table 2.1.: **Leptons in the Standard Model of Particle Physics** with their charge in units of the electron charge $q = e$, their Lepton number and the interactions they participate in.

Generation						
1	2	3	Charge	Lepton Number	Interaction	
e^-	μ^-	τ^-	-1	+1	weak, electromagnetic	
ν_e	ν_μ	ν_τ	0	+1	weak	
e^+	μ^+	τ^+	+1	-1	weak, electromagnetic	
$\bar{\nu}_e$	$\bar{\nu}_\mu$	$\bar{\nu}_\tau$	0	-1	weak	

In the SM the three generations of neutrinos interact only by the neutral (NC-reaction) and the charged (CC-reaction) currents of the weak interaction via the exchange of the gauge bosons W^\pm and Z^0 not with the currents of the electromagnetic or the strong interaction. Therefore, their so-called weak eigenstates (ν_e , ν_μ and ν_τ) build the electrically neutral part of the Lepton group in the SM (as it is shown in table 2.1). Further, the SM predicts a negative helicity for neutrinos and a positive helicity for the antineutrinos which results from the maximal violation of parity in the weak interaction and the zero rest mass of the neutrinos, which the SM assumes. In 1958, Goldhaber experimentally measured the helicity of the neutrinos to be $h_\nu = -1.0 \pm 0.3$ [12]. Thus, in the SM only left-handed neutrinos and right-handed antineutrinos couple to the gauge bosons of the weak interaction. In addition, the SM predicts the lepton number L as well as the lepton-flavour number L_α to be conserved in any process. Today it is known that physics beyond the SM exist and the effect of neutrino oscillations leads to restrictions on for example the conservation of the lepton-flavour number.

2.2. Neutrino Oscillations

In 1998, the Super-Kamiokande detector in Japan found evidence for oscillations between the different generations of neutrinos. The detector is located 1,000 m underground and consists of a water tank filled with 50,000 tons of water, which is surrounded by 11,146 photomultipliers. In the earths atmosphere high-energy cosmic rays react with protons and create pions, which subsequently decay:

$$\pi \longrightarrow \mu \nu_\mu \quad (\mu \longrightarrow e \nu_e \nu_\mu) \quad (2.4)$$

The neutrinos created in the decay according to formula (2.4) are detected with the Super-Kamiokande detector by weak interactions in the water where charged leptons of the same generation are created. While travelling through the water, these leptons create Cherenkov light-cones emitted in the direction of flight, which can be detected by the photomultipliers. Due to the higher rate of scattering of electrons, their light-cones are broader than the ones from muons and it is possible to differentiate between the electron and the muon neutrino signals. With this detection principle the Super-Kamiokande-experiment was able to detect a flight-distance dependent disappearance of atmospheric muon neutrinos, while the rate of electron neutrinos was flight-distance independent. The muon neutrinos therefore must have oscillated into tau neutrinos on their way to the detector [13]. Other experiments have looked for neutrino oscillations as well including the Sudbury Neutrino Observatory (SNO) experiment, which addressed the so-called 'solar neutrino deficit'. Built $\sim 2,000$ m underground in a mine close to Sudbury, Ontario, Canada, its detector consists of a transparent acrylic sphere of 12 m diameter filled with 1,000 tons of heavy water (D_2O) and

surrounded by 9,456 photomultipliers. The difference of SNO to other neutrino-oscillation experiments is the heavy water, which it uses as a target and which allows not only a measurement of a distinct neutrino flavour (ν_e) through CC-reactions with the heavy water but a measurement of all flavours of neutrinos coming from the sun through NC-reactions, too. This enabled a solar-model independent measurement of the solar neutrino flux from the 8B -decay in the sun:

$$\Phi_B = \left(5.25 \pm 0.16 \text{ (stat.)} {}^{+0.11}_{-0.13} \text{ (syst.)} \right) \cdot 10^6 \text{ cm}^{-2}\text{s}^{-1} \quad (2.5)$$

In addition, it found the electron neutrino survival probability during daytime and at an energy of 10 MeV to be:

$$c_0 = 0.317 \pm 0.016 \text{ (stat.)} \pm 0.009 \text{ (syst.)} \quad (2.6)$$

The solar neutrino deficit, which was first observed by Davis in the Homestake experiment in 1968 by a radiochemical chloride-argon method is a deficit in the measured rate of electron neutrinos coming from the sun compared with the theoretical predictions of the solar models [14]. The SNO results can explain this deficit by the oscillation of electron neutrinos ν_e into the two other neutrino flavours, while the total flux of solar neutrinos ν_α is constant [15].

The mechanism of neutrino oscillations has consequences for the SM of particle physics, since the lepton flavour number is not conserved anymore. In addition, oscillating neutrinos cannot be massless as it is discussed in the following. The first theoretical ideas about neutrino oscillations came up in 1957 by Pontecorvo and describe a periodically changing probability in time to find a distinct neutrino flavour α [16]. The theory of neutrino oscillations claims the eigenstates of the weak interaction (ν_e , ν_μ and ν_τ) not to be identical with the mass eigenstates (ν_1 , ν_2 and ν_3) of the neutrinos but a superposition of them:

$$|\nu_\alpha\rangle = \sum_{i=1}^3 U_{\alpha i} |\nu_i\rangle \quad (\alpha = e, \mu, \tau) \quad (2.7)$$

With the unitary PMNS (Pontecorvo-Maki-Nakagawa-Sakata) - matrix U that depends on three mixing angles θ_{12} , θ_{13} and θ_{23} as well as on a CP-violating phase δ and Majorana phases α_1 , α_2 :

$$U = \begin{pmatrix} 1 & 0 & 0 \\ 0 & \cos(\theta_{23}) & \sin(\theta_{23}) \\ 0 & -\sin(\theta_{23}) & \cos(\theta_{23}) \end{pmatrix} \cdot \begin{pmatrix} \cos(\theta_{13}) & 0 & \sin(\theta_{13})e^{-i\delta} \\ 0 & 1 & 0 \\ -\sin(\theta_{13})e^{i\delta} & 0 & \cos(\theta_{13}) \end{pmatrix} \times \\ \times \begin{pmatrix} \cos(\theta_{12}) & \sin(\theta_{12}) & 0 \\ -\sin(\theta_{12}) & \cos(\theta_{12}) & 0 \\ 0 & 0 & 1 \end{pmatrix} \cdot \begin{pmatrix} e^{i\alpha_1/2} & 0 & 0 \\ 0 & e^{i\alpha_2/2} & 0 \\ 0 & 0 & 1 \end{pmatrix} \quad (2.8)$$

After its creation in a weak interaction a ν_α -beam with distinct momentum propagates with time. Since the energy of the superposed ν_i mass eigenstates in the beam depends on their rest mass, an evolution in time of the ν_α -beam gives:

$$|\nu_\alpha(L)\rangle = \sum_{k=1}^3 U_{\alpha k} \cdot e^{-i \frac{m_k^2 \cdot L}{2E}} |\nu_k\rangle \quad (2.9)$$

Where L is the distance from the point of creation to the point of detection (in km) and E is the energy of the beam (in GeV). The probability for a neutrino oscillation from flavour

Table 2.2.: **Experimental Results for the Neutrino Oscillation Parameters** from different experiments. Most of the results are taken from [11]. The value for $\sin^2(2\theta_{13})$ was published by the Daya Bay experiment in April 2012 with a significance of 5.2σ [17]. It is consistent with the results of other experiments such as RENO [18], which indicate a nonzero mixing angle θ_{13} as well.

Experiment	Neutrino Source	Result
KamLAND + other experiments	reactor neutrinos	$\sin^2(2\theta_{12}) = 0.861^{+0.026}_{-0.022}$
	solar neutrinos	$\Delta m_{21}^2 = (7.59^{+0.20}_{-0.21}) \cdot 10^{-5} \text{ eV}^2/\text{c}^4$
Super-Kamiokande-I	atmospheric neutrinos	$\sin^2(2\theta_{23}) > 0.92$
MINOS	atmospheric neutrinos	$\Delta m_{32}^2 = (2.43 \pm 0.13) \cdot 10^{-3} \text{ eV}^2/\text{c}^4$
Daya Bay	reactor neutrinos	$\sin^2(2\theta_{13}) = (9.2 \pm 1.6 \pm 0.5) \cdot 10^{-2}$

α to flavour β is given by:

$$\begin{aligned} P(|\nu_\alpha\rangle \rightarrow |\nu_\beta\rangle) = & \delta_{\alpha\beta} - 4 \cdot \sum_{i>j} \operatorname{Re} (U_{\alpha i}^* U_{\beta i} U_{\alpha j} U_{\beta j}^*) \cdot \sin^2 (1.27 \cdot \Delta m_{ij}^2 L/E) \\ & + 2 \cdot \sum_{i>j} \operatorname{Im} (U_{\alpha i}^* U_{\beta i} U_{\alpha j} U_{\beta j}^*) \cdot \sin^2 (2.54 \cdot \Delta m_{ij}^2 L/E) \end{aligned} \quad (2.10)$$

For a system with two flavour states ($\alpha = e, \mu$ and $i = 1, 2$) only the formula in (2.10) simplifies to:

$$P(|\nu_\alpha\rangle \rightarrow |\nu_\beta\rangle) = \sin^2(2\theta_{12}) \sin^2 \left(1.27 \cdot \frac{\Delta m_{21}^2 L}{E} \right) \quad (\alpha \neq \beta) \quad (2.11)$$

Therefore, the probability of a neutrino oscillation between two flavours depends on the distance L between the source and the detector as well as the energy E of the neutrino beam. Experiments use a source of neutrinos known in its properties and determine the oscillation parameters such as the mixing angle θ_{ij} and the square of the mass differences Δm_{ij}^2 of the mass eigenstates with a given distance from the source to the detector and a known energy of the neutrino beam. While the mixing angle defines the amplitude of the oscillation, the square of the mass differences between the flavours defines its frequency. It should be noted that the probability in equation (2.11) turns out to be zero for a zero rest mass of all neutrino flavours. According to the measured neutrino oscillations, at least two of the flavours must have a non-zero rest mass with a dependency between the squares of the mass differences given by:

$$\Delta m_{31}^2 = \Delta m_{21}^2 + \Delta m_{32}^2 \quad (2.12)$$

Nevertheless, the oscillation experiments cannot determine the absolute rest mass of the neutrinos but only the square of their mass differences. While the phases δ , α_1 , α_2 and the square of the mass difference Δm_{31}^2 are not known yet all other mixing parameters were measured in different experiments and can be found in table 2.2. From equation (2.12) and the results in table 2.2, three possible mass hierarchies for the three neutrino mass eigenstates are possible. If the masses of all mass eigenstates were in the same order of magnitude ($m_1 \approx m_2 \approx m_3$), a quasi-degenerated mass distribution would be possible with the squared mass differences found by the neutrino oscillation experiments being much smaller as the absolute masses ($\Delta m^2 \ll m_i^2$). This would result in quite large absolute masses of $m_i > 0.2 \text{ eV}/\text{c}^2$. In the case of small absolute masses ($\Delta m^2 \approx m_i^2$) a

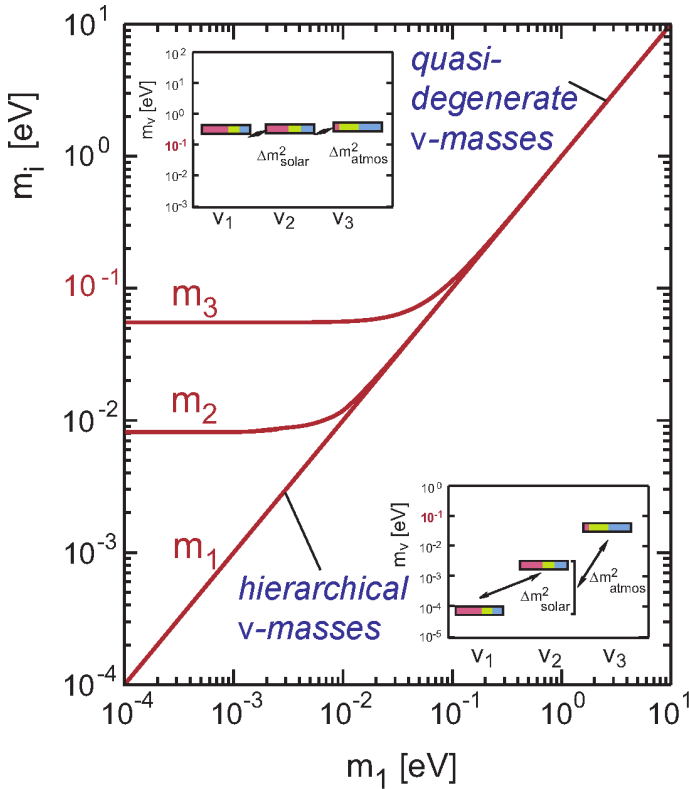


Figure 2.1.: **Mass Hierarchy of the Neutrino Mass Eigenstates** as a function of the lightest eigenstate m_1 . With m_1 approaching zero the mass distribution turns into a normal hierarchical structure ($m_1 \ll m_2 < m_3$) whereas for a high mass of ν_1 all eigenstates have approximately the same mass $m_1 \approx m_1 \approx m_3$ (quasi-degenerated hierarchy). Note, that the square of the mass difference Δm_{31}^2 is not measured yet and therefore an inverted mass hierarchy with $m_3 \ll m_2 < m_1$ is possible as well (From [19]).

hierarchical mass distribution is possible were the m_i would differ by orders of magnitude and one of them could even be zero. Since the square of the mass difference Δm_{31}^2 has not been measured yet by oscillation experiments two scenarios are possible. A normal hierarchical mass distribution with $\Delta m_{31}^2 > 0$ and a mass distribution with inverted hierarchy $\Delta m_{31}^2 < 0$. In figure 2.1 the different mass hierarchies are shown as a function of the lightest mass eigenstate m_1 . With its sensitivity of $m_{\bar{\nu}_e} = 200$ meV/c² (90% C.L.) the KATRIN experiment is able to prove either the quasi-degenerated or the hierarchical mass distribution for the neutrino mass eigenstates. Further, with the knowledge of one neutrino flavour's mass it is possible to reconstruct the mass of the two other neutrinos using the PMNS matrix.

2.3. Determination of the Neutrino Mass

In principle, the different experiments to determine the absolute mass of the neutrinos can be divided into two groups. While **model-dependent** measurements can be very sensitive to the neutrino mass their results depend on various theoretical models. **Model-independent** measurements only assume the conservation of energy and momentum to determine the neutrino mass and do not rely on any further assumptions, i.e. the theoretical models of neutrinos. To do so they use the relativistic energy momentum relation [19].

2.3.1. Model-Dependent Measurements

- **Determination of the Neutrino Masses from Cosmology**

The Wilkinson Microwave Anisotropy Probe (WMAP) satellite experiment launched in 2001, measures the variations in the temperature of the cosmic microwave background radiation with a μk precision. Its results represent the structure of the universe about 380,000 years after the Big Bang and, by an expansion into spherical harmonics, information concerning the fluctuations of the matter density in the early universe can be extracted. It is able to significantly constrain cosmological parameters such as the total mass density Ω_{tot} , the baryonic matter density Ω_b , the matter density Ω_m , the dark energy density Ω_Λ and the neutrino density Ω_ν . In cosmology there is no differentiation made between the flavours of neutrinos and all flavours contribute to the cosmological neutrino background in the same way. To determine an upper limit on the mass of all neutrino flavours together, the common ΛCDM -model of the universe is used. Until today, it is able to describe all measured properties of the universe at some level and it provides a relationship between the proportion Ω_ν contributed by neutrinos to the total energy density Ω_{tot} of the universe and the sum of the neutrino masses [20]:

$$\sum_\nu m_\nu = 94 \cdot \Omega_\nu h^2 \text{ eV/c}^2 \quad (2.13)$$

Here $h = 0.704 \pm 0.025$ is the Hubble constant [11]. Therefore, the sum of the neutrino masses can be determined by a measurement of Ω_ν . The WMAP data of five years measurement time gives $\Omega_\nu h^2 < 0.0062$ (95% C.L.). This results in an upper limit for the sum of the neutrino masses of [20]:

$$\sum_\nu m_\nu \leq 1.3 \text{ eV/c}^2 \quad (95\% \text{ C.L.}) \quad (2.14)$$

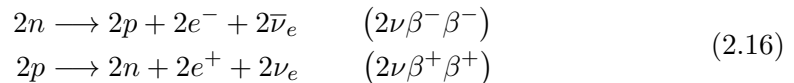
If the WMAP data is combined with recent results from SDSS [21] and HST [22], the upper limit is lowered to [11]:

$$\sum_\nu m_\nu \leq 0.44 \text{ eV/c}^2 \quad (95\% \text{ C.L.}) \quad (2.15)$$

Nevertheless, all results are strongly model-dependent, i.e. of the model of the universe ΛCDM .

- **Determination of the Neutrino Mass from Neutrinoless Double β -Decay**

In Nuclear Physics the binding energies inside a nucleus can be described by the semi-empirical Bethe-Weizsäcker equation. With a fixed nucleon number A the equation simplifies to a parabola. In the case of an even number of nuclei in the atomic nucleus this so-called mass parabola splits up into two, one for cores with an even-even configuration of neutrons and protons (ee-cores) and one with an odd-odd configuration (oo-cores). If the ground state of an ee-core has a lower binding energy than the neighbouring oo-core, a single β -decay can be forbidden. In this case a double β -decay is possible, which is a process of second order and has therefore a low probability and a long half life of $\sim 10^{20}$ years. In an usual double β -decay two nucleons are converted in the mother atom simultaneously with an emission of two electrons (positrons) and two electron antineutrinos (neutrinos):



The full kinematic energy of the charged leptons in this decay (with a decay energy of Q) is continuously distributed between $E_{\min} = 0$ and $E_{\max} = Q - 2m_e c^2 - 2m_\nu c^2$.

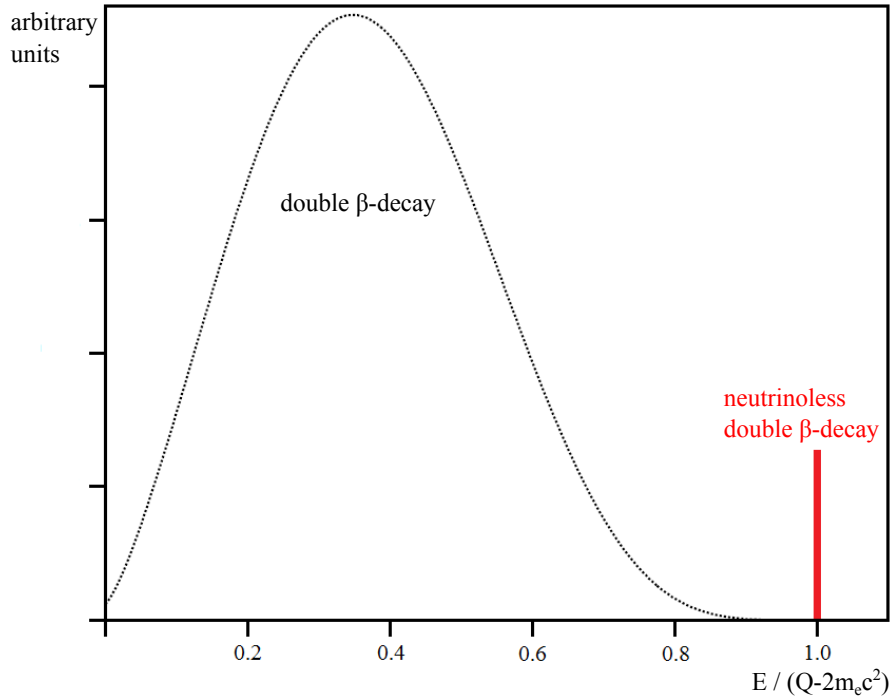
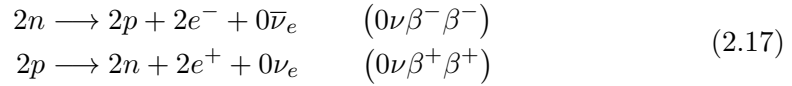


Figure 2.2.: The Energy Spectrum of the (Neutrinoless) Double β -Decay shows the dependency of the count rate (in arbitrary units) to the total energy of the charged leptons. In the normal double β -decay ($2\nu\beta\beta$) the energy is distributed continuously to the endpoint whereas for the neutrinoless double β -decay ($0\nu\beta\beta$) a monoenergetic line at the total decay energy is generated, when the decay involves only electrons (From [23], mod.).

The lepton number is conserved and this process is allowed in the SM. In 1967, it was discovered for the first time by Kirsten and Müller in the decay of ^{82}Se to ^{82}Kr with a half life of $1.4 \cdot 10^{20}$ years (error of 20%) [24].

In the search for physics beyond the SM a neutrinoless double β -decay ($0\nu\beta\beta$) is conceivable but was not yet verified:



In this case the neutrinos emitted during the conversion of the two nuclei are virtual and annihilate within the atoms core. To do so the neutrinos must be their own antiparticle and need to have a non-zero rest mass to perform a helicity flip. Thus, the neutrinos must be, in disagreement with the SM, Majorana fermions. In addition, this process would imply the Lepton number to not be conserved ($\Delta L = 2$). Even with a low rest mass the probability of a helicity flip of one of the neutrinos is small, which leads to a suppression of the neutrinoless double β -decay against the normal double β -decay. If the neutrinoless decay was possible, it would be seen in the spectrum as a monoenergetic line at $E = Q - 2m_e c^2$ as it is shown in 2.2 and from its measured half life $\tau_{1/2}^{0\nu}$, a phase space factor $G^{0\nu}$, a model-dependent nuclear matrix element $M^{0\nu}$ and the unknown phases δ , α_1 and α_2 (see equation (2.8)) the

effective Majorana-neutrino mass $m_{\beta\beta}$ can be determined:

$$m_{\beta\beta}^2 = \left| \sum_i U_{ei}^2 m_i \right|^2 = \frac{1}{G^{0\nu} \cdot |M^{0\nu}|^2 \cdot \tau_{1/2}^{0\nu}} \quad (2.18)$$

The first experimental value for the Majorana-neutrino mass was provided by the Heidelberg-Moskau experiment which examined the double β -decay of ^{76}Ge to ^{76}Se and found [11]:

$$m_{\beta\beta} = (0.32 \pm 0.03) \text{ eV/c}^2 \quad (68\% \text{ C.L.}) \quad (2.19)$$

Due to a special kind of analysis and the low significance of the measurement, this result is not commonly accepted. Other experiments like GERDA [25] or MAJORANA [26] will examine this result and improve the significance.

- **Time-of-Flight Studies of Supernovae Neutrinos**

With the supernovae SN1987A observed on the 23rd February 1987, an opportunity occurred to determine the electron neutrino's mass by a time-of-flight study of the neutrinos created during the supernovae. It was a type-II supernovae which are extremely bright sources of neutrinos and usually involve massive stars of several solar masses. At the end of the fusion process the star can no longer withstand the high gravitational forces and collapses under its own weight, forming a neutron star or a black hole. In this process neutrinos are generated according to:



The emitted neutrinos carry away 99% of the gravitational energy and the duration of the emission lasts ~ 10 seconds. Since the shape of the neutrino pulse depends strongly on the theory of the mechanism of the stellar collapse, the neutrino masses derived from the supernovae are model-dependent. From SN1987A 25 neutrino events were measured by the underground detectors Kamiokande II [27], IMB [28] and the Baksan Neutrino Observatory [29]. Two neutrinos created in the supernovae with different energies $E_{\nu,1} > E_{\nu,2}$ arrived at the detectors in a time span:

$$\Delta t = t_2 - t_1 = \Delta t_0 + L m_\nu^2 c^3 \left(\frac{1}{E_{\nu,2}^2} - \frac{1}{E_{\nu,1}^2} \right) \quad (2.21)$$

With the distance L from the supernovae to the detector ($L = 1.5 \cdot 10^{18}$ km) and an unknown parameter Δt_0 with regards to the duration of emission in the supernovae. Since an assumption on this parameter is needed to calculate the neutrino mass, the results are model-dependent. In 2002, a detailed analysis by Loredo and Lamb found an upper limit of the electron antineutrino mass of [30]:

$$m_{\nu_e} \leq 5.7 \text{ eV/c}^2 \quad (95\% \text{ C.L.}) \quad (2.22)$$

2.3.2. Model-Independent Measurements

Model-independent measurements of the neutrino mass use the relativistic energy momentum relation $E^2 = p^2 c^2 + m_0^2 c^4$ to determine the mass of a neutrino flavour. A limit on the mass of the muon neutrino was determined by Assamagan and others with a detailed investigation on the decay of an idle pion ($\pi^+ \rightarrow \mu^+ + \nu_\mu$) in 1996. With the well-known masses of the pion m_π , the muon m_μ and the measurement of the modulus of the muon momentum in this decay $|\vec{p}_{\mu^+}|$ an upper limit to the mass of the muon neutrino was derived [31]:

$$m_{\nu_\mu} \leq 0.17 \text{ MeV/c}^2 \quad (90\% \text{ C.L.}) \quad (2.23)$$

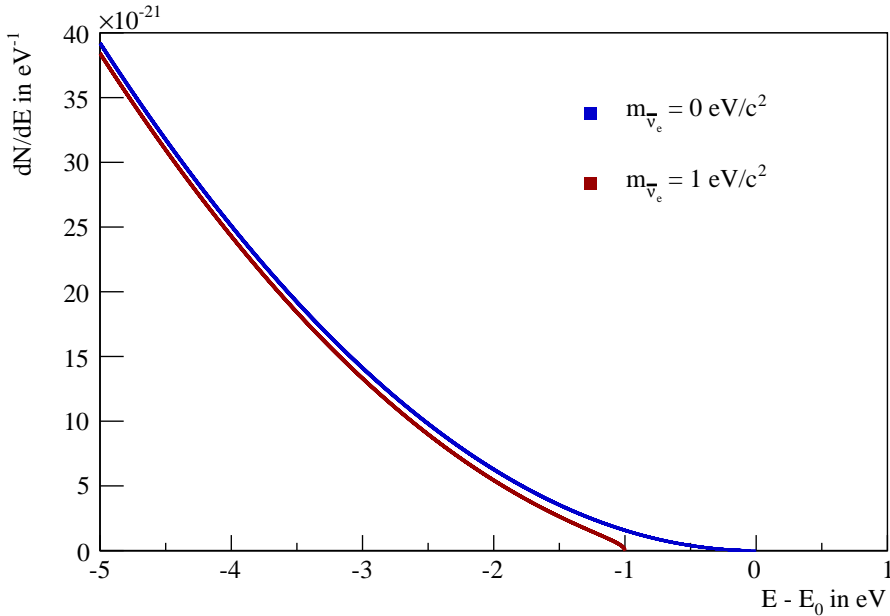
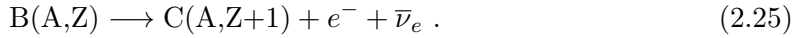


Figure 2.3.: Influence of the Antineutrino Mass on the β -Decay Energyspectrum of Tritium. A zoom into the region of the endpoint is shown, where the antineutrino mass significantly determines the shape of the spectrum. The blue line represents a spectrum with an antineutrino mass of $m_{\bar{\nu}_e} = 0 \text{ eV}/c^2$ and the red line a mass of $m_{\bar{\nu}_e} = 1 \text{ eV}/c^2$.

To derive a limit on the tau neutrino's mass a τ^- -decay in-flight was examined at the ALEPH experiment by a measurement of the summed energy of the created charged pions. The missing decay energy was assumed to be the rest energy of the tau neutrino. The upper limit on the tau neutrino's mass was determined to [32]:

$$m_{\nu_\tau} \leq 18.2 \text{ MeV}/c^2 \quad (95\% \text{ C.L.}) \quad (2.24)$$

To derive the mass of the electron neutrino model-independent a precise examination of the continuous β -spectrum of the electrons from a β -decay close to its endpoint is used (see figure 2.3):



A neutron in the mother nucleus is converted to a proton in a CC-reaction, creating the daughter nucleus. The decay energy Q is, neglecting the recoil energy of the daughter nucleus, transferred to the created leptons. Therefore, the kinetic energy of the β -electrons becomes continuously distributed to an energy $E_{\max} = E_0 - m_{\bar{\nu}_e} c^2$ with the endpoint energy $E_0 = Q - m_e c^2$. By the application of Fermi's Golden Rule, the differential β -spectrum of the electron can be derived to:

$$\frac{dN}{dE} = \frac{G_F^2 \cdot \cos^2(\theta_C) \cdot |M|^2}{2\pi^3 c^5 \hbar^7} \cdot F(Z+1, E) \cdot p \cdot (E + m_e c^2) \cdot (E_0 - E) \times \sqrt{(E_0 - E)^2 - m_{\bar{\nu}_e}^2 c^4} \cdot \Theta(E_0 - E - m_{\bar{\nu}_e} c^2) \quad (2.26)$$

With the electron's momentum p , the Cabibbo angle θ_C and the Fermi Function $F(Z+1, E)$, which takes the Coulomb interaction between the emitted electron and the daughter nucleus into account. The Heavyside Function Θ ensures the conservation of energy and the matrix element M can be derived from the theory of the weak interaction. Referring

to equation (2.7), the mass of the electron antineutrino can be written as an incoherent weighted sum of the squared mass eigenstates:

$$m_{\bar{\nu}_e}^2 = \sum_{i=1}^3 |U_{ei}|^2 m_i^2 \quad (2.27)$$

Since, according to table 2.2, the differences between the masses m_i are small, it is not possible to resolve them and the observed parameter in the kinematic experiments is the squared mass of the antineutrinos flavour eigenstate $m_{\bar{\nu}_e}^2$, which influences the shape of the β -spectrum of the electrons close to the endpoint E_0 . The event rate of the β -electrons close to the endpoint depends on a factor $1/E_0^3$, which constrains the experiments to use β -sources with low endpoints.

- **Rhenium as a β -Source**

The lowest endpoint energy of all β -radiators provides ^{187}Re with $E_0 = 2.47$ keV. In $6 \cdot 10^{-11}$ of all events the β -electrons have energies within 1 eV below the endpoint but the half life of ^{187}Re is quite large ($\tau_{1/2} = 4.32 \cdot 10^{10}$ years), requiring a high amount of rhenium to get a reasonable activity [19]. In difference to tritium the β -decay of rhenium is not a super-allowed transition, which is the reason for the quite high half life and an energy dependence of the matrix element M in equation (2.26). Most of the experiments using rhenium work with cryogenic bolometers, which are β -source and detector at the same time. The current upper limit for the neutrino mass from a ^{187}Re experiment is measured by the Milano experiment, which uses an AgReO_4 micro-calorimeter array [33]:

$$m_{\bar{\nu}_e} \leq 21.7 \text{ eV/c}^2 \quad (90\% \text{ C.L.}) \quad (2.28)$$

In the near future the MARE-I experiment wants to improve this upper limit with its sensitivity of $m_{\bar{\nu}_e} \leq 2 \text{ eV/c}^2$ [34]. In addition, a second phase of the MARE experiment is planned with an improved sensitivity of $m_{\bar{\nu}_e} \leq 200 \text{ meV/c}^2$ [35].

- **Tritium as a β -Source**

Currently, the most accurate model-independent measurement of the electron anti-neutrino's mass is done by the investigation of the tritium (^3H) β -decay. With the second lowest endpoint energy of all known β -decaying elements of $E_0 = 18.6$ keV, the tritium decay generates a rate of $2 \cdot 10^{-13}$ electrons with an energy closer than 1 eV to the endpoint. In addition, its half life ($\tau_{1/2} = 12.32$ years) is much lower than for Rhenium and therefore, a much lower amount of tritium is needed for a reasonable source activity. Another advantage of tritium with its daughter nucleus $^3\text{He}^+$ is the simple electron configuration of both, which is likewise the configuration of hydrogen and the low proton number ($Z=1,2$). Thus, the coulomb interaction of the emitted β -electron with the daughter nucleus considered by the Fermi Function $F(Z=2, E)$ in equation (2.26) is easy to determine. Furthermore, the inelastic scattering of the electrons within the source with tritium gas is relatively small, due to the weak coulomb interaction ($Z=1$). The tritium β -decay is a super-allowed decay and therefore, the shell configuration of tritium and its daughter nucleus $^3\text{He}^+$ are the same, which results in an energy-independent matrix element $|M|^2 = 5.55$ in equation (2.26).

The current way of measuring the neutrino mass by the investigation of a tritium β -decay is the magnetic adiabatic guidance of the β -electrons to an electrostatic retardation spectrometer with a magnetic adiabatic collimation (MAC-E filter) [36]. At the output of the spectrometer a detector with a high detection efficiency determines the rate of electrons, which were able to pass the retarding potential. This

results in an integral spectrum of the tritium β -decay electrons from which a differential spectrum like in equation (2.26) can be derived. Even if the use of tritium as a source for the β -decay has a lot of advantages some corrections have to be applied to the differential spectrum. Radiative corrections of higher orders for the tritium decay have to be taken into account as well as excited states and the tritium purity. In addition, the electrons that travel from the source to the detector on a cyclotron trajectory emit synchrotron radiation and the retarding potential of the spectrometer together with the high magnetic-guiding fields can create Penning traps. Usually it is not possible to use atomic tritium but molecular tritium (see equation (2.29)) and the distribution of the final states has to be considered [19]:



The experiments in Troitsk and Mainz, both using tritium as a source, have determined the best model-independent upper limits for the neutrino mass until today. The Troitsk experiment used a windowless gaseous tritium source and a spectrometer of 1.2 m in diameter to derive an upper limit for the electron antineutrinos mass of [37]:

$$m_{\bar{\nu}_e} \leq 2.05 \text{ eV/c}^2 \quad (95\% \text{ C.L.}) \quad (2.30)$$

In Mainz, a quench-condensed tritium source was used with a spectrometer of 1 m in diameter. The upper limit derived from the Mainz experiment is [38]:

$$m_{\bar{\nu}_e} \leq 2.3 \text{ eV/c}^2 \quad (95\% \text{ C.L.}) \quad (2.31)$$

In [11] a combined result of both experiments is given by:

$$m_{\bar{\nu}_e} \leq 2.0 \text{ eV/c}^2 \quad (95\% \text{ C.L.}) \quad (2.32)$$

This is today's model-independent upper limit on the electron antineutrino's mass.

3. The KATRIN Experiment

The KATRIN experiment represents the next generation of a model-independent neutrino mass measurement using tritium as a source. Compared with the recent experiments in Troitsk and Mainz it will have an one order of magnitude higher sensitivity for the measurement of the electron antineutrino's mass of $m_{\bar{\nu}} \leq 200$ meV/c² (90% C.L.). With a total length of ~ 70 m and a main spectrometer with a diameter of 10 m the experimental setup is nearly ten times larger than the earlier experiments. It is located at the Campus North of KIT right beside the Tritium Laboratory Karlsruhe (TLK). The TLK has more than 15 years of experience in technologies for tritium processing and can provide both the infrastructure and license required to handle 40 g of molecular tritium in a closed loop. In the case of an evidence for an electron antineutrino mass, the discovery potential of KATRIN depends on the neutrino mass found. E.g. the discovery potential of KATRIN is 5σ for a electron antineutrino mass of $m_{\bar{\nu}} = 0.3$ eV/c². In section 3.1 a detailed overview of the experiment's components is given and in section 3.2 the sensitivity of the experiment and its statistical and systematic uncertainties are discussed.

3.1. Main Components

The KATRIN experiment consists of different subsystems and an overview of the final setup is shown in figure 3.1. Like the Troitsk experiment KATRIN uses a Windowless

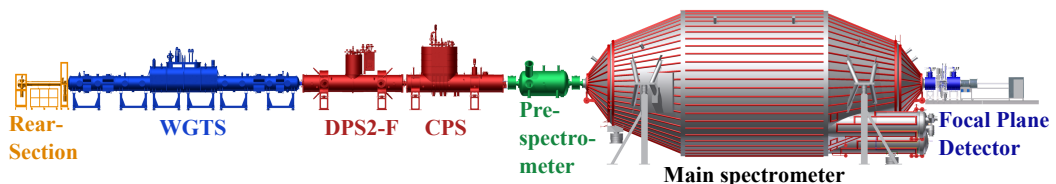


Figure 3.1.: **Setup of the KATRIN Experiment** with its different subsystems. The β -electrons are generated by a tritium β -decay in the source (WGTS) and magnetically adiabatically guided through a Differential Pumping Section (DPS2-F) and a Cryogenic Pumping Section (CPS) into two electrostatic retardation spectrometers. At the end of the setup the electrons are detected by a silicon PIN-diode detector array with a high detection efficiency. The Rear-Section is used to monitor the source parameters (From [39], mod.).

Gaseous Tritium Source (WGTS) for the controlled injection of the molecular tritium gas. Tritium that decays in the WGTS generates the β -electrons used for the neutrino mass measurement. The tritium and its daughter molecules are pumped out again at both ends of the WGTS and in the transport section, which connects to it. A detailed description of the WGTS is given in section 3.1.1. The transport section is mentioned in more detail in section 3.1.2 and is split into two parts. A Differential Pumping Section (DPS2-F) and a Cryogenic Pumping Section (CPS) are used to reduce the density of tritium gas, while the β -electrons are guided magnetic adiabatically on cyclotron trajectories through the transport section into two retardation spectrometers. The purpose of the pre-spectrometer is an event-rate reduction by a pre-selection of β -electrons with energies 200 eV close to the tritium endpoint of $E_0 = 18.6$ keV. The main spectrometer then performs a precision measurement of the energy of the β -electrons in the region of the endpoint. The measurement principle of the MAC-E filter spectrometers and their properties are discussed in section 3.1.3. By this measurement technique, only electrons with energies above the retardation potential can pass the analyzing plane of the main spectrometer and are counted by the FPD with a high detection efficiency. A short overview of the FPD system is given in section 3.1.4, while a detailed description of the system can be found in chapter 5.

3.1.1. Source

The 10 m long WGTS is located in the middle of the source cryostat and has a diameter of 90 mm. It is cooled to the $T = 30$ K regime by two cooling tubes on its outside containing boiling liquid neon that ensures a temperature stability of ± 3 mK needed to minimize Doppler-broadening from thermal influx. The molecular tritium gas with an isotopic purity of $\epsilon_T > 95\%$ is injected in a controlled manner into the middle of the WGTS. It is introduced through more than 250 holes at an injection rate of $q = 1.853$ mbar l/s ($\delta q/q \leq 0.1\%$) in order to keep turbulence of the gas small. The tritium gas diffuses continuously through the length of the WGTS within one second and is partly pumped out by six turbomolecular pumps of the DPS1-R and DPS1-F (Differential Pumping Section 1 - Rear / Front) located at both ends of the WGTS. This reduces the gas flow out of the source by a factor of 10^2 . The pumped out gas flows into the so-called 'inner loop' where it is refurbished and fed back to the WGTS for a reinjection. In this way, 40 g of tritium gas are introduced into the WGTS every day. Since the isotopic purity of the tritium gas has to be known to an accuracy of 0.1%, the composition of the gas is determined in the inner loop by Laser Raman-spectroscopy before it is reinjected into the WGTS [40]. Tritium gas, which is not pumped out by the DPS1-R or DPS1-F, reaches the transport section in the front or the Rear-Section in the back. The Rear-Section monitors the source activity during neutrino mass measurements with the use of a monitor-detector, while the activity can be measured with the FPD during measurement breaks with the use of the retardation potentials of the spectrometers. The strength of the WGTS is defined by:

$$N(T_2) = A_S \cdot \rho d \cdot \epsilon_T \quad (3.1)$$

With the source area A_S , the column density of $\rho d = 5 \cdot 10^{17}$ molecules/cm² (stable on a 0.1% level) and the tritium purity ϵ_T . The β -electrons emitted isotropically in the tritium decay are guided magnetic adiabatically on cyclotron trajectories through the WGTS, DPS1-R and DPS1-F with the guiding magnetic field provided by seven superconducting magnets ($B_S = 3.6$ T). With

$$\Phi = \int_A \vec{B} \cdot d\vec{A}, \quad (3.2)$$

the total magnetic flux tube in the source is given by $\Phi_{\max} = 229$ Tcm². To minimize the influence of β -electrons which scatter at the walls of the WGTS only the inner flux tube with $\Phi = 191$ Tcm² is analyzed. This corresponds to a magnetic flux of $B = 3.3$ T as it

is given at the FPD and results in a rate of 10^{11} β -electrons per second. A windowless gaseous tritium source offers highest luminosity and smaller systematic uncertainties than a quench condensed source and is therefore better suited for a long-term measurement like KATRIN [19], [39], [41].

While its different parts were tested by the manufacturers, the final assembly of the WGTS is planned to start in October 2012 at KIT and is scheduled to be finished in April 2014. In the final setup it will be located in the TLK, while the other subsystems are placed in the KATRIN hall and are connected to the WGTS via a feedthrough in the TLK safety wall.

3.1.2. Transport Section

In the transport section, which connects to the DPS1-F, a reduction of the tritium flow rate by 12 orders of magnitude to $q = \mathcal{O}(10^{-14})$ mbar·l/s is achieved. This results in 10^{-3} β -electrons per second generating a background by a tritium decay in the spectrometers. The β -electrons from the WGTS are guided on cyclotron trajectories through the DPS2-F and the CPS by 22 superconducting solenoids, which provide a magnetic flux density of $B = 5.6$ T.

In the DPS2-F four turbomolecular pumps with a pumping capacity of 2000 l/s for molecular hydrogen reduce the tritium flow by a factor of 10^5 . The pumped out tritium gas is fed back to the TLK by the so-called 'outer loop'. The cryostat of the DPS2-F is 7.2 m long with a beam tube 86 mm in diameter and cooled to 77 K by liquid nitrogen. With a tilt of 20° in the beam tube a direct line of sight from the WGTS to the spectrometers is prevented. This reduces the number of molecules in the residual gas which are guided into the spectrometers and increases the pumping efficiency. In addition, a ring-shaped electrostatic mirror at a potential of +100 V is located at the end of the DPS2-F, which backscatters positively charged ions. Without this mirror the ions would generate a background of a few kHz in the spectrometers by the ionisation of the residual gas. The trapped ions in the DPS2-F are deflected by electric dipoles and neutralized at the chambers walls. Two Ion Cyclotron Resonance Spectrometers, built into the DPS2-F, are used to monitor the ions in the beam tube and their deflection by the dipoles during measurement breaks [42], [19], [23].

The CPS follows the DPS2-F and reduces the tritium flow from the source by another factor of 10^7 by means of absorption of the tritium gas molecules on its walls. To enhance this absorption its beam tube is cooled by liquid helium to 4.5 K and a thin layer of argon frost covers its walls acting as a cryo-absorber for better trapping (3 K). To increase its trapping efficiency the beam tube of the CPS is tilted by 15° . During measurement breaks (\sim every 60 days) the beam tube is warmed up to 100 K and flushed with gaseous helium for regeneration and a new layer of argon frost is applied. A proof of principle for this kind of cryogenic pump is given by the TRAP experiment which was built as a test rig for the CPS at the TLK and reached a flow rate reduction factor of $3 \cdot 10^7$ for tritium [43]. With the Forward Beam Monitor Detector mounted to the CPS the source activity of the WGTS can be monitored during data-taking cycles by a measurement of the flux of electrons at the outer areas of the magnetic flux tube. In addition, the possibility for the optional installation of a quench-condensed tritium source or another electron source is given at the CPS for a survey of its spectrum or a calibration of the spectrometers [19], [44]. The CPS is built by ASG Superconductors S.p.A. and is expected to arrive at KIT in 2013. From the CPS the electrons are guided magnetically adiabatically into the pre- and main spectrometer.

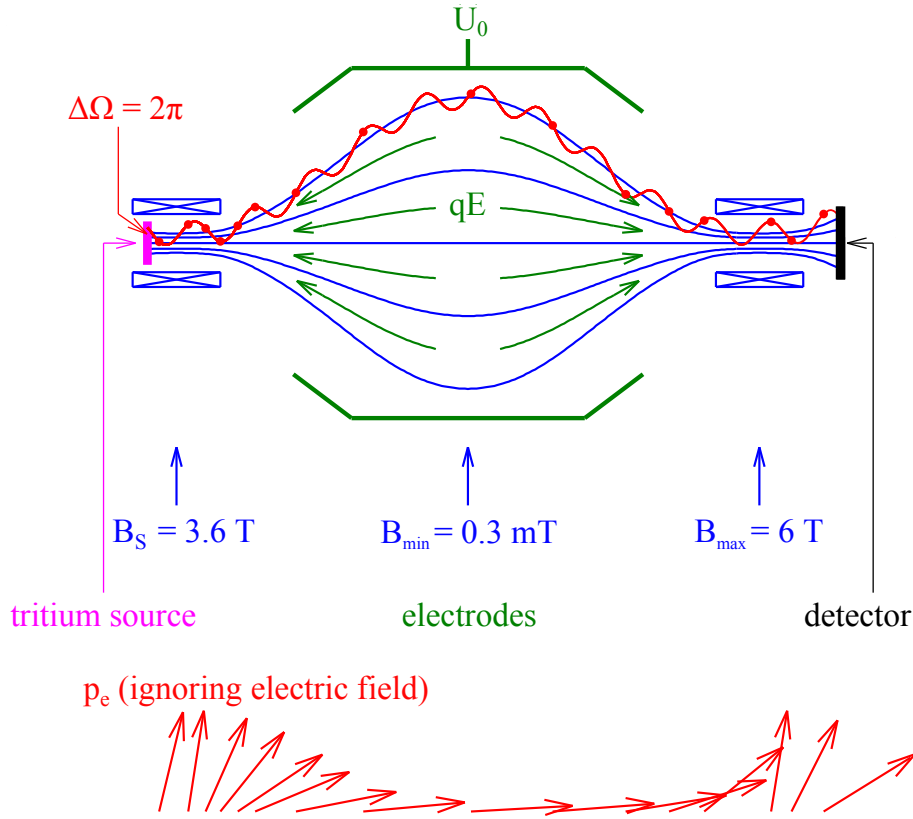


Figure 3.2.: **Illustration of the MAC-E Filter Principle.** The electrons are guided adiabatically on cyclotron trajectories (red) along the magnetic field lines (blue) from the tritium source towards the detector against the electric retardation potential (green). When they approach the analyzing plane in the middle of the spectrometer their momentum vector is turned into the direction of flight (see lower part of the figure) (From [19], mod.).

3.1.3. Spectrometers and the MAC-E Filter Principle

For a precise measurement of the β -electron energy close to the tritium endpoint the KATRIN experiment uses the MAC-E filter principle, which is well known from the experiments in Troitsk and Mainz. A MAC-E filter combines high luminosity with a low background and a high energy resolution [36] and its principle is illustrated in figure 3.2. The guiding magnetic field is generated by two superconducting solenoids at both ends of the spectrometer which provide a high magnetic flux density (B_{\max}). In the middle of the spectrometer, the so-called 'analyzing plane', the magnetic flux density reaches its minimum ($B_A \ll B_{\max}$). With equation (3.2) a broadening of the flux tube in the analyzing plane follows. During their magnetic adiabatic guidance on cyclotron trajectories the electrons are non-relativistic ($\gamma = 1.04$) and their magnetic moment is the invariant of motion:

$$\mu = \frac{E_{\perp}}{B} = \text{const.} \quad (3.3)$$

Here, E_{\perp} is the 'transverse' kinetic energy of the electrons defined by their transverse momentum. While the magnetic flux density decreases on the way from the ends of the spectrometer towards the analyzing plane, the magnetic moment of the electrons is constant in case their magnetic guidance is perfectly adiabatic. Therefore, the 'transverse' kinetic energy of the electrons has to decrease as well and is because of energy conservation transformed into 'longitudinal' kinetic energy E_{\parallel} . This means that the momentum vector of the electrons tilts towards the direction of flight when the electrons approach

the analyzing plane of the spectrometer. Since the retarding potential U_0 generated by cylindrical electrodes only influences the longitudinal momentum of the electrons, they need a 'longitudinal' energy of $E_{\parallel} > eU_0$ to pass the analyzing plane. Electrons with a too low 'longitudinal' energy are backscattered, whereas electrons which are able to pass the filter are reaccelerated by the retarding potential after the analyzing plane. This ensures that the electrons have their original kinetic energy distribution between 'longitudinal' and 'transverse' energy when they leave the spectrometer. Therefore, the MAC-E filter acts as a high energy-pass filter and measures in combination with a detector an integrated energy spectrum of the electrons. The energy resolution of a MAC-E filter is determined by the amount of maximum 'transverse' energy that electrons can still have in the analyzing plane. Therefore, it can be derived from equation (3.3) for an electron which has only 'transverse' energy $E_{\perp,\max}$ at the point of the maximum magnetic flux density B_{\max} :

$$\Delta E = \frac{B_A}{B_{\max}} \cdot E_{\perp,\max} \quad (3.4)$$

In the KATRIN experiment three spectrometers based on the MAC-E filter principle are used [19], [45]:

1. Pre-Spectrometer

The pre-spectrometer is located directly behind the transport section and is used for a pre-selection of the β -electrons before they reach the main spectrometer. Therefore it is held at a retarding potential of -18.4 kV and only electrons with an energy within 200 eV of the tritium endpoint can pass its analyzing plane. This results in a reduction of the flux of electrons coming from the source of two orders of magnitude to 10^4 s⁻¹. Its guiding magnetic field is provided by two superconducting solenoids with a magnetic flux density of $B = 4.5$ T. The pre-spectrometer is 3.4 m long with an inner diameter of 1.7 m in the analyzing plane and is held at Extreme High Vacuum (XHV) conditions with a pressure of 10^{-11} mbar by the use of turbomolecular- and getter-pumps [46], [19]. After its arrival at KIT in 2003, the pre-spectrometer was used for various test measurements as a prototype for the main spectrometer. These measurements included vacuum and cooling tests as well as background studies and improvements on the electromagnetic design. Since 2011, the pre-spectrometer has been located in the KATRIN hall and is being prepared for its connection to the main spectrometer.

2. Main Spectrometer

In the final KATRIN setup the main spectrometer connects to the pre-spectrometer and is held at a pressure of 10^{-11} mbar by a combination of cascaded turbomolecular pumps and non-evaporable getter-pumps. The pumps are located at three ports at the spectrometers rear end and have a total effective pumping speed of 10^6 l/s. The spectrometer is 23.3 m long with a maximal diameter of 10 m in the analyzing plane. Its guiding magnetic field is provided by the superconducting solenoid between main- and pre-spectrometer (4.5 T) and the Pinch Magnet at its rear side, with the highest magnetic flux density of the KATRIN experiment ($B_{\max} = 6$ T). This results in an asymmetric flux tube inside the spectrometer which is corrected by a system of air coils built around the spectrometer so that the flux tube fits into the vessel. A second system of air coils corrects for the earth's magnetic field. Since the magnetic flux density at the WGTS ($B_S = 3.6$ T) is lower than at the Pinch Magnet ($B_{\max} = 6$ T), electrons with polar starting angles of less than $\theta_{\max} = 51^\circ$ in the source are backscattered from the higher magnetic fields by the magnetic mirror effect, according to:

$$\theta_{\max} = \arcsin \left(\sqrt{\frac{B_S}{B_{\max}}} \right) \quad (3.5)$$

With a magnetic flux density of 0.3 mT in the analyzing plane of the spectrometer the magnetic flux tube has a diameter of 9 m according to formula (3.2). Equation (3.4) with $E_{\perp,\max} = 18.6$ keV and the maximum magnetic flux density of $B_{\max} = 6$ T gives an energy resolution of the main spectrometer of:

$$\Delta E = 0.93 \text{ eV} \quad (3.6)$$

Inside the main spectrometer's vessel a system of more than 28,000 wire electrodes is installed, which are held at a potential slightly higher than the vessel's walls. In this way the background from electrons emitted from the walls of the vessel can be kept small. To measure the integrated spectrum of the β -electrons close to the tritium endpoint E_0 with high precision, the retarding potential of the main spectrometer is varied in a region of $eU_0 = [-E_0 - 30, -E_0 + 5]$ eV. Since U_0 has to be known to a ppm-level at 18.6 kV, high precision voltage-dividers [47] are designed and built for the KATRIN experiment to enable a measurement of the retarding potential with a voltmeter. In addition, the voltage of the main spectrometer is monitored via the monitor-spectrometer [19]. After its shipment to KIT in 2006, the main spectrometer was tested to fulfill its XHV capabilities and by early 2012, the installation of the wire electrode system inside its vessel was finished.

3. Monitor-Spectrometer

To monitor the retarding potential of the main spectrometer the modified MAC-E filter from the Mainz experiment is used with the same potential applied as the main spectrometer. With the use of an implanted $^{83}\text{Rb}/^{83m}\text{Kr}$ -source it measures the spectrum of K-shell conversion electrons with an energy of 17.8 keV [48] during measurement cycles with KATRIN. Therefore, with the monitoring of the transmission function for the conversion electrons a monitoring of the main spectrometer retarding potential is possible [19].

3.1.4. Focal-Plane Detector

To count the electrons which passed the analyzing plane of the main spectrometer a Focal-Plane Detector with a high detection efficiency and a high background reduction is needed. A schematic view of the FPD system is shown in figure 3.3. To detect the electrons coming from the main spectrometer a segmented 148-pixel PIN diode fabricated on a single silicon wafer is used. The background reduction is realized by an active veto system, passive shielding as well as the use of construction materials with a low intrinsic activity in the detector system. In addition, the energy resolution of the FPD is aimed to be less than 1 keV (FWHM) to differentiate between background events and β -electrons from the main spectrometer. With a post-acceleration of the β -electrons of up to 30 kV in the FPD system a further reduction of the background is possible. The detector background is thereby reduced to less than 1 mHz in neutrino mass measurements. During calibration cycles the detector has to be able to handle high event rates of up to ~ 100 kHz, while the rates during neutrino mass measurements are only a few mHz [1]. The magnetic flux tube in the FPD system is provided by the Pinch Magnet ($B = 6$ T) and the Detector Magnet ($B = 3.6$ T) with a magnetic flux density of $B_{\det.} = 3.3$ T at the position of the detector wafer. A further description of the FPD system and its performance can be found in chapter 5.

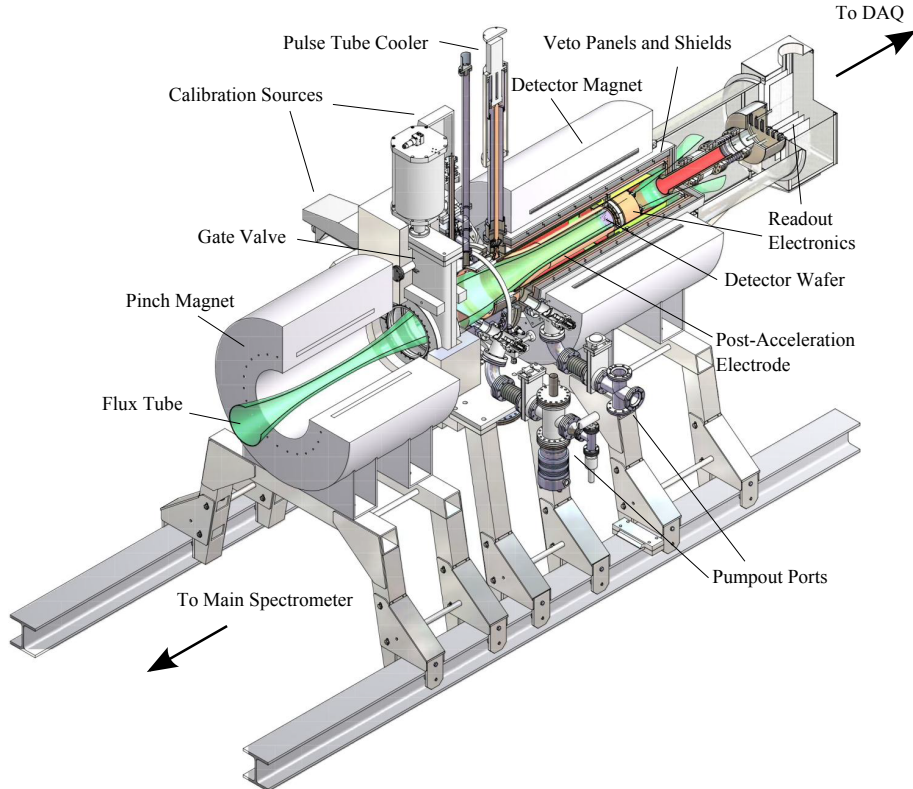


Figure 3.3.: Schematic View of the FPD System (From [1], mod.).

3.2. Sensitivity

To determine the electron antineutrinos mass with an one order of magnitude higher sensitivity than the earlier experiments in Troitsk and Mainz, the KATRIN experiment has to improve the statistical and systematic uncertainties by two orders of magnitude (see formula (2.26)). Therefore, the absolute uncertainty of KATRIN must not exceed:

$$\sigma_{\text{abs.}} = \sqrt{\sigma_{\text{syst.}}^2 + \sigma_{\text{stat.}}^2} \approx 0.025 \text{ eV}^2/\text{c}^4 \quad (3.7)$$

The requirements on the systematic uncertainties of the KATRIN experiment to reach this goal are discussed in section 3.2.1, whereas the statistic uncertainties are described in section 3.2.2.

3.2.1. Systematic Uncertainties

The goal of the KATRIN experiment is a systematic uncertainty of $\sigma_{\text{syst.}} = 0.017 \text{ eV}^2/\text{c}^4$ on the squared antineutrino mass $m_{\nu_e}^2$. To reach this goal a generation of all β -electrons under the same condition has to be ensured. Therefore, the source pressure and temperature as well as the isotopic purity of the molecular tritium have to be known to a 0.1% precision. In addition, secondary effects have to be taken into account, such as:

- radiative corrections of higher orders in the molecular tritium decay,
- the nuclear recoil energy of the tritium daughter molecules,
- the final state distribution of the tritium daughter molecules (investigated in the TRIMS-experiment [49]),
- the creation of tritium ions in the WGTS and the transport section,

- scattering of β -electrons with tritium molecules within the source,
- variations in the retarding potential,
- the synchrotron radiation of the electrons on their cyclotron trajectories,
- a Doppler-broadening due to the movement of the tritium column in the WGTS,
- penning traps in the electromagnetic design.

In addition, any non-adiabatic effects in the transport of the β -electrons through the experimental setup have to be taken into account [19].

3.2.2. Statistical Uncertainties

The effective measurement time of KATRIN is three years with a background of 10 mHz. A maximum statistical uncertainty of $\sigma_{\text{stat.}} = 0.018 \text{ eV}^2/\text{c}^4$ has to be achieved in the same range as the systematic uncertainty. It is determined by the count rate of β -electrons at the detector and is therefore dependent on the detection efficiency of the FPD. In addition, the column density in the WGTS of $\rho d = 5 \cdot 10^{17} \text{ cm}^{-2}$, the accepted polar angle of the β -electrons of 51° in forward direction as well as the lossless transport of the magnetic flux tube of $\Phi = 191 \text{ Tcm}^2$ through the experiment dominate the statistical uncertainty of KATRIN. While the statistical uncertainty decreases with an increasing ROI below the tritium endpoint the drawback of an increasing systematic uncertainty by inelastic interactions of the β -electrons with an increasing ROI has to be taken into account. Thus, a ROI starting 30 eV below the endpoint and ending 5 eV above it can be mentioned as a reference value. In addition, an improvement of $\sim 40\%$ for the statistical uncertainty of KATRIN can be reached by an optimization of the measurement cycles at different retarding potentials [19]. To ensure no influence of the detector dead layer on the uncertainty a calibration of the detector between the neutrino mass measurement cycles is necessary.

4. Physics of Semiconductor Diode Detectors

The FPD of the KATRIN experiment uses a 148-pixel PIN-diode array fabricated on a single silicon wafer to measure the β -electrons from the tritium decay. The major advantage of such a semiconductor diode detector compared to scintillation counters or gas-filled detectors is its high energy resolution. Since the statistical limit on the energy resolution of a detector is given by the number of information carriers generated per pulse, a semiconductor diode detector with its high amount of those can offer energy resolutions of up to 131 eV for incident radiation of 6 keV [50]. Besides this, semiconductor diode detectors offer other features such as a high detection efficiency, small sizes, fast timing characteristics and an effective thickness, which can be varied, to meet the demands of the experiment. In addition, the performance of semiconductor devices does not suffer significantly in the presence of high magnetic fields. After becoming practically available in the early 1960s, semiconductor diodes are used in most of today's particle detectors. After a short introduction to semiconductor physics in section 4.1 an overview of the semiconductor diode detectors used in the FPD system of KATRIN is given in section 4.2. A simulation package for low-keV electrons in silicon was developed within the KATRIN collaboration and is described in section 4.3. It allows high quality Monte Carlo simulations of the FPD response on electrons.

4.1. Semiconductors

After the discovery of the rectification effect of semiconductor materials by Ferdinand Braun in 1874, Felix Bloch derived the Bloch Theorem in 1928 [51], which provides a description of semiconductor properties by the so-called Band-Gap Model discussed in section 4.1.1. The combination of semiconductor materials with different properties allows a wide range of applications where the so-called p-n-junction forms the basis of most semiconductor devices. It is mentioned in detail in section 4.1.2 and builds the foundation for semiconductor diode detectors.

4.1.1. The Band-Gap Model

By the assumption of a periodic potential $V(\vec{r})$ inside a solid, generated by its crystal structure, the Schrödinger equation is given by:

$$\left[-\frac{\hbar^2}{2m} \nabla^2 + V(\vec{r}) \right] \Psi(\vec{r}, \vec{k}) = E(\vec{k}) \Psi(\vec{r}, \vec{k}) \quad (4.1)$$

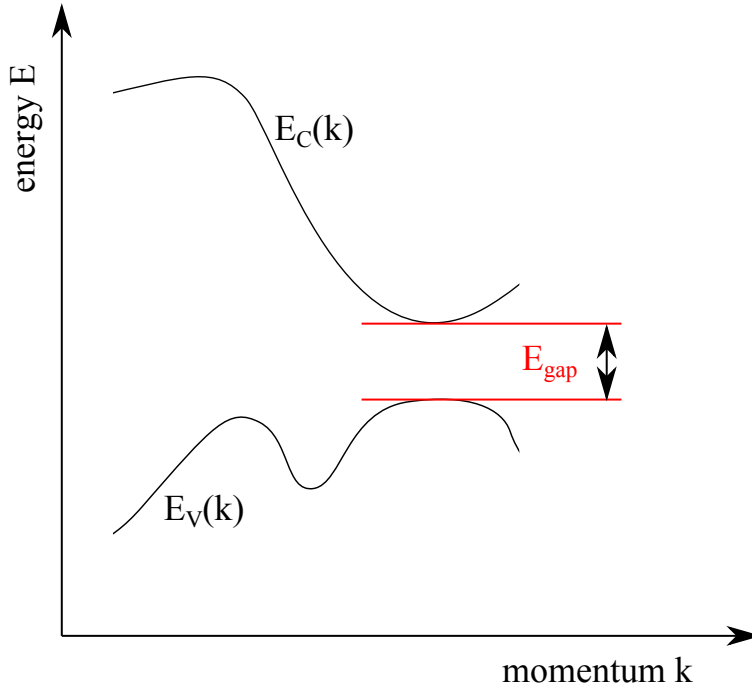


Figure 4.1.: Simplified Illustration of the Energy Band Gap in a Semiconductor.

Electrons in the valence band (E_V) are part of the covalent bond in the crystal lattice, while electrons in the conduction band (E_C) contribute to the conductivity of the material. Energies within the band gap (E_{gap}) are forbidden for the electrons.

According to Bloch's Theorem it can be solved by Bloch Functions:

$$\Psi(\vec{r}, \vec{k}) = \exp(i\vec{k}\vec{r}) \cdot U(\vec{r}, \vec{k}) \quad (4.2)$$

Here, $U(\vec{r}, \vec{k})$ is a periodic function within the crystal lattice. By solving the eigenvalue problem in formula (4.1) an energy-momentum relationship for electrons in the crystal can be derived, which defines distinct energy bands in the E-k-plane that the electrons can occupy. In the case of insulators or semiconductors band gaps with energies forbidden to the electrons exist [52]. In figure 4.1 a simplified illustration of the band gap for a semiconductor is shown. Here, the lowest energy band which is not fully occupied by electrons is called the conduction band E_C . It physically corresponds to free electrons in the crystal which contribute to the conductivity of the material. The so-called valence band E_V is the highest fully occupied energy band and corresponds to electrons which are bound in the crystal structure of the material, e.g. are part of the covalent bond in a bulk semiconductor. In the following, a simplified model of the energy bands in crystals is used where only one valence and one conduction band is assumed and a discrimination between direct and indirect band gaps is not made. In this model a distinction between insulators, semiconductors and conductors is given by the occupation of the energy bands and the size of the band gap in between.

- **Insulators:**

In an idealized insulator at a temperature of 0 K all energy levels in the valence band are occupied, while the conduction band is empty. The band gap between the bands is > 5 eV for an insulator and therefore, a great amount of thermal energy has to be introduced to the insulator to lift an electron from the valence band into the conduction band. Thus, insulators show a low conductivity even at room temperature.

Table 4.1.: Properties of Intrinsic Silicon and Germanium.

Property	Silicon	Germanium
Energy band gap (300 K)	1.115 eV	0.665 eV
Energy band gap (0 K)	1.165 eV	0.746 eV
Intrinsic carrier density (300 K)	$1.5 \cdot 10^{10} \text{ cm}^{-3}$	$2.4 \cdot 10^{13} \text{ cm}^{-3}$
Ionization energy ϵ (300 K)	3.62 eV	-

- **Semiconductors:**

At a temperature of 0 K an idealized semiconductor acts like an insulator. In this case, all energy levels in its valence band are filled and the conduction band is completely empty. In contrast to an insulator, the band gap of a semiconductor is relatively small ($< 5 \text{ eV}$). This allows a thermal excitation of valence band electrons into the conduction band at relatively low temperatures.

- **Conductors:**

In a conductor the conduction band is already partly filled at a temperature of 0 K and electrons can therefore be lifted to higher energy levels within the band by small thermal excitations. Thus, conductors have a high conductivity even at low temperatures.

Focusing on semiconductors a thermal excitation of a valence electron into the conduction band leaves a vacancy, a so-called 'hole', in the otherwise full valence band. This hole can be imagined as a net positive charged virtual particle. In the presence of an electric field valence electrons from covalent bonds close to the hole will preferably drift in the opposite direction of the electric field and fill this vacancy. But this leaves behind a new hole in their old covalent bond. Therefore, in the presence of electric fields holes drift in the direction of the electric field like positively charged particles would do. The combination of a thermally excited electron in the conduction band and the hole, which it left behind in the valence band, is called an 'electron-hole pair'. These represent the information carriers in a semiconductor diode detector. The most popular semiconductor materials used in modern detectors are based on silicon and germanium. While silicon is mostly used in the charged particle spectroscopy, germanium is used in the detection of gamma-rays. In table 4.1.1 the most important semiconductor properties of intrinsic silicon and germanium are listed.

The theoretical model derived up to this point can only describe pure semiconductor materials such as silicon or germanium. These materials are called intrinsic semiconductors. In reality the electric properties of a semiconductor are mainly dominated by small levels of residual impurities in the material. For semiconducting materials in common use for particle detection, a doping of the intrinsic material with impurities is intended to vary their resistivity. A differentiation between two kinds of doping can be made:

- **n-Type Semiconductors**

Pure silicon is located in the fourth main group of the periodic table. In its crystal lattice all four valence electrons of a silicon atom are part of the covalent bond to the four nearest neighbour atoms. A thermal excitation in the intrinsic material consists therefore in breaking loose one of the covalent bonds. If a small concentration of impurities from the fifth main group of the periodic table (e.g. phosphorus) exists in the silicon, its atoms will be embedded within the crystal lattice. However, their fifth valence electron does not contribute to the covalent bond and therefore, it is only loosely bound. Thus, only a small thermal excitation is needed to break it loose. In the Band-Gap Model of a semiconductor the loosely bound electrons form an energy

level within the forbidden band gap directly below the conduction band. These impurities are called 'donor impurities'. Semiconductors which are actively doped with those impurities are called 'n-type semiconductors'. In such a semiconductor the number of conduction electrons (majority carriers) is higher than the number of holes (minority carriers).

- **p-Type Semiconductors**

In case pure silicon is doped by impurities from the third main group of the periodic table (e.g. thallium), one electron is missing in the covalent bond of the impurity atom to the surrounding silicon atoms in the crystal lattice. Electrons from other covalent bonds within the lattice only need a small thermal excitation to fill this vacancy. Therefore, the impurities are called 'acceptor impurities'. Since the binding of an electron to such an impurity is slightly less than the binding to a silicon atom in the lattice, the acceptor impurity forms an energy level within the forbidden band gap right above the valence band. Semiconductors which are doped with acceptor impurities are called 'p-type semiconductors' and the conductivity of these materials is dominated by holes (majority carriers) rather than by electrons (minority carriers).

If the concentration of donor and acceptor impurities is equal, the material will have some of the properties of an intrinsic semiconductor and is called 'compensated'. Because of their nearly intrinsic properties, these materials are denoted as 'i-type semiconductors'. The total concentration of charge carriers in a n-type or p-type semiconductor is higher than in the intrinsic material. If thin layers of semiconductor materials have an extremely high concentration of impurities, they will have a very high conductivity and are denoted as ' $n^{(+)}$ -type semiconductors' or ' $p^{(+)}$ -type semiconductors'. In semiconductor diode detectors these materials are often used to make an electrical contact to the readout electronics. If a charged particle passes through a semiconductor material, it will generate electron-hole pairs along its path. The number of these pairs depends on the ionization energy ϵ of the material. With $\epsilon = 3.62$ eV at 300 K, the ionization energy for silicon is by one order of magnitude smaller than in gas-filled detectors. Therefore, ten times more information carriers (charge carriers) are created in a semiconductor detector. This results in a higher energy resolution, since the statistical uncertainty on the energy deposited in the detector by the passing particle decreases with an increase of information carriers. In addition, a greater amount of charge is generated and contributes to the detection pulse which increases the signal-to-background ratio. To collect the information carriers at the boundaries of the semiconductor a voltage of a few hundred volts has to be applied to it. For a single i-type, p-type or n-type semiconductor this voltage results in a leakage current due to the small but non-zero conductivity of the material, which is superimposed on the detection pulse. Therefore, the leakage current of the detector has to be reduced to the nA-scale by so-called 'blocking contacts'. The commonly used blocking contact in a semiconductor detector is the junction of a p-type and a n-type semiconductor called 'p-n junction' [53].

4.1.2. The p-n Junction

The properties of a p-type and a n-type semiconductor brought together in good thermodynamic contact, especially the characteristics close to the junction surface, form the basis for modern semiconductor diode detectors (note that the p-n junction is nothing else than a diode). While the p-part has a high concentration of acceptor impurities, the n-part has a high surplus of loosely bound electrons. Therefore, these electrons drift from the n-side to the p-side by a diffusion process where they fill the vacancies in the covalent bonds of the acceptor impurities. In addition, a diffusion of free holes from the p-region into the n-region takes place where they recombine with electrons. Since this diffusion process

leaves ionized donor impurities in the n-side and a surplus of electrons in the p-side, a positive space charge in the n-part and a negative space charge in the p-part of the junction is generated. This results in an electric field within the p-n junction which is, when the thermal equilibrium is reached, just strong enough to stop the diffusion process and results in a steady-state charge distribution. The region over which this charge imbalance exists is called 'depletion zone'. Its extension into the p-region and n-region of the junction depends on the particular doping of the sides (i.e. a lower doping results in a larger extension of the depletion zone). The potential difference across the junction (contact potential) can amount to nearly the full band gap value of the semiconductor material.

The properties of the depletion region are very attractive for a detection of radiation. When a charged particle passes through, it will create electron-hole-pairs along its path. The electric field across the p-n junction will cause these electrons and holes to drift towards the end of the n-side (p-side) where they can be collected as an electric charge. The height of this charge pulse is proportional to the energy of the particle which passed through. Nevertheless, an unbiased p-n junction has a contact potential of ~ 1 V for silicon, which is by far not enough to ensure an effective collection of the created electron-hole pairs. More likely, the electrons and holes recombine within the junction before they can be collected at its ends. In addition, the depletion zone of an unbiased junction is quite small and it has a high capacitance. Therefore, its noise properties are poor when it is connected to the input stage of a preamplifier. To prevent this, in usual semiconductor detectors a 'reversely' biased p-n junction is used rather than an unbiased junction.

If an external bias voltage is applied to the junction in the reverse direction, i.e. a negative voltage is applied to the p-side of the diode in respect to the n-side, the contact potential in the depletion zone will be enhanced and the depletions zone will get broader. Modern semiconductor diode detectors are operated with a bias voltage which is large compared to the contact potential. Therefore, they have a large active detection volume (depletion zone). If the reverse bias voltage gets too high, a sudden breakdown (avalanche-breakdown) in the junction will occur with often destructive results. Thus, a monitoring of e.g. the leakage current of the detector is needed to ensure no overbias of the diode. In addition, a broadening of the depletion zone reduces the capacitance of the diode. This allows for a better energy resolution under conditions where electronic noise is dominant. Since the time, which is needed to collect the information carriers is in the ns-range, semiconductor diode detectors are one of the fastest-responding detectors commonly used in particle physics. Most of the semiconductor diode detectors are operated in fully depleted mode where the bias voltage is set high enough (depletion voltage) to ensure the depletion zone covers the whole thickness of the detector wafer. In this case a finite electric field through the whole wafer is guaranteed, which increases in its absolute value with the bias voltage. This results in a better charge collection and therefore, in a better timing and energy resolution of the detector [53].

4.2. Silicon PIN-Diode Detectors

At a given bias voltage the depletion zone of a silicon diode detector can be extended by the insertion of a mildly doped or intrinsic layer (i-type semiconductor) between the p-type and n-type layers forming a so-called PIN-diode (PIN stands for p-type, i-type, n-type). Since in the intrinsic middle layer the concentration of free charge carriers is small, it has a high resistance and nearly the whole bias voltage drops here. This results in a high electric field in the i-type region with sharp edges at the p-i and i-n borders. The lifetime of charge carriers created in this active region of the detector is much greater compared to the time required to collect them. This results in good charge collection properties of a PIN-diode detector and therefore, good timing and energy resolutions. It should be noted

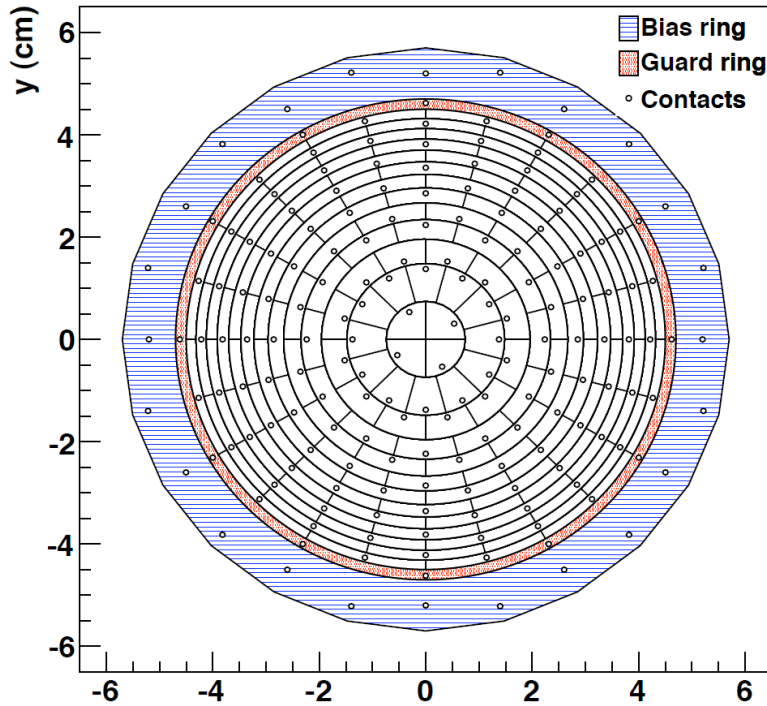


Figure 4.2.: **Mask of the FPD Pixel Pattern** surrounded by the bias ring (blue) and the guard ring (red). The electric contact points of the readout pogo-pins are shown as circles (From [1]).

that the intrinsic layer in PIN-diode detectors is usually mildly n-doped and the two other layers are heavily doped (p^+ , n^+). With an increasing bias voltage the depletion zone of the PIN-diode grows from the p-n junction between the p^+ -layer and the mildly doped n-layer and extends through the whole n-layer when the bias voltage reaches the depletion voltage. In the FPD system of KATRIN two kinds of silicon PIN-diode detectors are used, the FPD wafer and the Multi-Pixel Photon Counters (MPPCs) of the veto system. While the detection principle of the FPD wafer is discussed in section 4.2.1, the MPPCs are mentioned in section 4.2.2.

4.2.1. The FPD Wafer

The FPD is built on the basis of a n-intrinsic silicon wafer with a homogeneous n^{++} -doped blocking contact entrance side facing the main spectrometer. On its backside a p^{++} -doped pixel array of 148 pixels according to the mask in figure 4.2 is applied. In figure 4.3 a schematic draft of a cut through the wafer is shown. The wafer has a total thickness of $503\ \mu\text{m}$ which is chosen as a trade-off between the intrinsic detector background and the energy resolution of the detector determined by the input capacitance into the readout electronics. In addition, the wafer needs a reasonable thickness to withstand the mechanical stress induced by the custom-made readout scheme of the FPD system by means of pogo-pin contacts to the readout electronics. According to [54] no indication for performance changes of the detector due to this mechanical stress is found. The wafer is manufactured by Canberra Semiconductor NV (Belgium) in a double-sided process which combines photolithography and ion implantation. All electric contacts to the wafer are located on its backside (readout side). Therefore, the bias voltage applied on the backside of the wafer to a 'bias-ring' is fed around the edge of the wafer to reach the n^{++} -entrance side. A 'guard ring' structure between the detector pixels and the bias ring allows breakdown voltages of the diode that are several times higher than the depletion voltage.

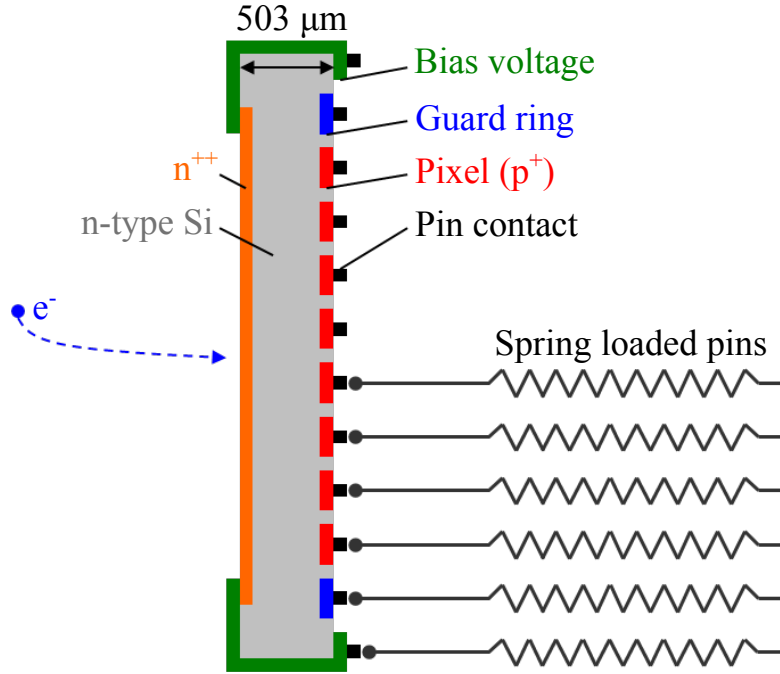


Figure 4.3.: Schematic Draft of the FPD Wafer.

In addition, the guard ring is held at a signal reference potential to suppress surface leakage currents between the outer pixels and the bias ring. Thus, leakage currents of $I_{lc} \ll 0.1 \text{ nA}$ at $T = -100 \text{ }^{\circ}\text{C}$ can be reached and a monitoring of the currents provides information about the detector performance. While the n^{++} -entrance side has no metalization applied to it to maximize the detection efficiency, the pixels as well as the guard and bias ring on the backside are coated by a thin layer of TiN to make ohmic contact to the readout electronics and the bias voltage. TiN is chosen because it is non-oxidizing and has low background properties [55], [54], [56], [53]. A further discussion about the FPD, especially about the readout electronics and the performance of the detector at KIT, is given in chapter 5.

4.2.2. The Veto MPPCs

To detect the light from the veto panels, which is created by cosmic muons passing through, Hamamatsu S10362-11-050P MPPCs are used. The MPPCs consist of an array of 400 avalanche diode detectors (pixels) where each pixel is operated in the so-called 'Geiger Mode'. The effect of an avalanche breakdown in a diode is already mentioned in section 4.1.2. At bias voltages above the breakdown voltage electron-hole pairs created in the depletion zone will gain enough kinetic energy by the high electric field that they can create additional pairs. This process multiplies the number of charge carriers and an avalanche of carriers is generated which forms a detectable pulse. If the bias voltage is high enough so that the multiplication regions of various interactions in the depletion zone merge together to form a single avalanche, the diode will be denoted to work in Geiger Mode. In this case the charge produced by a single event in the depletion zone is in principle multiplied without limit, which results in a high output pulse. Diodes which are operated in Geiger Mode have to be built, so that the avalanche process does not have destructive consequences. Since the avalanche effect is self-sustaining in Geiger Mode, it must be quenched by an external circuit. In terms of the MPPCs used for the FPD veto this is realized by quenching resistors. Diode detectors operating in the Geiger Mode pro-

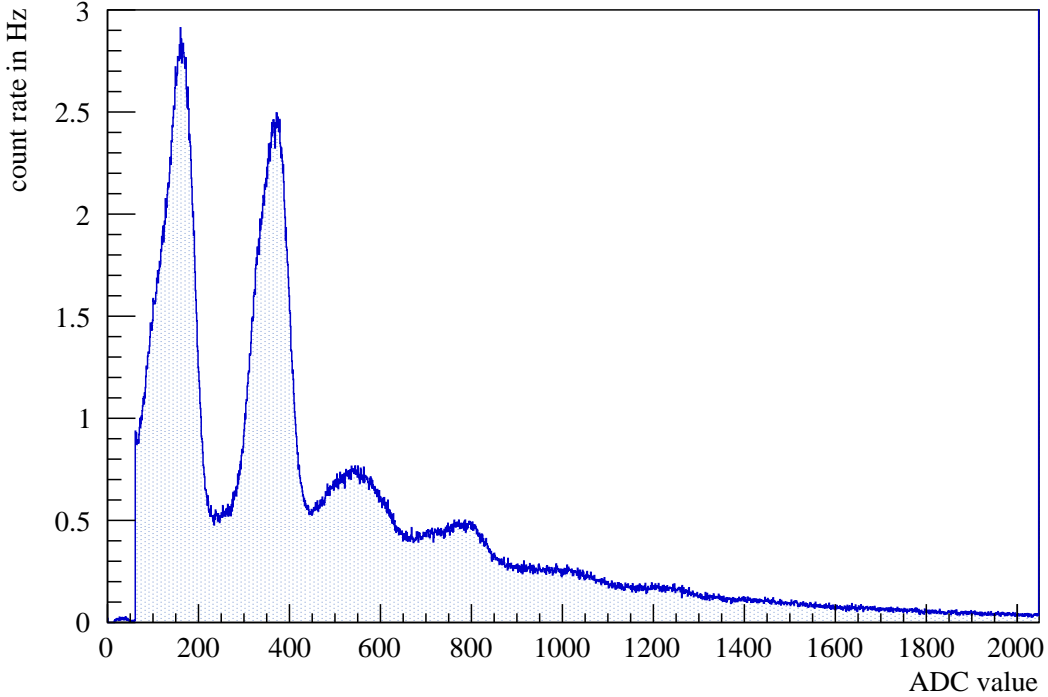


Figure 4.4.: **Dark Rate Spectrum of MPPC (#8)** without a connection to the veto panels and at a temperature of -18 °C. The bias voltage of the MPPC was set to 68.6 V.

vide an internal gain of up to 10^6 which increases with the bias voltage. The disadvantage of the Geiger Mode is the loss of any information about how many photons struck the diode detector, since the avalanches of different events merge. Thus, to recover this information large arrays of these diodes are used as in the MPPCs of the FPD veto. In case of a pulse of incident photons the small size of each diode (pixel) increases the probability that only one of the photons will hit one of the pixels. Since the gain of the different pixels is nearly the same, the summed output signal of all pixels is therefore proportional to the number of incident photons. In a spectrum of the MPPCs output the different peaks, corresponding to multiple cells firing, are clearly separated.

The bias voltage needed for a good performance of a MPPC depends strongly on its temperature. With rising temperature the vibrations in the crystal increase and so does the probability for carriers striking the crystal before an avalanche effect can take place. Therefore, a reliable biasing circuitry must be designed to guarantee a stable operation of the MPPCs. Since a diode in Geiger Mode is in an unstable condition it is very sensitive to thermal excitations in its depletion zone. This adds a random noise component to the spectrum of a MPPC output, called 'dark rates'. The dark rates of a MPPC can be as large as 10^6 pulses per second per mm^2 at room temperature. While an active cooling helps to reduce the dark rates, a discrimination level corresponding to the simultaneous firing of multiple pixels of the MPPC is necessary to reduce the dark rates to a reasonable level. In figure 4.4 a dark rate spectrum of the veto MPPC #8 is shown at a temperature of -18 °C. The multiple peaks in the spectrum correspond to one, two, three, a.s.o. pixels of the MPPC firing within the minimum timeframe which can be resolved by the veto system. Besides the thermal excitations, the dark rate of a MPPC is a complex interplay of additional effects such as afterpulsing or optical crosstalk. The MPPCs used in the FPD veto system consist of a p^+ -doped entrance side for the photons, a mildly p-doped layer

Table 4.2.: Properties of the FPD Veto MPPCs. The values are taken out of the manual for the Hamamatsu S10362-11-050P MPPCs [58].

Property	Value
Active area	1×1 mm
Number of pixels	400
Pixel size	50×50 μm
Peak sensitivity wavelength	440 nm
Photon detection efficiency	50%
Operating voltage	70 ± 10 V
Dark rate (room temp.)	400 kcps
Gain	$7.5 \cdot 10^5$

in the middle and a n⁺⁺-doped readout side [53], [57]. Their properties are listed in table 4.2.2. A further description of the FPD veto system and its performance at KIT can be found in chapter 5.

4.3. Simulation of Low-keV Electrons in Silicon

To simulate the detector response of a silicon diode detector to low keV electrons a Monte Carlo simulation package called KESS (KATRIN Electron Scattering in Silicon) was developed within the KATRIN collaboration. The package is embedded in the global KATRIN simulation program KASSIOPEIA [59] and validated by a detailed comparison to experimental data. Originally written in Fortran, the code was translated to C++ from 2008 on until KESS was included into KASSIOPEIA in 2010. The Monte Carlo is event-based and tracks an electron step-by-step on its path through the silicon bulk material. The bulk is thereby split into a dead layer and a second layer, the sensitive volume. KESS is especially configured to simulate electrons with energies of 0 - 50 keV in silicon, since commonly used simulation packages do not provide sufficient results for detailed energy distributions of backscattered electrons in combination with a very thin dead layer. In figure 4.5 and figure 4.6 the simulation results of the commonly used packages 'Geant4' [61] and 'Penelope08' [62] are shown. While both simulation packages provide acceptable results for a wide range of applications, their accuracy for low-keV electrons in silicon is not sufficient for the KATRIN experiment.

To configure the settings for a simulation with KESS the user can specify parameters, exit conditions, calculation methods, etc. in a configuration file. An example of such a configuration can be found in table A.6 in the appendix. The simulation is managed by the KESSRunManager which reads-in the settings from the configuration file and each primary KESSElectron is submitted to the run manager, which creates a KESSTrack for it. In KESS electrons are tracked step-by-step and at the end of each step an interaction takes place and the exit conditions defined in the configuration file are checked. The smallest unit of the simulation is therefore the KESSStep which determines all relevant physical processes and moves a KESSElectron according to its properties (such as its energy, angle, etc.). A KESSTrack is a collection of KESSSteps and saves information about the beginning and the end of the track of a given KESSElectron. In addition, it stores the energy deposition of the electron as well as its exit condition. Primary electrons as well as secondary electrons, created in inelastic processes, are stored in a KESSTrack.

In the following the physical processes included in KESS are mentioned [56], [59]:

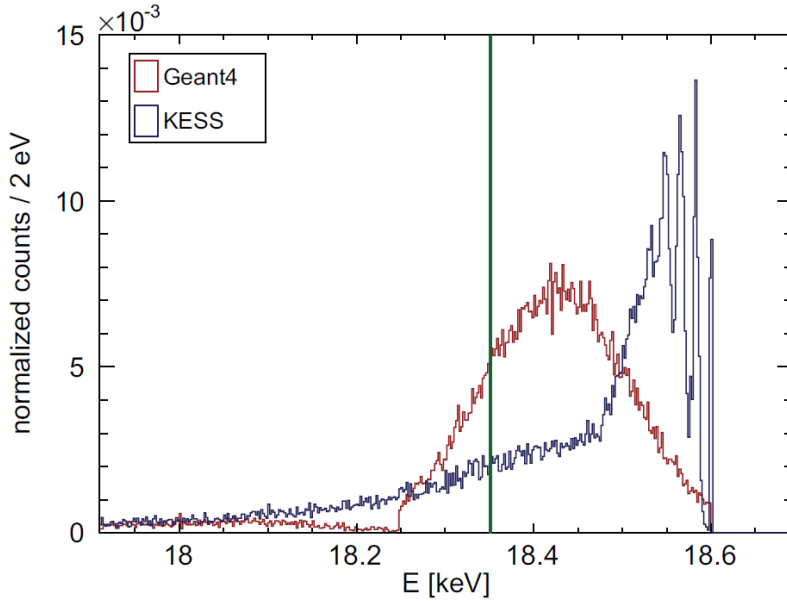


Figure 4.5.: **Comparison of a Geant4 Simulation with a KESS Simulation** for the energy distribution of monoenergetic 18.6 keV electrons after 100 nm of bulk silicon. While Geant4 approximates the energy losses in silicon by a straggling around an average energy loss details of single energy losses are visible in the KESS result. The vertical green line is not of interest in this thesis (From [56]).

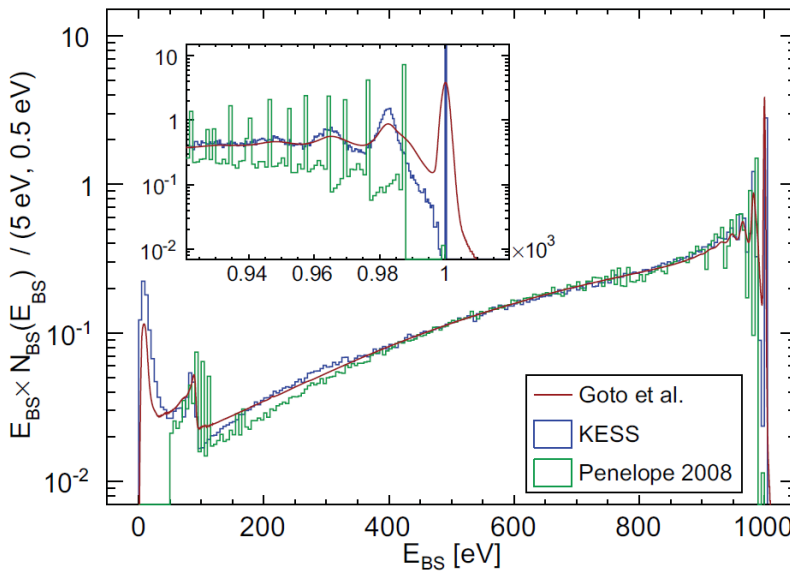


Figure 4.6.: **Comparison of a KESS Simulation with Penelope08 and Experimental Data**[60] for the energy distribution of backscattered electrons. The energy of the incident electrons is 1 keV. The experimental energy resolution was not applied to both simulations to demonstrate the artifacts in the high energy peak of the Penelope08 results (From [56]).

- **Elastic Scattering:**

Electrons which scatter with the silicon atom potential change their direction depending on their energy but will not lose energy when the scattering is elastic. The data tables used for the elastic scattering processes are generated by the ELSEPA software [63], which is based on relativistic partial wave expansions and the Dirac-Fock atomic potential. Energy values in the range of 1 eV to 400 keV are included in the tables.

- **Inelastic Scattering:**

If the electron scatters inelastically with a silicon atom potential, up to half of its energy can be transferred to a shell electron of the silicon atom. Thereby, the energy loss depends on the incident energy of the electron. To calculate the mean free path and the probability density functions for an inelastic scattering KESS uses the Penn Formalism [64] which includes effects such as bulk plasmon excitations, inter-band transitions and inner-shell ionization. If the energy loss of the electron is great enough, it can be transferred to K- or L-shell electrons of the silicon atom which results in a creation of a secondary electron and an ionization of the silicon atom. The secondary electron can optionally be tracked with KESS, as well and will produce further scatterings, ionizations, etc. If the energy of the incident electron is small enough, it will be transferred to a M-shell electron and will lead to an excitation of the valence band.

- **Atomic Relaxation of Silicon:**

An ionized silicon atom relaxes through the Auger and the Coster-Kronig effect where electrons from outer shells fill the vacancy in an inner shell. The energy released in this process is transferred to another electron which is subsequently emitted. This results in a cascade of secondary electrons which are emitted in spherical symmetry. A relaxation of the ionized silicon atoms through fluorescence is neglected in KESS.

- **Transmission Probabilities:**

When an electron enters the silicon bulk its base potential changes. This potential change is nothing else than the energy difference between vacuum and the conduction band minimum in silicon and is called the electron affinity χ . The potential change can be approximated as a step with height χ where the electron affinity for silicon is $\chi_{\text{Si}} = 4.05 \text{ eV}$. This effect is important for secondary electrons with $E < 50 \text{ eV}$ in particular.

An application example of KESS can be found in chapter 6 where it is used to determine the dead layer of the FPD wafer by a χ^2 -comparison of a simulated detector response and data from an energy loss measurement with the FPD system.

5. Assembly and Performance of the Focal-Plane Detector System at KIT

The Focal-Plane Detector (FPD) system was designed and built at the University of Washington (Seattle, USA) in collaboration with the Massachusetts Institute of Technology (Boston, USA), the University of North Carolina (Chapel Hill, USA) and the Institute for Data Processing and Electronics (at KIT). It was tested and successfully commissioned in spring 2011 and after its disassembly shipped to KIT in June 2011. One major issue of this thesis is the assembly of the FPD system at the KATRIN main spectrometer hall together with the KATRIN Detector Task Group as well as tests to ensure the fulfillment of its design criteria. A picture of the fully assembled FPD system at KIT is shown in figure 5.1. In the following the design criteria of the system will be presented in section 5.1. An overview of the FPD system and especially of its performance at KIT is given in section 5.2. In this context upgrades of the system, which are planned to be installed in 2012, are mentioned.

5.1. Background Requirements for the FPD System and the Figure of Demerit

During neutrino mass measurements with KATRIN the FPD has to count the β -decay electrons close to the tritium endpoint, which pass the retarding potential of the main spectrometer. Therefore, it has to fulfill high criteria in detection efficiency and background reduction to allow a sensitivity of $m_{\bar{\nu}} \leq 200 \text{ meV}/c^2$ for the KATRIN experiment. To reduce the background from radioactive materials in the detector region the FPD system is built out of materials with a low intrinsic activity wherever possible. In addition, all sources of radiation, e.g. the readout electronics are spatially separated and shielded from the detector wafer. These design constraints result in the FPD system being a complex apparatus from a physical and technical point of view.

The optimum performance of the detector system requires a balance of several parameters. These contain the detector's intrinsic background, its energy resolution, the ROI in its response spectrum and its detection efficiency, which is for example dominated by the dead layer of its wafer. Some of these parameters influence each other, e.g. a better energy resolution allows a smaller ROI in the response spectrum. To combine these parameters with their benefits and drawbacks in a single value the Figure of Demerit was introduced for the FPD system. Besides this balancing it allows a separation of the sources for the

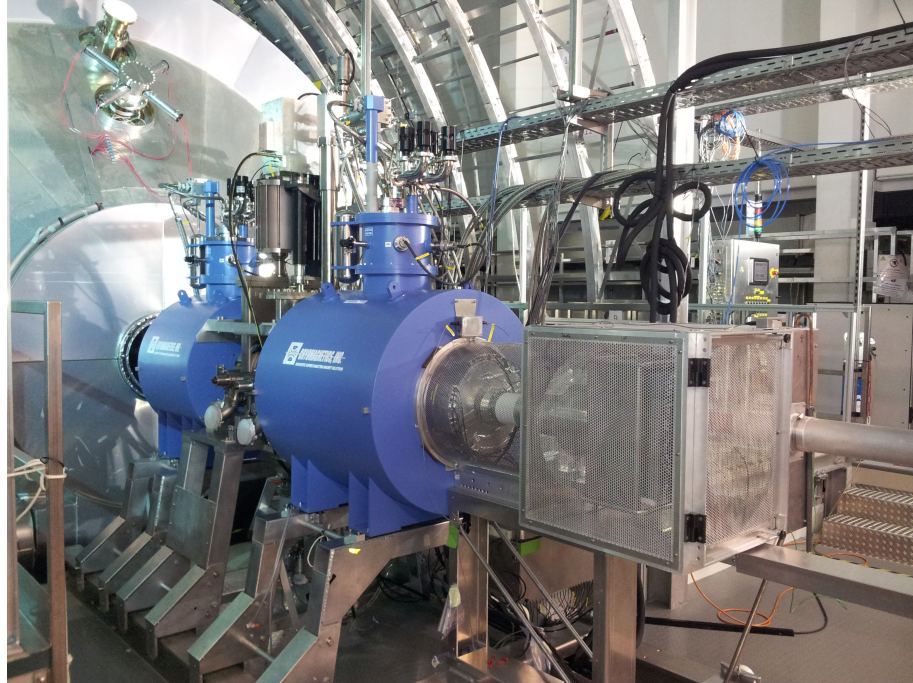


Figure 5.1.: The FPD System Installed at KIT prior to its connection to the main spectrometer. The Data Acquisition Crate and the High Voltage Crate are out of the picture on the right hand side.

statistical uncertainty of KATRIN from the detector parameters and from other parts of KATRIN such as the main spectrometer background. To ensure an optimal measurement the Figure of Demerit has to be minimized. According to [36], the statistical uncertainty for the square of the neutrino mass $m_{\bar{\nu}}$ in a given ROI in the detector response spectrum with an upper (E_U) and lower (E_L) bound is given by:

$$\sigma(m_{\bar{\nu}}^2) = \frac{k \cdot b(E_L, E_U)^{1/6}}{r^{2/3} \cdot t^{1/2}} \quad (5.1)$$

Here, $k = (16/27)^{1/6}$ is a constant, t is the measurement time, r (Hz/eV³) is the normalized count rate of tritium endpoint electrons coming from the main spectrometer and $b(E_L, E_U)$ is the total background rate in Hz integrated over the ROI. The background rate is a sum of the background rate b_{MS} from the main spectrometer, which is assumed to be constant [19], and the integrated intrinsic background rate b_{Det} of the detector. Since the backgrounds of the main spectrometer and the detector as well as the tritium endpoint energy are assumed to be known to perfect accuracy and to be independent from each other, this formula is idealized. Due to the limited energy resolution of the detector as well as its detection efficiency only a fraction of the incident electrons with energies in the ROI will contribute to a peak in the detector response spectrum within the same ROI. To correct for these effects a factor $f(E_L, E_U)$ is introduced denoting the fraction of the count rates r on the detector which fall into the ROI in the detector response peak. While the background rates b_{MS} from the main spectrometer have to be corrected by this factor as well, the intrinsic background rate b_{Det} of the detector does not depend on it and formula (5.1) changes to:

$$\sigma(m_{\bar{\nu}}^2) = \frac{k \cdot b_{MS}^{1/6}}{r^{2/3} \cdot t^{1/2}} \cdot \frac{\left(f(E_L, E_U) + \frac{b_{Det}(E_L, E_U)}{b_{MS}} \right)^{1/6}}{f(E_L, E_U)^{2/3}} \quad (5.2)$$

The Figure of Demerit F is defined as:

$$F = \frac{\left(f(E_L, E_U) + \frac{b_{Det}(E_L, E_U)}{b_{MS}} \right)^{1/6}}{f(E_L, E_U)^{2/3}} \geq 1 \quad (5.3)$$

and includes the intrinsic detector background rates as well as its energy resolution, its detection efficiency and the ROI in the detector response spectrum. Thus, by minimizing F, the combination of these parameters needed for the lowest possible statistical uncertainty on the square of the neutrino mass can be found [65]. To satisfy the KATRIN design goal, the Figure of Demerit has to be $F < 1.1$. While comprehensive background and detection efficiency measurements at KIT have yet to be done, the commissioning data in Seattle gives a limit for the Figure of Demerit of $F < 1.2$ with veto and multi-pixel cuts applied [1].

5.2. Main Components and their Performance

The KATRIN FPD system consists of different subsystems which are explained in the following. Since the main spectrometer will expand by ~ 12 cm during its 350°C bake-out, the whole FPD system is installed on rails in order to accommodate this movement.

5.2.1. Magnets

The magnetic flux tube in the detector region is defined by two superconducting solenoids, the Pinch Magnet and the Detector Magnet built by Cryomagnetics, Inc, of Oak Ridge, Tennessee. Each magnet has its own warm bore cryostat and is capable of delivering 6 T as a maximum field, while the nominal fields during normal operation are 6 T (Pinch Magnet, current of 87.15 A) and 3.6 T (Detector Magnet, current of 56.15 A). Thus, during neutrino mass measurements the Pinch Magnet provides the largest guiding magnetic field in the beamline of the KATRIN experiment. It constrains the magnetic flux tube at the end of the main spectrometer and is therefore part of its MAC-E filter. Placing the maximum field at the end of the main spectrometer ensures that trapped electrons inside the spectrometer will preferentially escape towards the source. This will help to reduce the background rate coming from the main spectrometer. To image the entire analyzing plane onto the detector wafer a second magnet, the Detector Magnet, is needed. During usual operation it delivers a magnetic field of 3.3 T at the detector wafer, which sits 16 cm downstream of the magnets center in its warm bore. The cryostats of both magnets are equipped with a Cryomech PT410 Pulse Tube Cooler (PTC) for helium recondensing and operate at a nominal temperature of 4.2 K. Under usual working conditions there is no measurable loss of liquid helium. The magnet coils consist of a twisted multifilamentary NbTi/Cu wire including a bare NbTi persistent switch. This allows operation either in persistent or driven mode. The attractive force between the magnets at full field (6 T each) is 54 kN. Therefore, aluminum spreader bars are required to separate the magnets.

Apart from a 'training' quench of the Detector Magnet after its transportation in summer 2011, right after the startup of the magnets they work fine and were tested together at their maximum fields of 6 T. In figure 5.2 the drift of the Pinch Magnets field with time is shown. It was measured with a Nuclear Magnetic Resonance (NMR) probe inside the Pinch Magnets warm bore at a field of 6 T (Pinch Magnet) and 3.6 T (Detector Magnet) in persistent mode. The drift is 0.0015% per month [66], well within the KATRIN design goal of 0.1% per month [1].

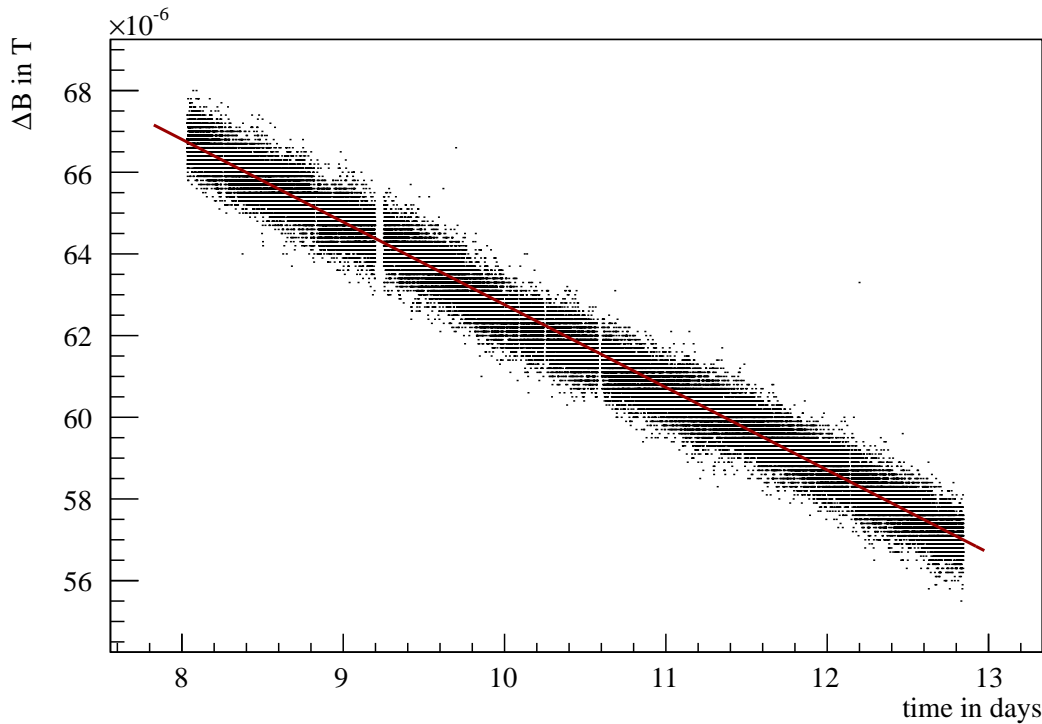


Figure 5.2.: The Drift of the Pinch-Magnet's Field with Time in Persistent Mode
 was measured with a Nuclear Magnetic Resonance (NMR) probe inside the Pinch Magnets warm bore over a period of ~ 5 days at a magnetic field of 6 T (Pinch Magnet) and 3.6 T (Detector Magnet). For a better illustration the magnetic field $\Delta B = B_0 - 6.0688$ T is shown where B_0 is the actual field measured with the probe. The data is fitted with an exponential decay (red line). The drift of 0.0015% per month is well within the design specification (From [66], mod.).

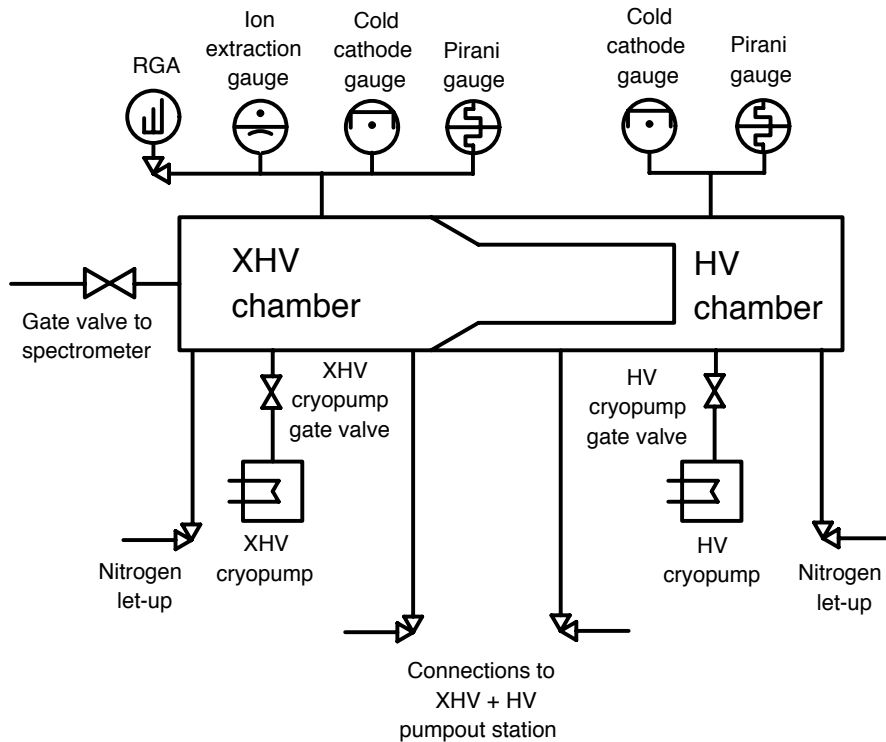


Figure 5.3.: **Draft of the FPD Vacuum System without the Pumpstation.** The main spectrometer is located on the left side (From [1]).

5.2.2. Vacuum System

The vacuum system of the FPD system consists of two separate chambers. On the one hand the Extreme High Vacuum (XHV) chamber at an operating pressure of 10^{-11} mbar is connected to the main spectrometer and houses the detector wafer. On the other hand, the High Vacuum (HV) chamber at a pressure of 10^{-6} mbar surrounds the XHV chamber and houses the detector readout electronics. The spacial separation of the detector wafer itself and the readout electronics is necessary to shield radiation from the electronics producing backgrounds in the detector wafer. The XHV chamber can be separated from the main spectrometer by a DN250 all metal gate valve, which will close automatically if the pressure in either the main spectrometer or the XHV chamber exceeds 10^{-8} mbar. To create and maintain a vacuum two different kinds of pumping systems are in use for both chambers individually. To initially pump down the chambers two turbopumps backed by dry scroll pumps are available and housed in a mobile pumping station. The pumping station can be connected to the HV and XHV chambers via bellows for an easy alignment. In the presence of magnetic fields the turbopumps may not be operated and the pumpstation is moved outside of the 30-mT area surrounding the detector. To maintain the vacuum during the magnets are operated two cryopumps, one for each chamber, are used. The cryopumps are connected to the vacuum chambers via bellows in order to reduce microphonic noise associated with their vibrating PTCs. In figure 5.3 a draft of the vacuum system is shown without the pumpstation. A series of pressure gauges including Extractor Ion Gauges, Cold Cathode Gauges, Pirani Gauges and Residual Gas Analyzers allow the monitoring of the pressures in the chambers [67]. At KIT a pressure of $3 \cdot 10^{-10}$ mbar in the XHV chamber was achieved. It is expected that the pressure will reach the design goal of 10^{-11} mbar once the FPD system has been adequately baked out and is operating at its optimum temperature after the installation of different upgrades to the system in summer 2012. The HV chamber reached the design goal of $1 \cdot 10^{-6}$ mbar.

5.2.3. Post-Acceleration Electrode

Since, in the KATRIN ROI around 18.6 keV, fluorescence peaks created in the materials close to the detector can appear in the spectrum a post-acceleration of the tritium endpoint electrons to higher energies can reduce the background during neutrino mass measurements. In addition, the probability for electrons being backscattered from the detector will be lowered, since their angle of incidence decreases with an increasing post-acceleration potential [56]. A post-acceleration can also be used to raise potentially interesting low-energy signals above the electronic noise threshold. To be able to raise the ROI of the tritium endpoint electrons coming from the main spectrometer to energies higher than 18.6 keV, a Post-Acceleration Electrode (PAE) is installed in the detector system. The PAE also forms the boundary between the XHV and HV chambers and will provide post-acceleration potentials up to 30 kV. Due to high magnetic fields in conjunction with the post-acceleration voltage there is a high probability for Penning discharges and electric breakdowns which occur in the region of the detector. To prevent this a cylindrical quartz tube with stainless steel foil electrodes on the inner and outer surfaces is installed between the PAE and the HV chamber wall. While the inner electrode is at post-acceleration potential, the outer electrode is at ground potential confining the electric field within the quartz insulator. With post-acceleration applied the detector wafer and the front-end readout electronics float at high voltage, which leads to constraints on the FPD systems design.

Although designed to be capable of 30 kV, the PAE has so far only been stable up to ~ 8 kV at KIT. At higher potentials, especially above 9 kV, high current spikes and discharges occur. During the disassembly of the FPD system in spring 2012, a possible reason for the discharges was found. In the high voltage rack, which floats on the post-acceleration voltage, a loose gasket stucked out barely touching the Faraday cage which surrounds the rack and sits on ground potential. With the lights in the hall off a clear discharge at ~ 14 kV is visible. In addition, the quartz insulator tubes in the HV chamber were found to be misaligned which might be the reason for discharges, as well.

While the pressure difference between the two vacuum chambers is only $\sim 10^{-6}$ mbar during normal operation, the PAE has to withstand a pressure difference of 1 atm when the HV chamber is vented for changes on the detector electronics. The original PAE became deformed by ~ 1 cm in the beam direction due to this high mechanical stress. A failure of the PAE would endanger the main spectrometer, therefore, to be able to connect the FPD system to the spectrometer a new mechanically more robust PAE was built in Seattle and shipped to KIT. It can handle the pressure difference of 1 atm in either direction and was installed in May 2012. In figure 5.4 a picture of the new PAE is shown prior to its installation.

5.2.4. Cooling System

To hold the detector readout electronics at a temperature below 50 °C during normal operation and the detector wafer below 0 °C to prevent high leakage currents an active cooling system is needed. Therefore, a PT60 PTC is installed between the magnets. Its cold head is connected to a copper ring around the ceramic break at the end of the PAE by a ~ 1 m long copper rod and a vibration-isolating copper braid since the PTC is not able to work in high magnetic fields. The detector itself is connected to the PAE by the so-called detector feedthrough-flange (see next section 5.2.5) at the downstream end of the PAE. Due to the quite long cooling chain the cold head of the PTC reaches temperatures below -135 °C, whereas the detector flange has temperatures of ~ -26 °C and the preamplifier modules ~ 40 °C. The advantage of this chain is the reduced outgassing rate of the PAE, since it is cooled to below -40 °C. All temperatures reached at KIT were found to be ~ 10 K higher than in Seattle. In addition, the temperature of the preamplifier modules at KIT



Figure 5.4.: Picture of the New, Mechanically more Robust Post-Acceleration Electrode.

Table 5.1.: **Heat Input by the Low Voltage Power Supplies into the FPD Vacuum System** for different configurations of detector quadrants powered. It is found that in each configuration where quadrant two is powered the heat input is higher than in a comparable configuration without quadrant two.

Quadrants no. Powered	Heat Input in W
-	3
0	3.9
1	3.9
2	4.1
3	4.0
0, 1	7.8
0, 2	8.6
0, 3	8.2
1, 2	8.5
1, 3	7.9
2, 3	8.9
0, 1, 2	12.4
0, 1, 3	11.8
0, 2, 3	12.5
1, 2, 3	12.4

is ~ 30 K higher during normal operation than it was in Seattle, while the temperature of the detector flange is nearly the same (except of the 10 K offset). Further, it is found that the heat input generated by the vacuum electronics is higher than expected. With all detector quadrants powered the heat input from the low voltage supplies into the FPD vacuum system at KIT was measured to be 17.4 W, while the low voltage power supplies were designed with an expected heat input of 15 W [68]. The heat input for different combinations of detector quadrants powered at KIT can be found in table 5.1. In each configuration where quadrant two is powered the heat input into the vacuum system is higher than in a comparable configuration without quadrant two. This might be due to an incorrect cabling of this quadrant inside the HV chamber which results in a few dead pixels in this quadrant as well. A further discussion on this can be found in the next section. The heat input into the system is expected to decrease when a new set of bench tested electronics is installed in summer 2012.

The new more robust PAE presents a greater heat load due to the increased conductance of the thicker walls. To compensate for this additional load the copper rod connecting the PTC to the PAE will be replaced by a more efficient heat pipe designed and constructed at the University of Washington [49].

5.2.5. Detector and Readout Electronics

The FPD consists of a 148-pixel PIN-diode array fabricated on a single silicon wafer [55]. The wafer has a thickness of 503 μm and a diameter of 125 mm including its guard and bias ring with a $<111>$ crystal orientation perpendicular to the surface. Its sensitive area has a diameter of 90 mm and fits completely within the flux tube defined by the Detector Magnet field. Electrons coming from the main spectrometer hit its unsegmented, shallowly ion-implanted, n++ ohmic face. The backside of the wafer is segmented into 148 pixels, all with the same area of 44 mm^2 , separated by 55 μm , yielding a pixel-to-pixel resistance of more than 1 G Ω . The pixels are ion-implanted, p-type and grouped



Figure 5.5.: Picture of the Detector Wafer's Segmented Backside. The 148 pixels arranged in twelve concentric rings plus four "bulls-eye" pixels are shown in addition to the guard and bias ring at the insensitive outer regimes of the wafer (From [1]).

in twelve concentric rings, each consisting of twelve pixels. In addition, there are four "bulls-eye" pixels in the middle of the wafer. The segmentation of the detector allows for measurement and correction of electromagnetic irregularities in the analyzing plane of the main spectrometer. On the pixel side of the wafer a non-oxidizing TiN coating facilitates electrical connections to allow the application of the bias voltage of 120 V. The TiN coating wraps around the edges of the wafer to the insensitive outer surface of the front of the wafer. In figure 5.5 a picture of the segmented backside of the wafer is shown and a description of the detection principle of PIN-diode detectors is given in chapter 4.2. To make electrical contact to the pixels, gold-plated pogo pins, obtained from Interconnect Devices, are pressed onto each pixel with a pin-compression of 0.38 mm. This results in a total wafer deformation of 0.24 mm, which has not been found to change the leakage current per pixel of 0.6 ± 0.1 nA at room temperature [54]. The XHV chamber, housing the detector wafer, and the HV chamber with the preamplifier modules are separated by the detector feedthrough-flange on which the pogo pins are mounted. This design provides a low capacitance and low microphonics connection between the detector wafer and the preamplifier modules. The feedthrough consists of a custom made, 184-pin array with gold-plated pins sealed in type-L21 borosilicate glass. The array consists of 148 pins for the detector signals, 12 guard-ring contacts and 24 bias-ring contacts. The pogo pins, which compress on the wafer, make contact to the feedthrough pins via Mill-Max brass-alloy adapter pins. In figure 5.6 a schematic view of the signal read-out from the wafer through the detector feedthrough-flange is shown. Detailed Geant4 simulations indicate that the borosilicate glass of the feedthrough generates the main background component of the detector due to the 0.06-Hz β -decay rate of potassium. The 3.6 T magnetic field then guides the electrons directly to the backside of the detector wafer. Cylindrical copper sleeves were designed and fabricated at the University of Washington, which fit over the feedthrough pins to prevent the β -electrons from the borosilicate glass reaching the detector

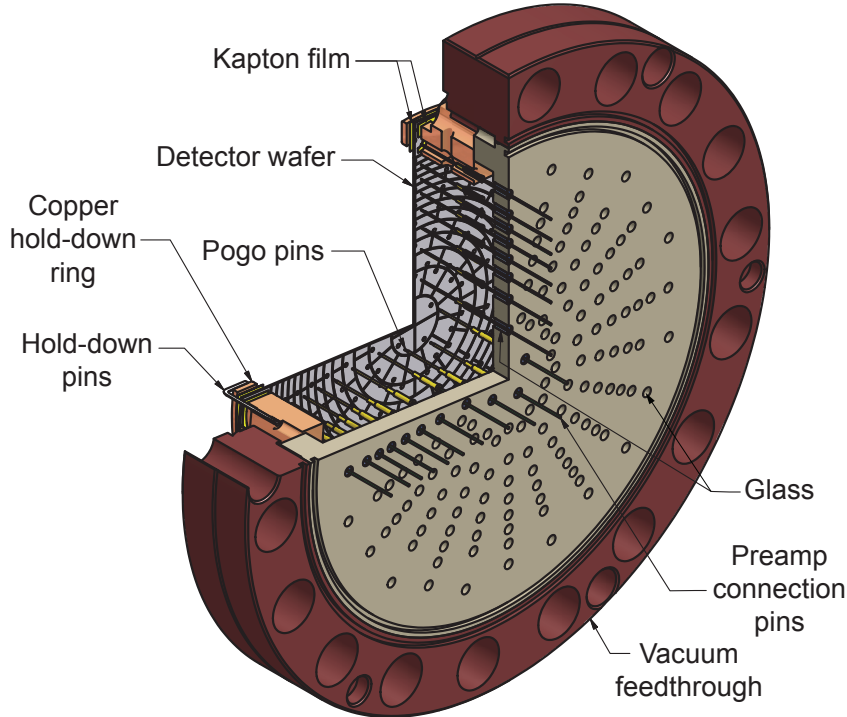


Figure 5.6.: Schematic View of the Signal Read-Out from the Wafer and through the Detector Feedthrough-Flange (From [1]).

wafer. After their installation in spring 2012, it is expected that they will reduce the detector background by at least one order of magnitude [49].

On the HV side of the detector flange the feedthrough pins make directly contact with the custom-made preamplifier modules. The 24 modules are arranged in a radial pattern with a 15° angular spacing between them. Each module consists of either six or seven charge-sensitive preamplifiers to amplify the signals coming from the pixels. The heat generated by the modules is conducted to the detector flange via mounting pins and from there to the PTC. To avoid a power dissipation only the first amplification stage is included on each module. In addition to the preamplifiers, the modules house electrical circuits to measure their temperature, the leakage current per pixel as well as a test pulse injection. On their rear end the modules make contact to a circular board, which distributes the output signals to a cable harness. Another ring shaped board sitting under the circular board redistributes the power and control lines to the cable harness. In figure 5.7 a picture of the vacuum electronics, described above, is shown. At its downstream end the cable harness connects to six, 50-pin, sub-D feedthroughs in a custom made feedthrough-flange which connects the HV chamber to ambient air. On the other side of the flange four 37-channel signal boards as well as a power-and-control (PAC) board make contact to the feedthroughs. The PAC board provides power-conditioning circuits, over-voltage protection as well as variable-gain controls and temperature read-outs. Besides a differential pick-up and additional signal amplification, the signal boards allocate variable-gain stages and fiber-optic transmitters. These transmitters are needed to convert the analog pixel data into optical signals, which are sent to the DAQ system via optical fibers. Since the detector electronics described up to this point float at the post-acceleration potential, this optical connection is needed to feed the signals out of the high voltage area. The signal- and PAC-boards are installed in an anti-corona housing inside a Faraday cage and use power supplies sitting in a high voltage rack which floats at post-acceleration voltage, as well. The high voltage rack as well as the DAQ rack are located 2.5 meters further downstream placing them outside

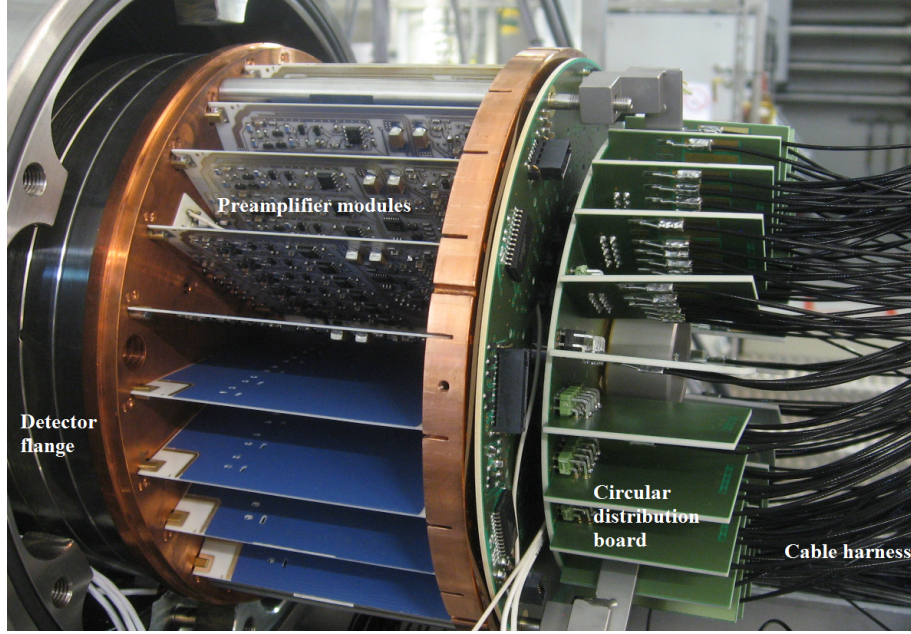


Figure 5.7.: **Picture of the Vacuum Electronics** including the feedthrough-flange, the preamplifier modules, the circular boards and the cable harness (From [1], mod.).

the 7-mT magnetic-field contour. The power lines from the high voltage rack to the PAC board are fed through an insulated metal tube connecting the high voltage rack with the Faraday cage.

In the cable harness installed in the vacuum system some channels of detector quadrant two were wired incorrectly at KIT for the measuring period relevant to this thesis. This results in 13 dead channels and 4 additional channels with high noise or crosstalk in quadrant two. In the other three detector quadrants only 7 channels show a high noise level or crosstalk. Over all this results in 135 (91%) working detector channels, where 11 channels have a high noise level or show crosstalk. The number of working channels, stated above, is obtained by a direct test-pulse injection into the preamplifier modules. The number of working pixels differs from the number of working channels and is obtained by ^{241}Am measurements described in chapter 6. After the installation of a new set of electronics in summer 2012, the number of working channels is expected to increase.

5.2.6. Data Acquisition System and Slow Controls

To digitize and process the data coming from the FPD and the veto a Data Acquisition System (DAQ) was developed which consist of two parts: The DAQ electronics and the DAQ software. All devices which are not part of the detector or veto signal chain are monitored and controlled via Slow Controls.

1. DAQ Electronics:

The FPD DAQ electronics follow the same concept used by the Pierre Auger Cosmic Ray Observatory [69]. While the analog part of the electronics is KATRIN specific, the digital part is more general and user-programmable. To allow a time synchronization with other DAQ systems in KATRIN, the DAQ electronics are able to accept timing signals from a global-positioning-system clock. The optical detector signals coming from the ambient air signal boards are fed into eight First Level Trigger (FLT) cards which sit in the DAQ rack each handling 24 channels. Besides the optical-to-analog conversion, they condition and process the analog signals as well as

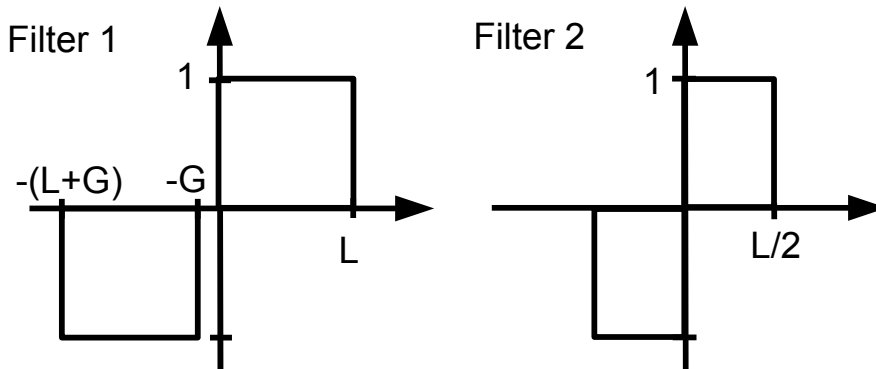


Figure 5.8.: Response for the Two Trapezoidal Trigger Stages of the FPD DAQ System as a function of time (in ADC bins). L is the filter length needed to smooth the signal and G the gap length of the trigger. It ensures that the rise time of the pulse is not used for the determination of the signals height (From [1]).

digitize the signals using series Analog Digital Converters (ADCs) with 12-bit precision and 20-MHz sampling rate. The acquisition and preprocessing is controlled by Altera Cyclone II EP2C35 Field Programmable Gate Arrays (FPGAs) and a central FPGA does the time synchronization and the read-out for each card. In addition, two FLT cards handle the processing of the analog veto signals. The FLT cards are followed by a Second Level Trigger (SLT) card using an embedded 1.4-GHz Pentium M processor running Linux to initialize and coordinate all ten FLT cards.

The digital part of the DAQ electronics uses a 64 pages ring buffer to record the ADC traces, which allows operation at rates up to 70 kHz without any dead time. Since the rates at the detector differ over a few orders of magnitude between calibration runs and actual neutrino mass measurements, the experimenter can choose between three different recording modes. While the 'Energy Mode' is the usual operating mode recording the energy and timing of each event the 'Trace Mode' adds a 2048 points waveform for each event to the recorded data. In the case of high rates the 'Histogram Mode' is used, which records a 2048-bin energy histogram for each channel.

An electron incident on the detector results in a step in the signal fed into the DAQ electronics with the height being proportional to the incident energy. Two trapezoidal filters, schematically shown in figure 5.8, detect this step and determine its height which is subsequently compared to a programmable energy threshold. To search for coincidences in the veto signals a special Veto Mode can be used. Since cosmic muons hitting the veto panels create relatively short signal pulses, only the second trapezoidal filter is used in this mode, recording the pulse height and an event time stamp. To differentiate between actual muon events and noise the experimenter can define how many coincidences the FPGA should look for in the fiber signals from one veto panel. A read-out is only triggered, if the sum of the signals from all fibers of the panel will exceed a threshold at the same time as the coincidence takes place [70], [1].

2. DAQ Software:

The DAQ software of the KATRIN experiment is based on a Object-oriented Real-time Control and Acquisition package (ORCA), which was developed at the University of Washington and the University of North Carolina [71]. It is written in Objective-C for the Mac-OS X operating system and allows the control and moni-

toring of measurements with the FPD system as well as the veto system. A graphical user interface consisting of drag-and-drop items representing the hardware components can be edited by the user. In addition, ORCA provides the access to the FLT and SLT cards to control the data read-out. Before starting a measurement via ORCA, the user is able to set variable conditions for the measurement by writing a script in ORCAScript. After changes of the configurations, no compilation of ORCA is needed. The results of each measurement can be written into ".root" files via ORCAROOT for a further analysis with CERN's ROOT package [72].

3. Slow Controls:

To control all devices which are not in the FPD or veto signal chain a software program called Slow Controls (SC) is used. It provides a user interface to make quick status checks and to define set points for the different devices. The communication of SC with the devices is done via a compact Field Point (cFP) hardware from National Instruments. The overall management is provided by the ZEntrale datenerfassung Und Steuerung (Central DAQ and Control System, or ZEUS) software [73]. In case of an emergency, e.g. a sensor value exceeds its set point value, the local cFP initializes an emergency shutdown of the affected system and sends out alarm messages via email or text message. In addition, it will generate an alarm in the KATRIN hall itself. For safety reasons the magnet status can only be monitored but not remotely controlled via SC.

5.2.7. Calibration Sources

To do calibration measurements with the detector system in a standalone mode a number of calibration sources is installed. All sources can be moved in and out of the system without breaking the vacuum. In figure 5.9 a schematic view of the sources is shown.

- **^{241}Am γ -Source:**

To measure the detector response to mono-energetic γ -photons an ^{241}Am -source is installed at the XHV chamber between the magnets and can be moved in and out of the system via an air-driven motor. It was built at the Massachusetts Institute of Technology in Boston and has an activity of 18.5 MBq. Due to shipping problems, it has not been available at KIT yet and various other high activity sources available at KIT do not have the right dimensions. Thus, all measurements were done with a weaker source (<3.7 MBq), available at KIT, which fits into the source holder of the FPD system [74].

- **Titanium Disc with UV Illumination:**

A titanium disc with a diameter of 20 cm is installed between the magnets on top of the XHV chamber and is inserted into the flux tube by an air-driven motor. The disc can be raised to potentials of up to 30 kV and when illuminated with UV light it generates mono-energetic photo-electrons used to measure the detector response. The 240-nm UV light is provided by an UV-LED mounted inside an optic assembly which can be installed outside of the vacuum system at a quartz window. To project the UV light as uniformly as is reasonably possible onto the titanium disc the optic assembly consists of three parts: A collimation assembly, a prism assembly and a focusing assembly [75]. Due to space restrictions in the area where the optics assembly is located and a small opening angle of the UV LED of 2.5 °, it is not possible to illuminate the titanium disc uniformly. After calibration data had been taken at KIT, a loose electrical connection to the UV LED was found which resulted in lower detector rates during the calibration measurements. As discussed in chapter 6 these rate issues significantly affect the measurements. In figure 5.10 the rates on the detector at a disc voltage of 18.6 kV are shown. At KIT the electron disc suffered

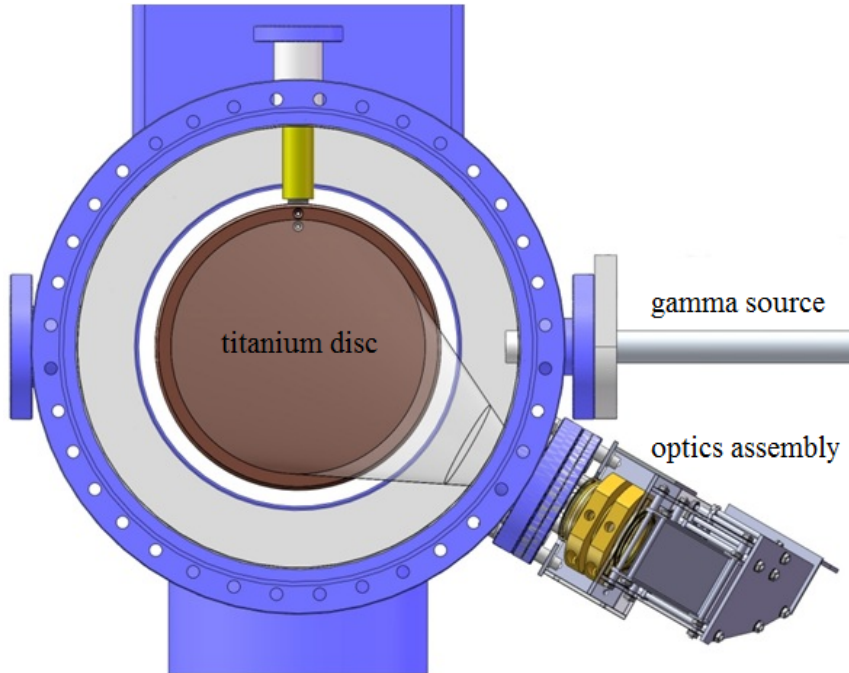


Figure 5.9.: **A Schematic View of the FPD's Calibration Sources** is shown without the direct pulser and the test-pulse injection. On the right side, the holding structure of the ^{241}Am -source is shown retracted out of the XHV chamber without breaking the vacuum. The titanium disc is inserted into the flux tube and illuminated by the optics assembly shown in the lower right corner (From [1], mod.).

from discharges at voltages of 25 kV after \sim 45 minutes but was stable at 20 kV for periods of more than 1 day. On top of the titanium disc support structure a Precision Ultra-Low Current Integrating Normalization Electrometer for Low-Level Analysis (PULCINELLA) is installed to measure the effective charge of the photo-electrons emitted from the disc [76]. By comparing the photo-electron current from the disc to the electron rates measured by the detector one can make efficiency measurements of the detector. Due to the inhomogeneity of the illumination through the UV light at KIT, these measurements have not been carried out yet.

- **Red LED:**

In addition to the UV-LED, a red LED is installed inside the optics assembly. Its light floods the vacuum chamber, scatters on its walls and when hitting the detector wafer produces ion pairs in the silicon. These ions create a signal in the detector which is proportional to the intensity of the light. The voltage applied to the LED is likewise proportional to the intensity and can be measured with an oscilloscope. In a pulsed mode the LED is used for linearity measurements of the detector electronics [77].

- **Direct Pulser and Test-Pulse Injection:**

An electric pulse can be either fed directly into the FLT cards (Direct Pulser) to test the DAQ system or into the preamplifier modules (test-pulse injection) to check the behavior of the read-out electronics. The Direct Pulser is for example used to determine the timing resolution of the FPD electronics and is programmed to have the shape of a pin-diode signal. The test-pulse injection is used to determine the FPD channel map.

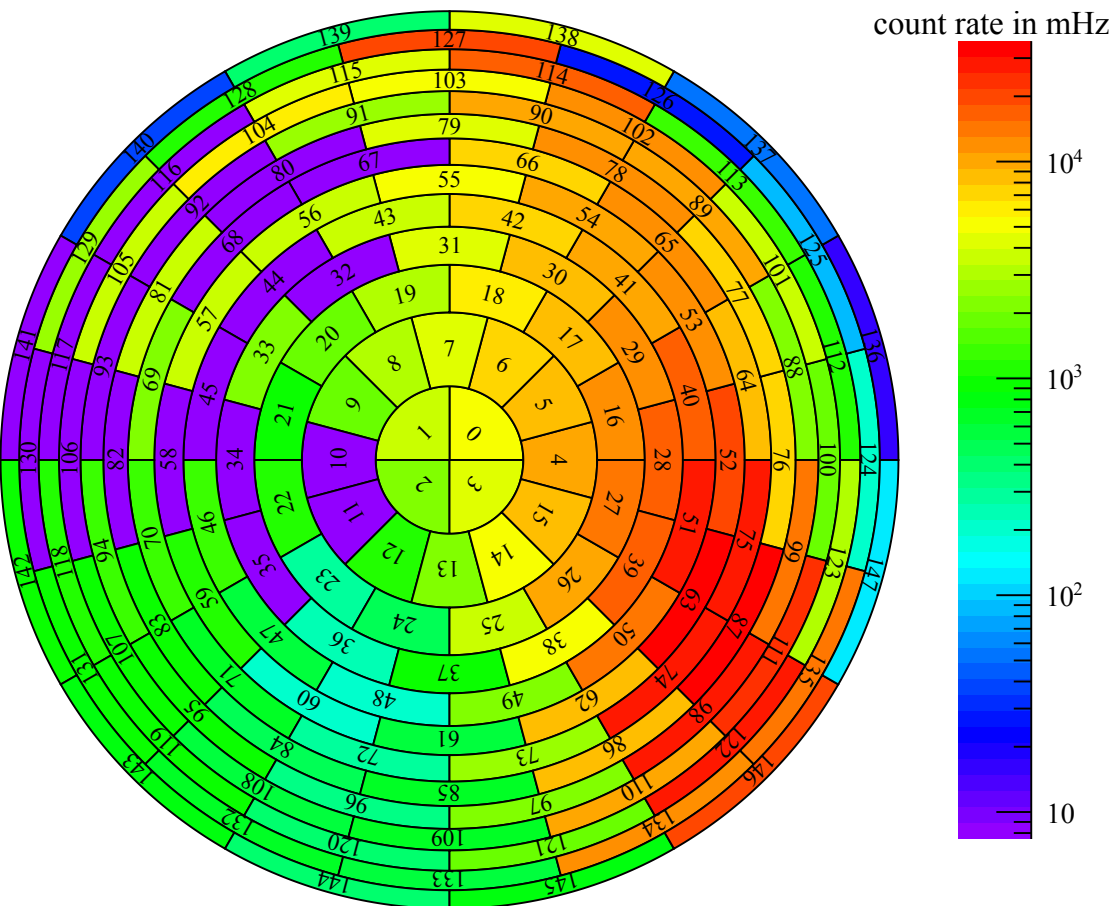


Figure 5.10.: Spacial Pattern of the Detector Rates with the Electron Disc at 18.6 keV and Illuminated with UV Light. The non-uniformity of the rates is a result of the UV LED not uniformly illuminating the titanium disc. All pixels in purple are not working and therefore disabled.

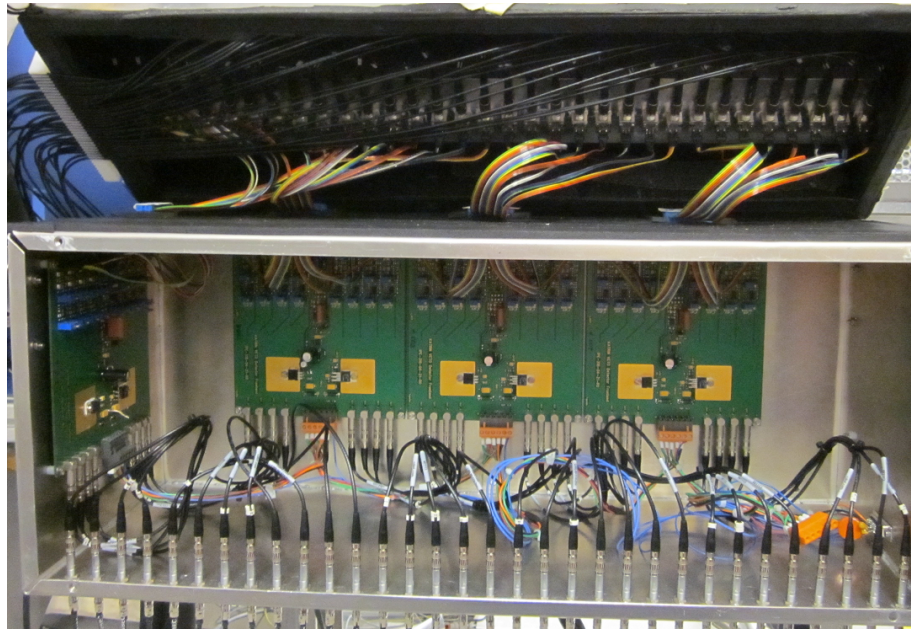


Figure 5.11.: **Picture of the Veto Readout Electronics Box** with the upper part lifted up to show the aluminum bar that supports the MPPCs which in this picture are connected to the veto panels by optical fibers. The four amplifier boards are located in the lower part of the box.

5.2.8. Veto System

Besides a passive low activity lead and copper shield the detector is surrounded by an active muon veto system consisting of St. Gobain Bicron-408 plastic scintillator panels. It is mounted around the vacuum system inside the Detector Magnet's warm bore and the scintillation light is extracted via optical fibers. The veto consists of 4 long panels and two half moon end caps resulting in a total of 32 readout fibers. The fibers connect to Multi Pixel Photon Counters (MPPCs) made by Hamamatsu Photonics. The MPPCs can operate in high magnetic fields and detect the light coming from the panels to produce a charge signal, which is fed into custom-made amplifier boards. A more detailed discussion on the properties of MPPCs is given in chapter 4.2.2. Each amplifier board accommodates 8 channels and its output signals are sent via lemo cables to the DAQ crate. In figure 5.11 a picture of the veto readout electronics box is shown which houses the MPPCs and the amplifier boards. All MPPCs sit on an aluminum bar which is cooled by two Peltier Coolers on top of the box to reduce the dark rates of the MPPCs. On their warm side, the Peltier Coolers have additional water cooling blocks which are fed with a mixture of distilled water and ethanol maintained at a temperature of 6 °C by a chiller. During normal operation the MPPCs are cooled below -16 °C where the dark rates drop to ~4.7 kHz/channel [1]. To prevent water condensing on the MPPCs the upper part of the veto box, which houses the MPPCs, sits under a nitrogen atmosphere regulated via a flowmeter. Due to a high use of nitrogen and oscillations caused by the instable electric connection of the MPPCs to the amplifier boards the connections were rebuilt in this thesis and sub-D feedthroughs were installed between the upper and the lower part of the box. In figure 5.12 a picture of the new feedthroughs with an added ground connection for each MPPC is shown. Since this change no more oscillations are seen in the veto data.

The amplifier boards are powered with +6 V and -6 V power supplies, whereas the MPPCs bias comes from a 120 V power supply and is set via regulators on the amplifier boards between 60 V and 80 V depending on the performance of the individual channel. In



Figure 5.12.: **Picture of the New Signal Feedthrough for the Veto** in the lower part of the veto box. A ground connection for each MPPC was added replacing a single ground connection to the aluminum bar which houses the MPPCs.

addition, a clipping voltage on the signals can be set by hand with regulators on the amplifier boards for each channel to shift the baseline of the veto signals before being fed into the DAQ. The possibility of clipping was added to maximize the deconvolution of the first photoelectron peak and noise from the electronics, which looks like the first photon peak, before digitizing the signals. At KIT, measurements for the MPPCs dark rates were done with 31 (96.9%) of the MPPCs working and a representative dark rate spectrum of MPPC #8 can be seen in figure 4.4 in chapter 4.2.2.

Due to a failure of the Peltier water cooling system, it was redesigned and rebuilt during this thesis to allow stable operating temperatures of the MPPCs. This is of great importance to keep the MPPC dark rates small. In figure 5.13 the power outputs of Peltier Cooler B are shown before and after the installation of the new water cooling system. An increase of the power output with time with the old cooling system resulted in a non-stability of the MPPC temperatures. With the new system the power output is stable and in addition, lower operating temperatures for the MPPCs are possible. The results of a longtime stability measurement for the first photoelectron peaks of the dark rates are shown in figure 5.14. \sim 175 hours after the initial cooldown the temperatures of the MPPCs are in equilibrium and the peak positions stop to drift. Therefore, it can be stated that the veto system operates stable now and further data with the system can be taken in summer 2012, including efficiency measurements and coincidences between different panels.

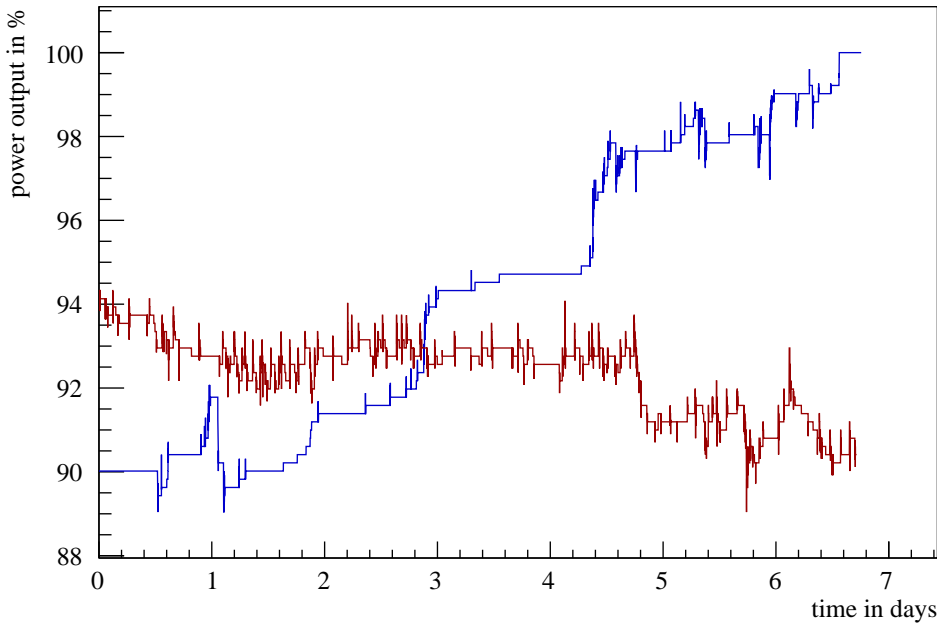


Figure 5.13.: **Power Outputs of Peltier Cooler B** before (blue line) and after (red line) the installation of the new water cooling system. The increase of the power outputs with the old water cooling system with time results in a non-stability of the MPPC temperatures. With the new system the outputs do not increase. Note that the Peltier Coolers temperature set point was at -17 °C in the old configuration and is at -18 °C in the new one.

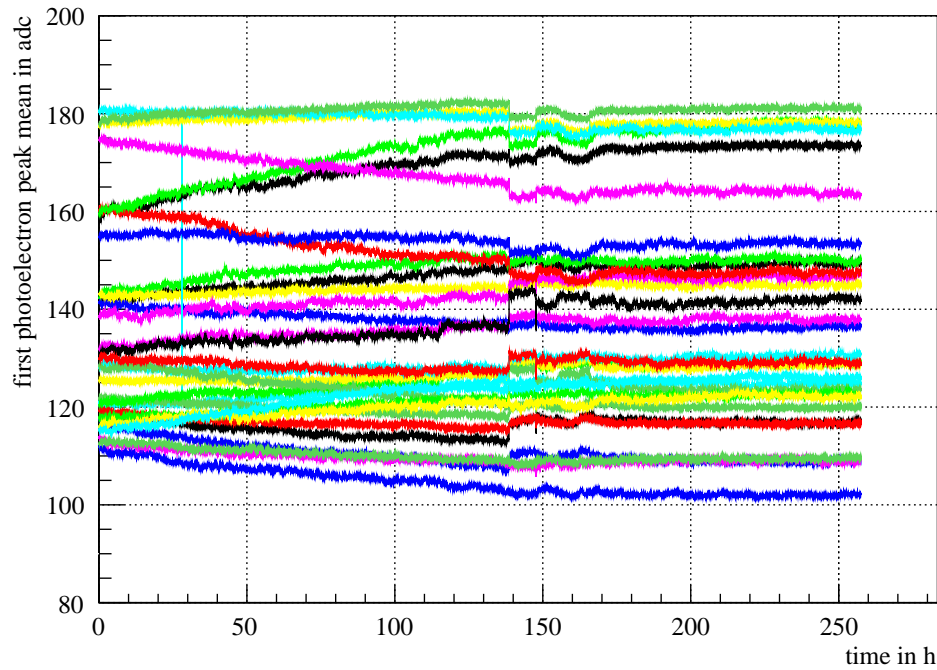


Figure 5.14.: **Stability of the First Photoelectron Peak Positions with Time** for 31 MPPCs. The steps between hour 140 and 150 correspond to a failure of the nitrogen supply for the veto box. Note that the peak positions reach an equilibrium \sim 175 hours after the initial cooldown.

6. First Measurements and Results

From January to March 2012 data was taken with the FPD system mostly at nominal magnetic fields of 6 T (Pinch Magnet) and 3.6 T (Detector Magnet). In the following first results are presented and discussed. To enable an easy comparison with the data taken in Seattle in 2011, the conditions for the measurements at KIT were held as close as possible. Information on the Seattle measurements can be found in [1]. The analysis was carried out using CERN's ROOT package, version 5.32/01 [72]. Due to inhomogeneities in the illumination of the detector wafer by some of the calibration sources, the number of pixels used for the data analysis depends strongly upon which source was used. In section 6.1 the linearity of the FPD electronics is investigated and in section 6.2 the energy resolution of the detector response to monoenergetic γ -photons and electrons is determined. In this context the energy calibration of the detector with the use of an ^{241}Am -source is described. This calibration forms the basis for essentially all other measurements. In section 6.3 a strong background effect, which was found during data taking with the electron disc at high voltage, is discussed. This is relevant for the determination of the detector wafer's dead layer described in section 6.4, in particular.

6.1. Linearity

To make an estimate on the linearity of the FPD electronics a pulsed standard miniature instrument red LED is used to flood the XHV chamber with photons. These photons will scatter at the chamber walls, hit the detector wafer and create electron-hole pairs in the wafer resulting in a detector signal. The number of electron-hole pairs created and therefore, the detector response scales linearly with the intensity of the incident light. To produce a signal equivalent to the 59.54-keV ^{241}Am γ -line a steady-state current of 0.5 nA through the detector wafer is needed with a fixed pulse width of 5 μs at 100 Hz, which is reasonable for a PIN diode illuminated by a pulsed LED. The direct use of an electronic pulser, e.g. with its pulse fed into the preamplifier boards is not possible for the linearity measurements, since the pulser's signal would have to be transmitted optically across the post-acceleration potential and the optical transmitters would distort the signal [77].

The detector response on the red light was measured by driving the LED using different voltage settings of a 33220A Agilent pulser. To stabilize the operation of the LED a Hamamatsu S4204 silicon PIN diode is built into the illumination device, which houses the red LED in such a way that it can measure a fraction of the light coming from the LED. The diode's photocurrent is used in a feedback arrangement for the LED drive

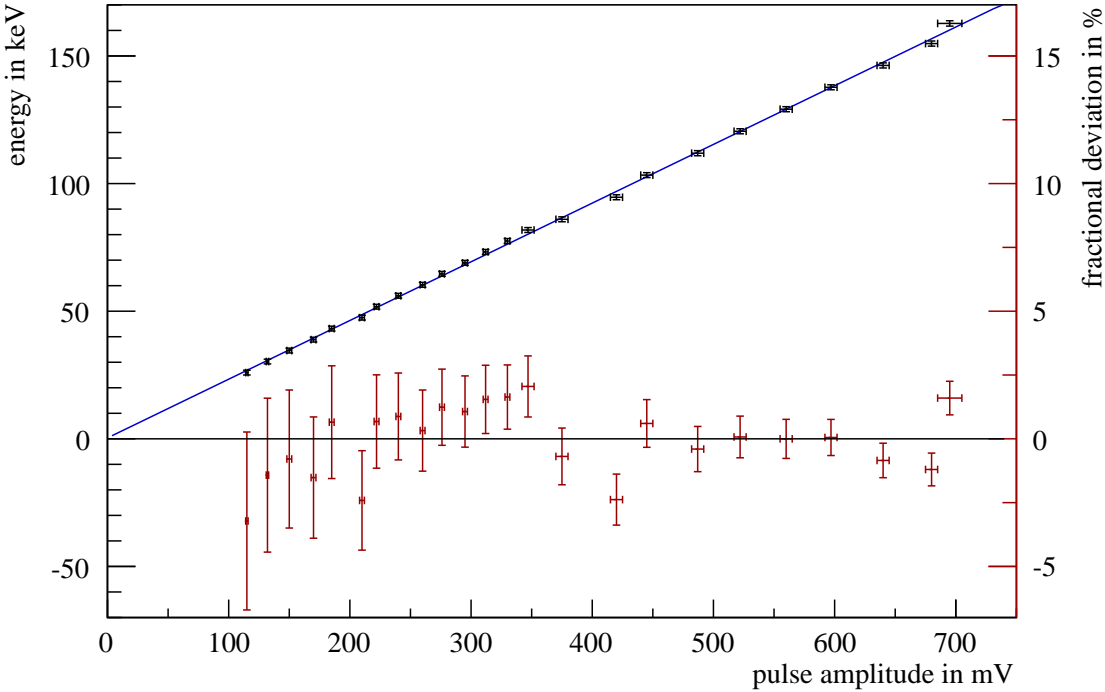


Figure 6.1.: **The Linearity of the FPD Electronics** for pixel 54 is determined by the use of a pulsed red LED which shines onto the detector wafer. The black data points with statistical error bars represent the dependence of the detector response (left axis) on the pulser voltage measured with an oscilloscope. In blue the best linear fit through the data points is given. In addition, the resulting fractional deviation from linearity (right axis) is shown in red with statistical error bars.

ensuring a precise scaling of the LED's light intensity with the applied voltage from the pulser. While stabilizing the LED in this way, the LED voltages were measured using a UTD2052CEL oscilloscope with a 50-MHz sampling rate. The voltage set points for the pulser, as well as the measured voltages can be found in table A.1 in the appendix. The resulting energy spectra show a clear peak, which was fitted for each pixel individually by a Gaussian function to obtain its mean. In figure 6.1 the derived means in keV (for the energy calibration of the detector see section 6.2) over the measured voltages at the LED are shown for the randomly chosen pixel 54 with statistical error bars. The uncertainty in the value of the voltage is obtained from the uncertainty of the used oscilloscope. The uncertainty on the mean of the detector response peak is the standard deviation of the Gaussian fit. An estimate of the linearity of the system is obtained by making a linear fit of the data points. The fractional deviation from the fit is also shown in figure 6.1. The pulser uses an auto-range mode where internal switches introduce attenuators at programmed points during a voltage change. The imperfect precision of the attenuators can introduce steps in the linearity curve as can be seen in the fractional deviation from linearity. The plot in figure 6.1 is representative for all 125 pixels used for the analysis were 23 pixels are excluded, due to a distortion of the peak. The results of the linear fits for all pixels in terms of the slope and the offset are shown in figure 6.2. It is reasonable that there is a variation of the slope and the offset of the linearity from pixel to pixel, due to the different behavior of each readout channel but the effect is negligible for the further analysis. In addition, it can be stated that the FPD readout electronics show a linear behavior with less than $\sim 5\%$ fractional deviation from linearity (apart from the

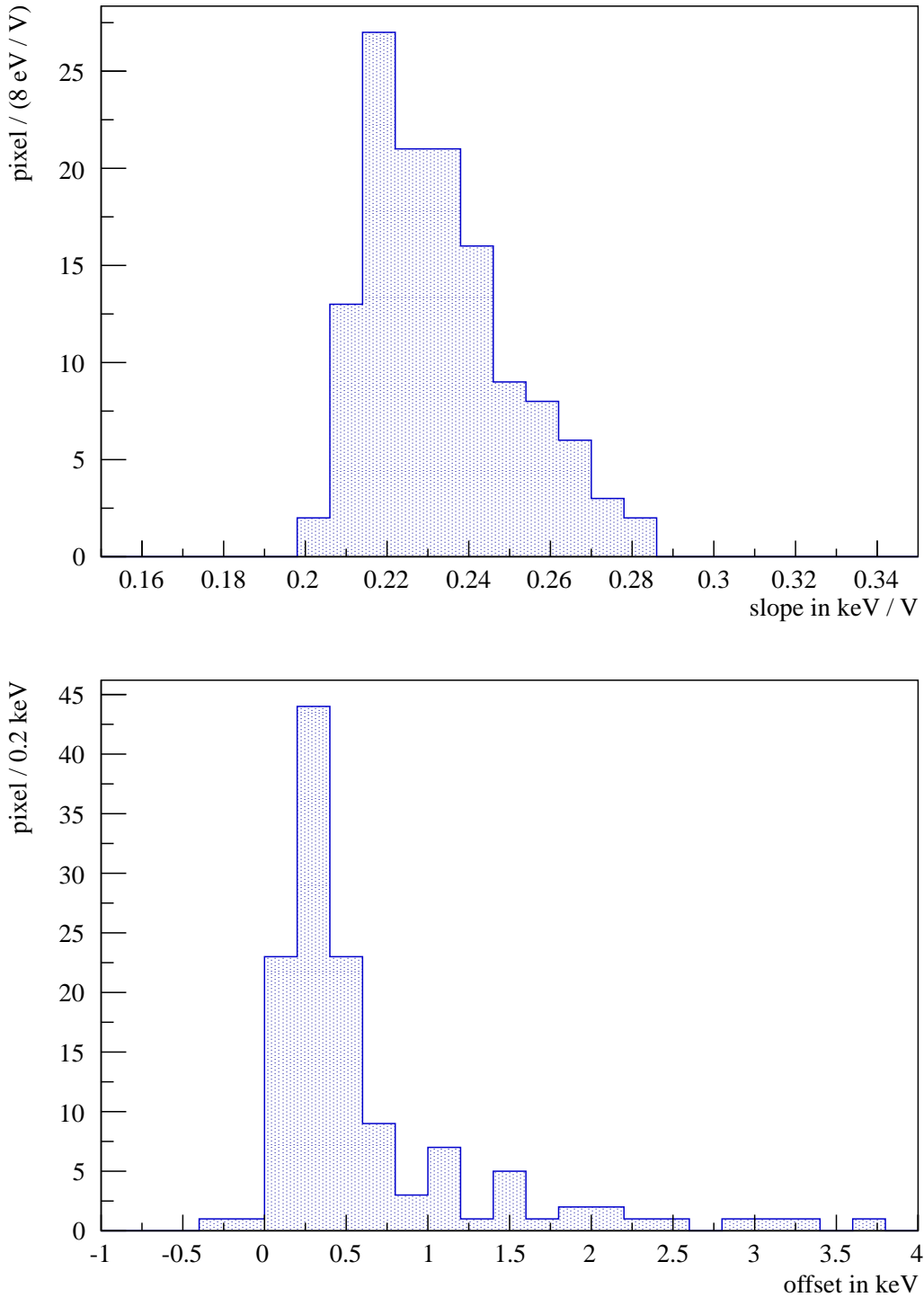


Figure 6.2.: **Distribution of the Linearity Slopes and Offsets for 125 Pixels.** An analysis such as is shown in figure 6.1 was done for 125 pixels of the detector.
Top: The distribution of slopes of the FPD electronic's linearity fit.
Bottom: The distribution of offsets of the FPD electronic's linearity fit.

first value) for all pixels and in all measurements. It should be noted that the fractional deviation from linearity in Seattle was less than at KIT. This is due to a different approach for the measurement in the Seattle analysis (see [1]) where the setpoint of the pulser was used for the linearity fit instead of the measured value of the voltage at the LED stabilized by the feedback arrangement. In addition, the statistical uncertainties on the detector response are higher at KIT, since the standard deviation is used for the error bars instead of the fit uncertainties.

6.2. Energy Resolution

To calibrate the detector and determine its energy resolution an ^{241}Am -source is used to measure the detector response to monoenergetic γ -photons. In the spectrum of ^{241}Am significant γ -peaks appear at 26.35 keV and 59.54-keV besides a number of low-energy X-ray peaks [78]. In section 6.2.1 an overview of the detector's energy calibration by a fit of the 59.54 keV line in the ^{241}Am -spectrum is given. Changes of the detector's energy calibration with time as well as discussions about the appearance of Compton spectra in the data are presented, too. The results concerning the energy resolution obtained with the UV-light illuminated electron disc at high voltage are presented in section 6.2.2.

6.2.1. ^{241}Am -Source

The 59.54-keV γ -peak in the ^{241}Am spectrum is separated from other peaks in the spectrum by more than 30 keV. Therefore, quality fits to this peak are straight forward making this peak the ideal candidate for an energy calibration of the detector. In the following, the energy calibration for each pixel of the detector can be understood as the ADC-to-energy conversion obtained from a fit of the 59.54-keV peak in the pixel response spectrum to monoenergetic γ -photons from the ^{241}Am -source. The ADC-to-energy conversion for each pixel is done, according to:

$$E = C \cdot \text{ADC} + \text{Offset} \quad \text{with} \quad C = \frac{59,540 \text{ eV}}{\text{mean of the fit (in ADC channels)}} \quad (6.1)$$

The offset in the energy calibration was found by a fit of the second γ -peak at 26.35 keV in the spectrum to be in the 0.1 keV regime. The factor C is used in all other measurements for the energy calibration with the offset ignored or considered as part of a systematic uncertainty in case of the dead-layer determination. A number of calibration measurements were taken during the measurement period, but due to the low activity of the source available at KIT at the moment only a few sequential data sets were taken with sufficient statistics for the energy calibration of the detector. In the following, the data from a set of 16 sequential runs, 4 hours each, without magnetic fields is used and the combined spectrum for 129 pixels can be found in figure 6.3 with a fit of the 59.54-keV peak to the data. 14 pixels showed no response to the ^{241}Am -source. For another five pixels the background noise is so high as to make a fit of the 59.54-keV peak impossible. These pixels are excluded from the spectrum shown in figure 6.3, while one pixel with a high energy resolution of more than 3 keV (FWHM) is still included. The summed pixel energy resolution gives a detector response to γ -photons of $\Delta E = 1.637 \pm 0.004$ keV (FWHM) at 59.54 keV. This is higher than the resolution that was obtained in Seattle ($\Delta E = 1.51 \pm 0.03$ keV (FWHM)), which might be due to the new set of electronics which was installed at KIT and performs somehow different (e.g. is running at higher temperatures). Note that an energy resolution of $\Delta E \leq 1$ keV (FWHM) is aimed for the detector but not necessary (see chapter 5.1). The energy resolution and the ADC-to-energy conversion factors of the individual pixels can be found in table A.2 in the appendix. For all measurements described in this chapter this energy calibration is used in the analysis for each pixel if not stated otherwise.

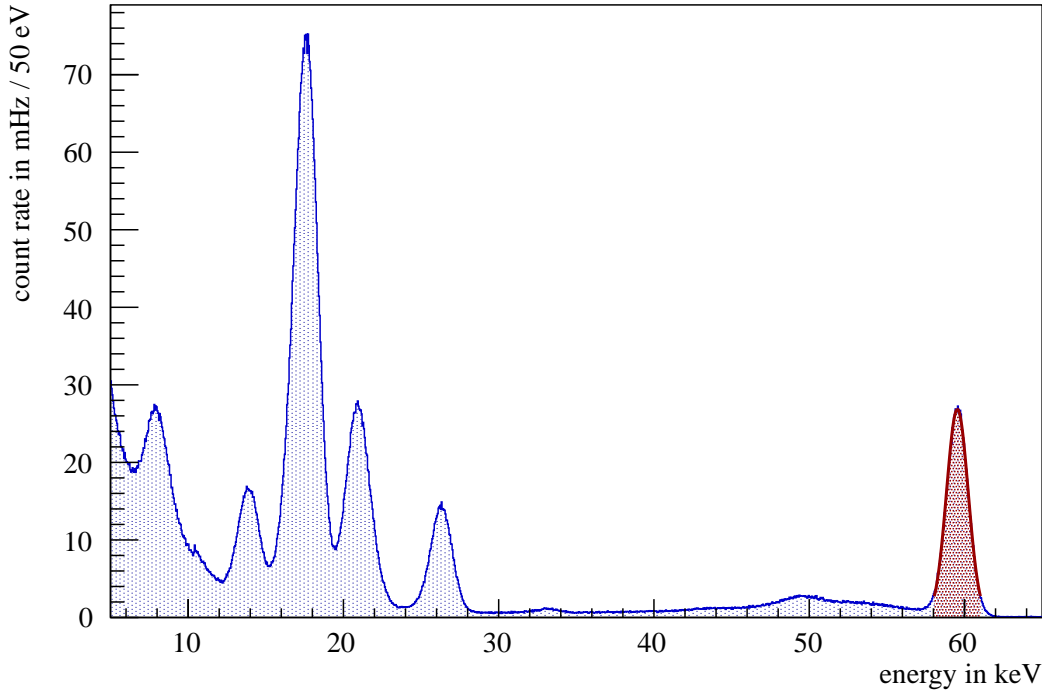


Figure 6.3.: **^{241}Am Spectrum with a Gaussian Fit of the 59.54-keV Peak for 129 Pixels.** The data was taken with no magnetic fields applied and the fit (red) gives a global energy resolution of $\Delta E = 1.637 \pm 0.004$ keV (FWHM).

In another calibration measurement with the magnets at nominal fields (6 T and 3.6 T) the ^{241}Am -spectrum of a few pixels showed evidence of a Compton spectrum with the edge at ~ 56 keV resulting in higher rates for these pixels. The event rates on the detector with the γ -source retracted by ~ 7 cm are shown in figure 6.4. It appears that only pixels in the magnetic shadow of the γ -source holder are affected by the Compton spectra leading to the assumption that the γ -photons from the source knock out electrons from the source-holder's material by Compton scattering which are subsequently guided towards the detector by the magnetic field lines. Since the Compton edge is close to the 59.54-keV γ -peak, the usual energy calibration for the affected pixels is not possible. In order to be able to carry out an energy calibration with the magnets at nominal fields two calibration measurements are needed, one with the γ -source completely inserted into the XHV chamber and one with a retraction of the source by ~ 5 to 7 cm. In this case an acceptable energy calibration measurement is done at least once for each pixel. To do this in a reasonable timescale a γ -source with a higher activity is needed.

A comparison between the fit results from different energy calibration measurements (some with low statistics) provides a measure of the scattering of the derived ADC-to-energy conversion factors per pixel. Even if a small scattering of the factors is reasonable and acceptable for the detector, some of the pixels show a scattering of more than 6 keV/ADC-channel between different measurements. This affects among other things the dead layer determination in section 6.4 and will be discussed further in this context.

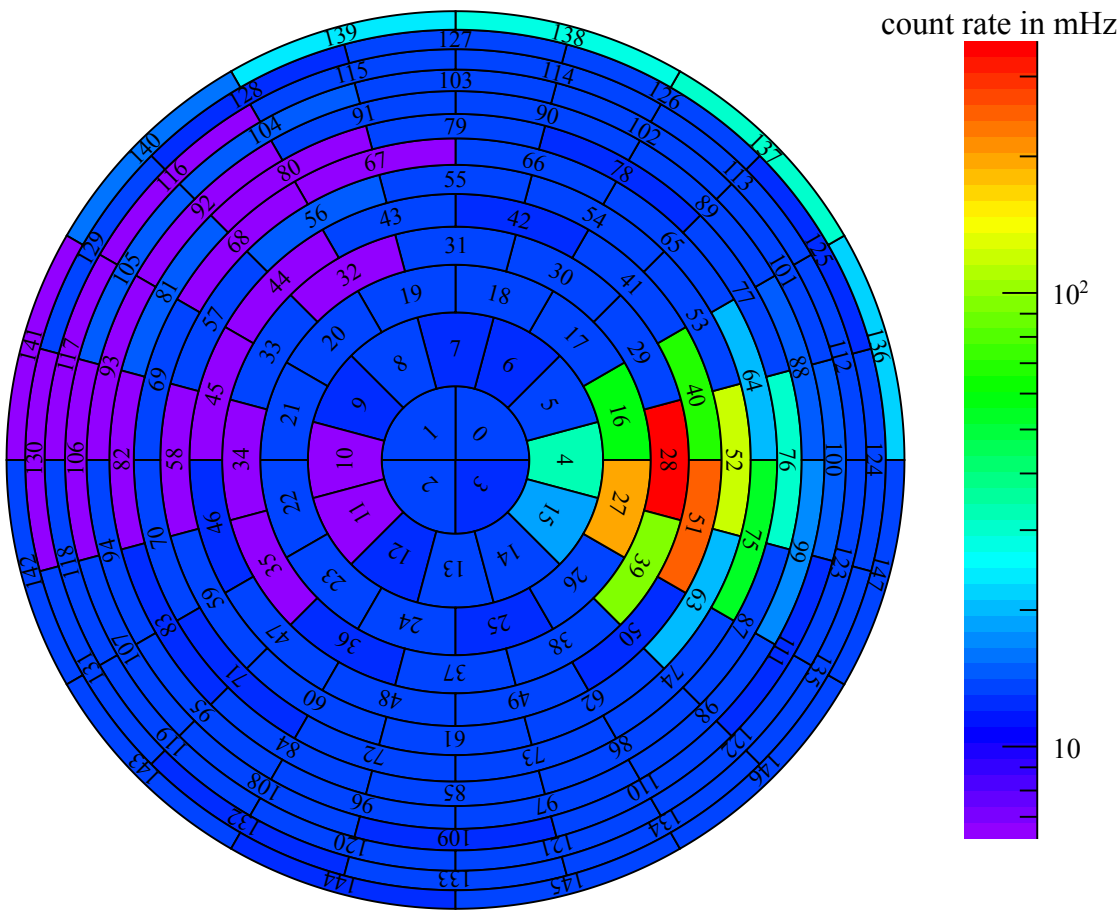


Figure 6.4.: **Compton Scattering in the ^{241}Am Source Holder.** At nominal fields (6 T and 3.6 T) a rate increase in the magnetic shadow of the ^{241}Am -source holder occurs on the detector. In this case the source was retracted by ~ 7 cm from its fully inserted position.

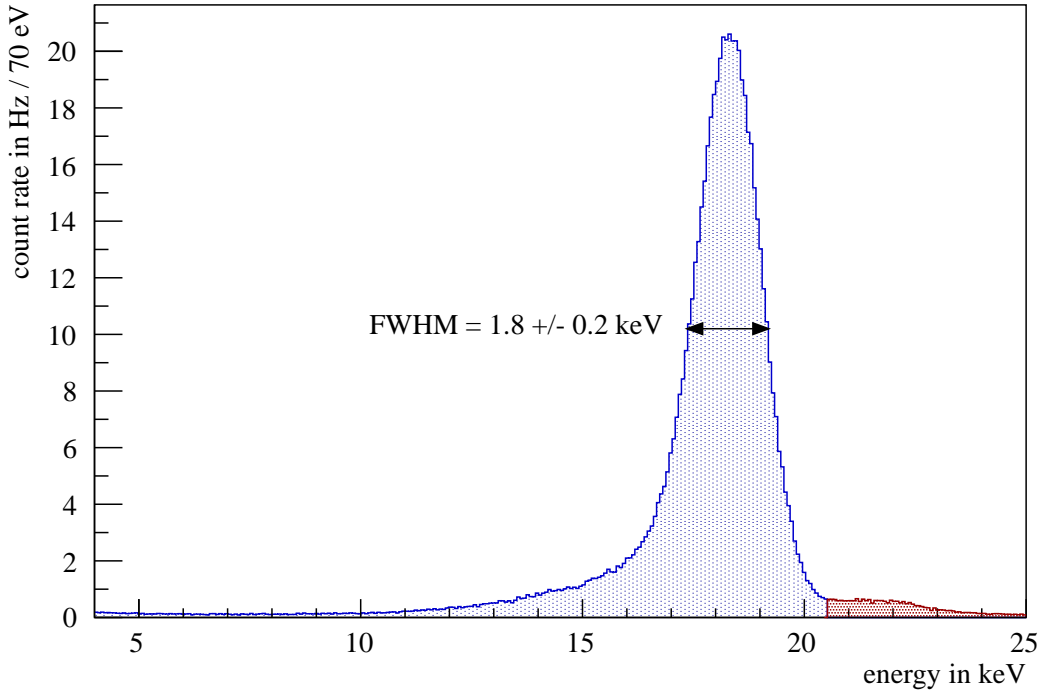


Figure 6.5.: **Global Spectrum of 18.6-keV Electrons** generated by the illumination of the electron disc ($U_0 = -18.6$ kV) with 240 nm UV light. The spectra of 63 pixels that received sufficient illumination are combined. At the high-energy side of the peak a little bump appears (red) which corresponds to a yet unknown background effect.

6.2.2. Electron Disc

To determine the energy resolution of the detector response to monoenergetic electrons a series of measurements was performed with different voltages applied to the inserted electron disc (see table A.4 in the appendix). The UV LED used for the illumination of the electron disc was biased with a voltage of 2800 mV by a 33220A Agilent pulser at a frequency of 400 Hz using a custom programmed positive PIN diode waveform for each pulse. As mentioned in chapter 5 the UV illumination device is not able to deliver an uniform illumination across the entire electron disc. This results in low statistics on approximately two thirds of the pixels which are therefore excluded in the following analysis. In figure 6.5 a combined spectrum for 63 pixels with sufficient statistics is shown. The electron disc was held at a voltage of 18.6 kV and the magnets were at nominal fields (6 T and 3.6 T). At the high energy tail of the peak a little bump can be seen at ~ 22 keV. This is due to a previously unknown background effect, which is discussed in section 6.3. Looking at the global event rates on the detector for the measurements at different voltages (see table A.4 in the appendix) an increase of the rate with energy can be seen with a flat region between ~ 9 keV and 17 keV. At energies below 9 keV the low-energy tail of the peak reaches the noise threshold of the detector which results in a drop of the rates. At energies above 17 keV the above mentioned background effect becomes significant resulting in higher rates at the higher energy side of the peak. These effects will influence the dead-layer determination of the detector wafer in section 6.4. In comparison with the ^{241}Am -spectrum the peak itself is not exactly Gaussian and its maximum is shifted towards lower energies with a low-energy tail. Besides the effect of backscattering from the detector wafer, this low energy bias is due to the effect of the dead layer of the detector,

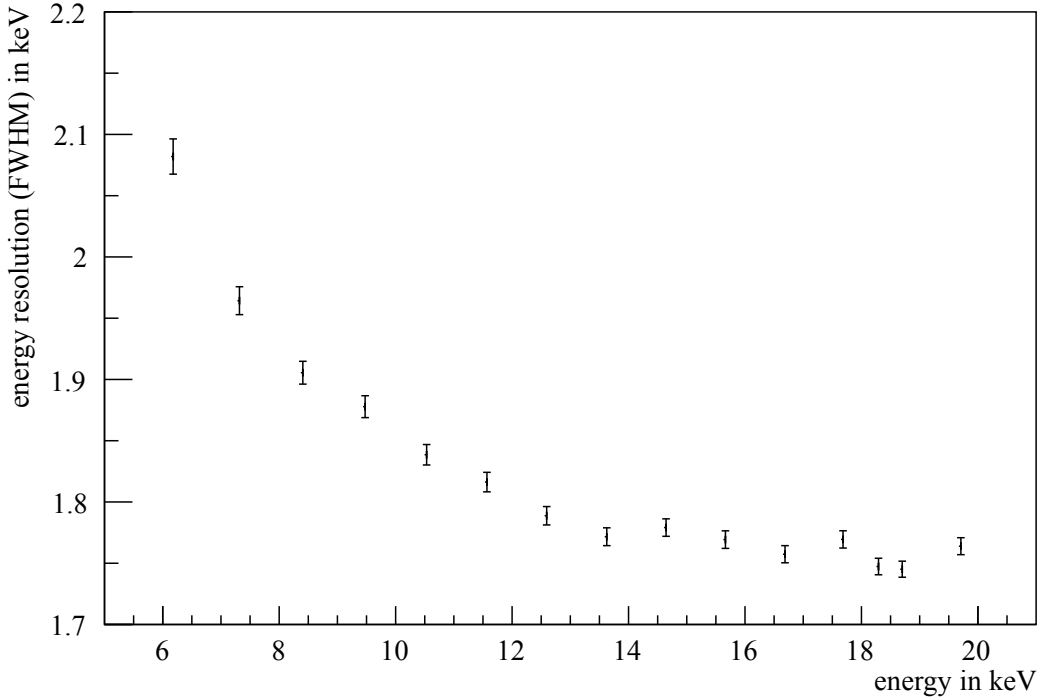


Figure 6.6.: **Energy Dependence of the FWHM Energy Resolution of the Detector Response to Monoenergetic Electrons.** The detector response is measured with the electron disc at different voltages and illuminated by the UV-LED. The statistical error bars on the energy resolution on the y-axis and the means of the Gaussian fit on the x-axis are introduced by the uncertainty of the fit. The combined spectra for all pixels with a sufficient illumination are used.

which affects the detector response to electrons but not to γ -photons. A Gaussian fit is done in the region of the peak center in the global spectra for different voltage settings of the electron disc. The number of pixels (with sufficient statistics) included in the analysis is energy dependent and can be found in table A.4 in the appendix. The resulting energy resolutions (FWHM) are plotted as a function of the electron energy in figure 6.6. The influence of the scattering in the ADC-to-energy calibration factors as a systematic is neglected in this analysis as well as the offset in the energy calibration. An increase of the energy resolution from ~ 1.75 keV at high energies to above 2 keV at low energies is found. This is due to the greater fraction of the energy loss of the low energy electrons in the dead layer and the generation of less information carriers by the incident of a low-energy electron on the detector (see chapter 4). The energy dependence is compatible with the results found in the Seattle measurements (see [1]).

6.3. Auger Background

During measurements with the electron disc at high voltage a bump in the energy spectrum of the detector response was found a few keV above the actual peak (see section 6.2.2 figure 6.5). A closer investigation of this effect revealed that it does not disappear when the UV illumination of the electron disc is turned off. In this case, the global count rate on the detector is still up to 300 Hz. In figure 6.7 the distribution of the event rates per pixel is shown. It appears that the effect is most significant in the upper right corner of the detector. Looking at the energy spectrum of pixel 103 in figure 6.8, which was taken with

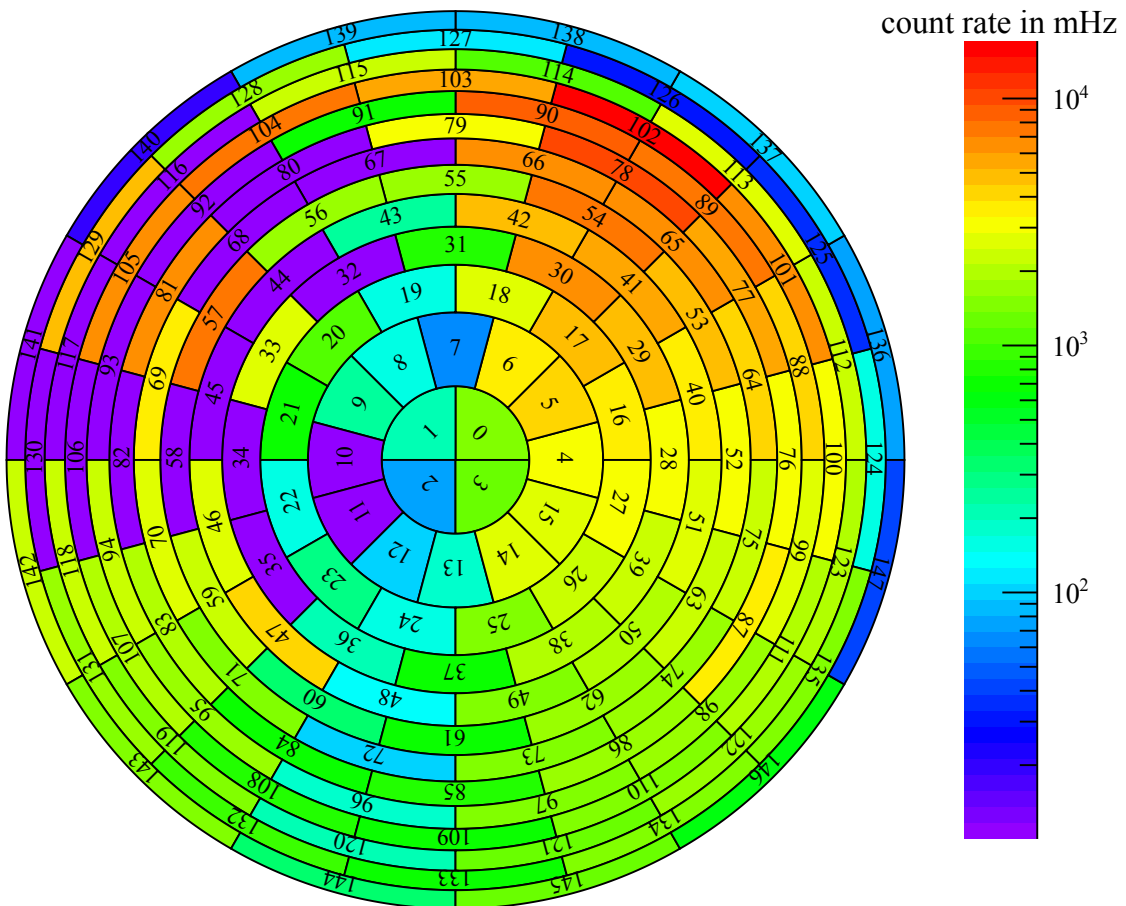


Figure 6.7.: Background Rates on the Detector with the Electron Disc at High Voltage. The magnets are at nominal fields (6 T and 3.6 T) and the UV-LED is turned off. In the upper right corner high rates up to over 10 Hz per pixel suggest a distinct region for the creation of the background effect.

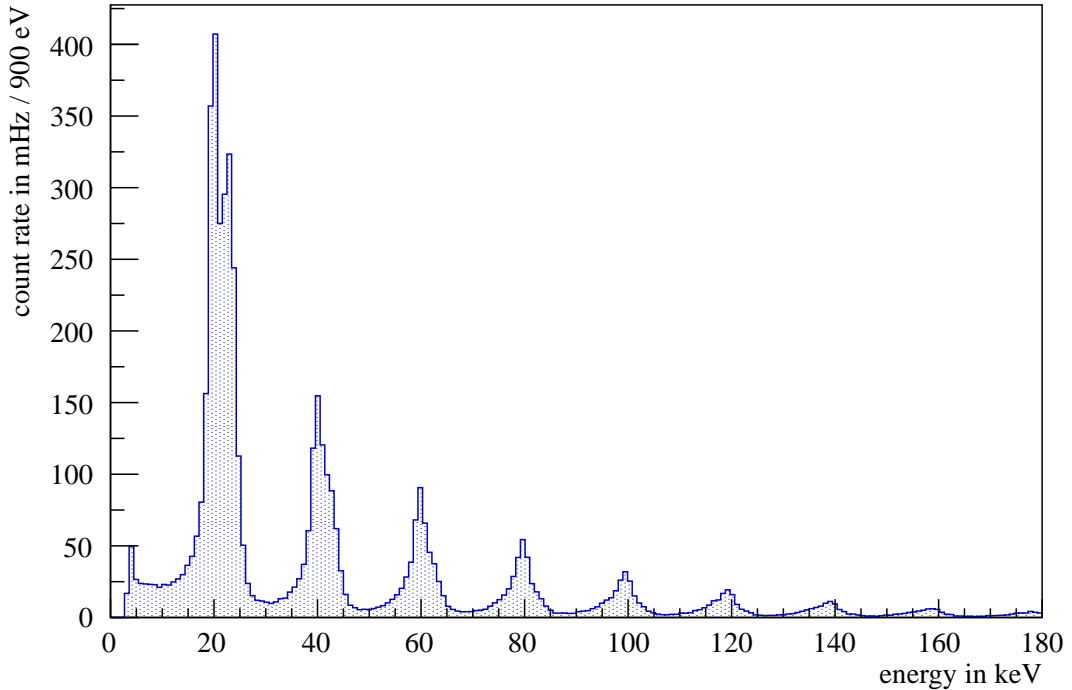


Figure 6.8.: **The Energy Spectrum of the Electron Disc Background for Pixel 103** shows multiple, equidistant peaks when the disc is at high voltage (20 kV) but not illuminated with UV light. Each peak is split into two but the splitting can only be resolved by the detector for the peak at 20 keV. At higher energies it is visible as a shoulder on the high energy side of the main peak. This spectrum is representative for all pixels which are affected by this background effect.

the electron disc at 20 kV multiple peaks can be seen at 20 keV, 40 keV, 60 keV and so on. In addition, each peak shows a second smaller peak, 3 to 4 keV above the main peak, which can only be resolved by the detector at low energies. Since this background affects all measurements with the electron disc at high voltage, in particular the dead layer determination in section 6.4, it has to be well understood. A promising explanation of it is given in [79] and is summarized in section 6.3.1. To verify this theory various measurements were done, which are presented in section 6.3.2.

6.3.1. Theory of Background Production

The electron disc is suspended in the middle of the flux tube by a short gold-plated titanium rod connected to a longer stainless steel rod by a glass-break. This is needed as an electric break for the high voltage and is covered by an aluminum shroud to prevent damage on it. If, for some reason electrons are emitted from the high voltage part of the electron disc's mounting structure, there will be a possibility that these electrons are guided magnetically to a copper band, which surrounds the ceramic break of the post-acceleration electrode. With an energy of more than 9 keV these incident electrons can generate characteristic fluorescence lines by the knocking-out of shell electrons in copper. It is assumed that X-ray emission lines from the copper K-shell with $E \sim 8$ keV [80] are most likely. From the copper band the generated X-rays are emitted isotropically and some fraction of these X-rays will strike the titanium electron disc. A ~ 8 keV X-ray has a high probability to knock out a K-shell electron from a titanium atom. With its low valency of $Z = 22$ in titanium the probability of relaxation by emission of Auger electrons is higher than

Table 6.1.: **Auger Transition Lines of Titanium** with the transition probability and the corresponding energy. In the context of Auger electrons, the probabilities of all possible transitions add up to 100%. In this table only transitions with probabilities higher than 10% are shown [62].

Transition	Probability in %	Energy in keV
KL ₃	12.7	4.51
KL ₁ L ₃	10.9	3.92
KL ₂ L ₃	25.7	4.00
KL ₃ L ₃	14.5	4.01

Table 6.2.: **Fit Results for the Double-Peak Structure of the Auger Background.** The goodness-of-fit is given by $\chi^2 = 9.34$.

Description	Energy in keV
Mean first peak	19.76 ± 0.07
Sigma first peak	0.92 ± 0.06
Mean second peak	22.8 ± 0.1
Sigma second peak	1.37 ± 0.09

the probability for the emission of X-rays. KLL-Auger electrons have a particularly high probability to get generated with typical energies in the region of ~ 4 keV (see table 6.1). A number of Auger electrons from higher shells with energies close to 0 keV are emitted by a subsequent relaxation of the titanium atom. If these low-energy electrons leave the titanium disc in the direction of the detector, they will be accelerated from the titanium disc at high voltage towards the wafer at a potential of 120 V by the electric field. This results in multiple peaks seen in the detector response spectrum in figure 6.8. E.g., two low-energy Auger electrons are emitted from the same atom in the titanium plate at 20 kV with a delay time (< 50 ns), which cannot be resolved by the detector. Therefore, they will contribute to a peak at 40 keV in the detector response spectrum. If in addition to such low-energy Auger electrons, a high energetic K-shell Auger electron (with ~ 4 keV) is emitted in a way where it is guided to the detector, it will contribute together with the two low-energy electrons to a peak at ~ 64 keV in the spectrum. This theory explains the multiplicity of the peaks in the background spectrum as well as the splitting of each peak. Due to the multiple contribution possibilities to the peaks at ~ 44 keV, ~ 64 keV, ~ 84 keV and so on the detector is not able to resolve the contributions from each Auger transition line and the peak splitting is smeared out. Detailed simulations with Penelope 2008 [81] support the theory regarding the possibility of a 9-keV X-ray knocking out a K-shell electron from the titanium atom.

6.3.2. Background Measurements and Results

The data from a 17-hours long background measurement with the electron disc at 20 kV and the UV LED turned off is used to fit the double-peak structure from 18 to 26 keV with two Gaussian functions (see figure 6.9). The results can be found in table 6.2. The peak-to-peak distance of $E_{\text{split}} = 3.04$ keV is actually ~ 1 keV lower than the energy of the K-shell Auger electrons predicted by the theory. Nevertheless, due to the influence of the detector dead layer the inaccuracy of the fit ($\chi^2 = 9.34$) and a possible energy loss of the Auger electrons during their emission from the titanium disc by collisional ionization and

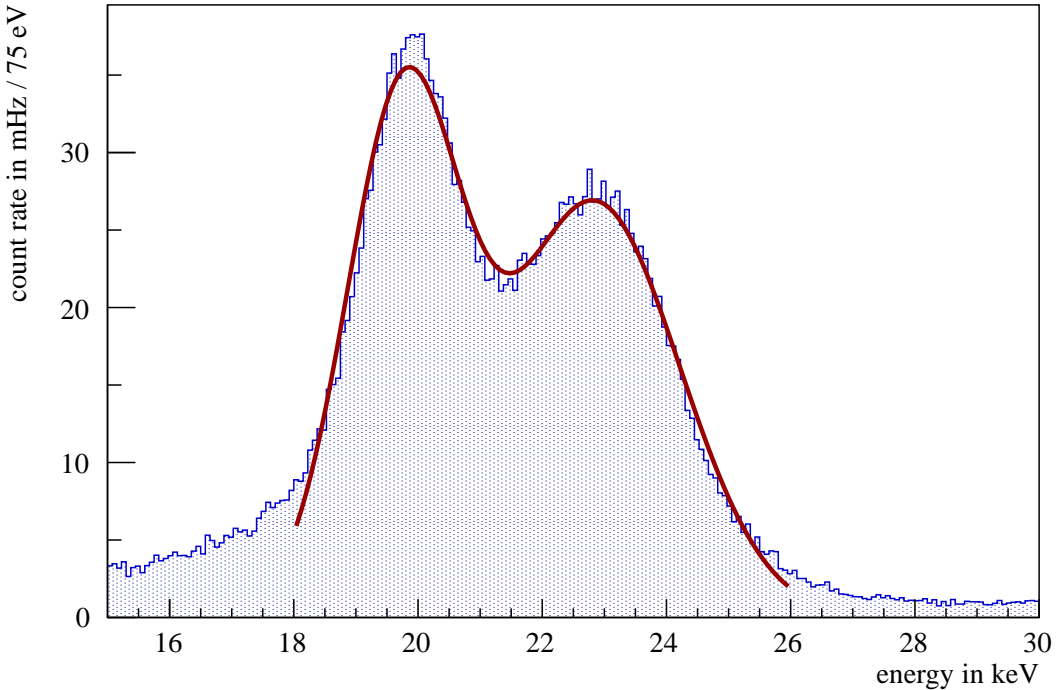


Figure 6.9.: The Splitting of the First Background Peak of Pixel 103 is fitted with two Gaussian functions (red line). The distance between the peaks is calculated out of the fit results to $E_{\text{split}} = 3.04 \text{ keV}$.

bremsstrahlung it is still in good agreement with the theory. In addition, a measurement of the detector response with the electron disc at 8 kV, below the energy threshold for a X-ray fluorescence of copper, was performed. At this voltage the background effect disappeared, which is a good indication that the theory is valid. Even if the probability for an emission of Auger electrons from the disc is higher than for a X-ray emission, a small peak at ~ 4 keV due to X-rays should still be visible in the spectrum. To look for this peak a measurement with the threshold of the detector lowered to ~ 3 keV was done, but the high noise rate at such low energies makes it impossible to see the peak. In a number of measurements with the electron disc at different voltages and the UV light turned off a rate-to-voltage dependency of the background effect is found, which is compatible with the rate increase found in the measurements for the energy resolution with the electron disc discussed in section 6.2.2. Especially at voltages above 17 keV the background rates increase significantly. To determine the spot on the electron disc holding structure where electrons are emitted from, measurements were performed with the electron disc raised by a few cm. Even with the disc retracted by ~ 12 cm the background effect does not disappear. Nevertheless, looking at the radial distribution of the event rates on the detector a trend upwards is visible when the disc is raised. Due to the limited radial and angular resolution of the detector a more detailed investigation of the spot of emission is not possible. During the installation of the various upgrades for the FPD system (see chapter 5) an investigation of the electron disc's holding structure was carried out to determine the location of the field emission. Two marks on the aluminum shroud which covers the glass-break were found with their counterpart marks on the inner surface of the vacuum chamber. At these points field emission takes place, while the electron disc is at high voltage, generating the electrons which could then create the background effect as described in the theory above. In addition, a misalignment of the electron disc was found during the disassembly which explains the fact that the background is not dominant at detector pixels at the top of the

wafer but on pixels in the upper right corner of the detector. During the re-assembly of the FPD system the electron disc is aligned correctly and a glass tube is inserted, which surrounds the holding structure of the electron disc and should prevent a field emission. Therefore, it is expected that the background effect will disappear when the next set of data is taken.

6.4. Dead-Layer Determination

In order to achieve a better understanding of the FPD system and the influence of its performance to the neutrino mass measurement of the KATRIN experiment, a knowledge of the detector wafer's dead layer is of great importance. The dead layer of a semiconductor diode detector denotes the non-sensitive volume of the detector. A more detailed discussion on the properties of such detectors can be found in chapter 4. The goal of the manufacturer of the wafer (Canberra, Belgium) was to achieve a dead layer thickness of 100 nm. To verify this a comparison of a simulated detector response on monoenergetic electrons with the data taken with the FPD system is carried out. The data used for the dead-layer determination is the same as for the determination of the energy resolution with the use of the electron disc in section 6.2.2 and will be mentioned from now on as 'dead-layer-data'. Information regarding the different measurement settings can be found in table A.4 in the appendix. The simulation is done with KESS/KASSIOPEIA and will be discussed in section 6.4.1. A χ^2 -comparison of the simulated spectra and the dead-layer-data is done and described in section 6.4.2. The results of the analysis as well as systematic effects which influence the results are discussed in section 6.4.3.

6.4.1. Simulation

To simulate the electrons that are emitted from the titanium disc and accelerated towards the detector by potentials of up to 20 kV the global KATRIN simulation package KASSIOPEIA [59] is used. With a detailed geometry of the detector region, the titanium disc as well as the magnetic fields of the Pinch and the Detector Magnet, no significant influence of the electron trajectory on the energy spectrum of the electrons at the detector is found. Thus, to save CPU-time, the electrons in the following simulations start 1 mm in front of the detector with an energy given by the potential of the electron disc plus 120 V bias voltage of the detector wafer. Their starting angles are isotropic distributed with the maximum polar starting angle restricted to 78.4° by the magnetic mirror effect (see formula (3.5)). For various energies between 7 keV and 20 keV simulations with different dead-layer depths of the detector wafer between 20 nm and 250 nm are carried out using KESS. The detailed simulation settings can be found in table A.6 in the appendix. In figure 6.10 a simulated detector response spectrum for one million 15-keV electrons and a dead layer thickness of 120 nm is shown. In the simulation the energy resolution of the detector is not included. Therefore, the spectrum has to be smeared out by a Gaussian function with a standard deviation determined with the ^{241}Am source to be able to compare it to a measured spectrum obtained with the electron disc at high voltage. Here it is not reasonable to use the energy resolution determined with the electron disc since this resolution depends on the dead layer itself. The low energy tail of the spectrum in figure 6.10 is due to the energy losses of the electrons in the dead layer and to the effect of backscattering from the detector wafer.

6.4.2. Analysis

To derive the dead layer of each detector pixel a χ^2 -comparison between the dead-layer-data and the simulations is carried out with the simulated dead layer as a free parameter. For a better understanding of the analysis procedure an overview of the analysis is given

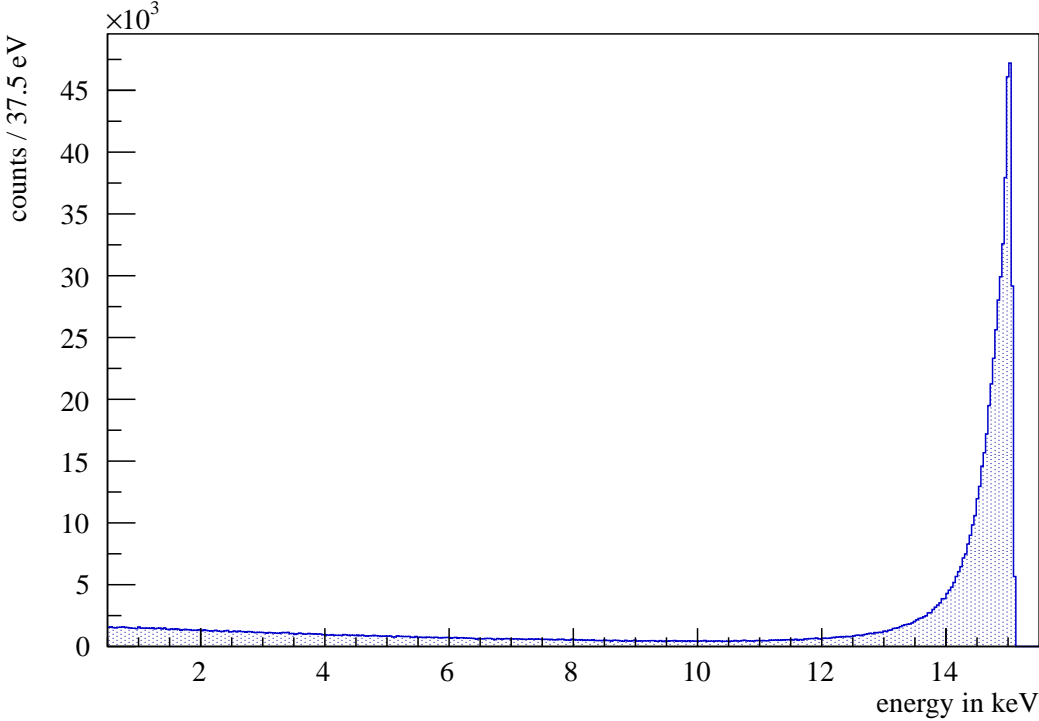


Figure 6.10.: **The Simulated Detector Response for 15.12-keV Electrons** and a detector dead layer of 120 nm. Note that the 120 V bias voltage of the detector is taken into account in the simulation.

in figure 6.11. Since the UV illumination of the electron disc is not uniform across the disc approximately two thirds of the detector pixels have to be excluded from the analysis due to low statistics. Here, the number of excluded pixels differs between the measurements at different voltages on the electron disc (different energies of the electrons). The number of excluded pixels per voltage setting can be found in table A.5 in the appendix. Note that the number of excluded pixels increases with decreasing energy, since the detector response peak reaches the threshold. The energy calibration of the dead-layer-data differs from the usual ^{241}Am calibration technique described in section 6.2.1. The calibration measurement used for the dead-layer analysis was performed with the magnets at nominal fields (6 T and 3.6 T) and the ^{241}Am -source fully inserted into the flux tube. The Gaussian smearing of the simulated spectra is well described by using the standard deviations obtained from this calibration measurement for each pixel. As discussed in section 6.2.1 a few pixels in the middle of the detector have to be excluded from the analysis due to the Compton spectra in the ^{241}Am -data. In order to get information comparing the goodness-of-fit of a simulated spectrum with a distinct dead layer to the detector response of the FPD system, a χ^2 -comparison of the two weighted histograms of the spectra is performed according to:

$$\sum_{i=1}^r \frac{(W_1 w_{2i} - W_2 w_{1i})^2}{W_1^2 s_{2i}^2 + W_2^2 s_{1i}^2} \quad \text{with} \quad W_{1/2} = \sum_{i=1}^r w_{1/2i} \quad (6.2)$$

Here, $w_{1/2i}$ are the common weights of events in the i -th histogram bin and $s_{1/2i}^2$ are the variance estimators of the normal distributions assumed for the weights in each histogram bin [82]. As an example the measured spectrum at a disc voltage of 15 kV and the simulated spectrum for electrons with 15.12 keV and a detector dead layer of 40 nm are shown in figure 6.12. The simulated spectrum is scaled to the number of events in the measured spectrum and the 120 V bias voltage of the detector is taken into account in

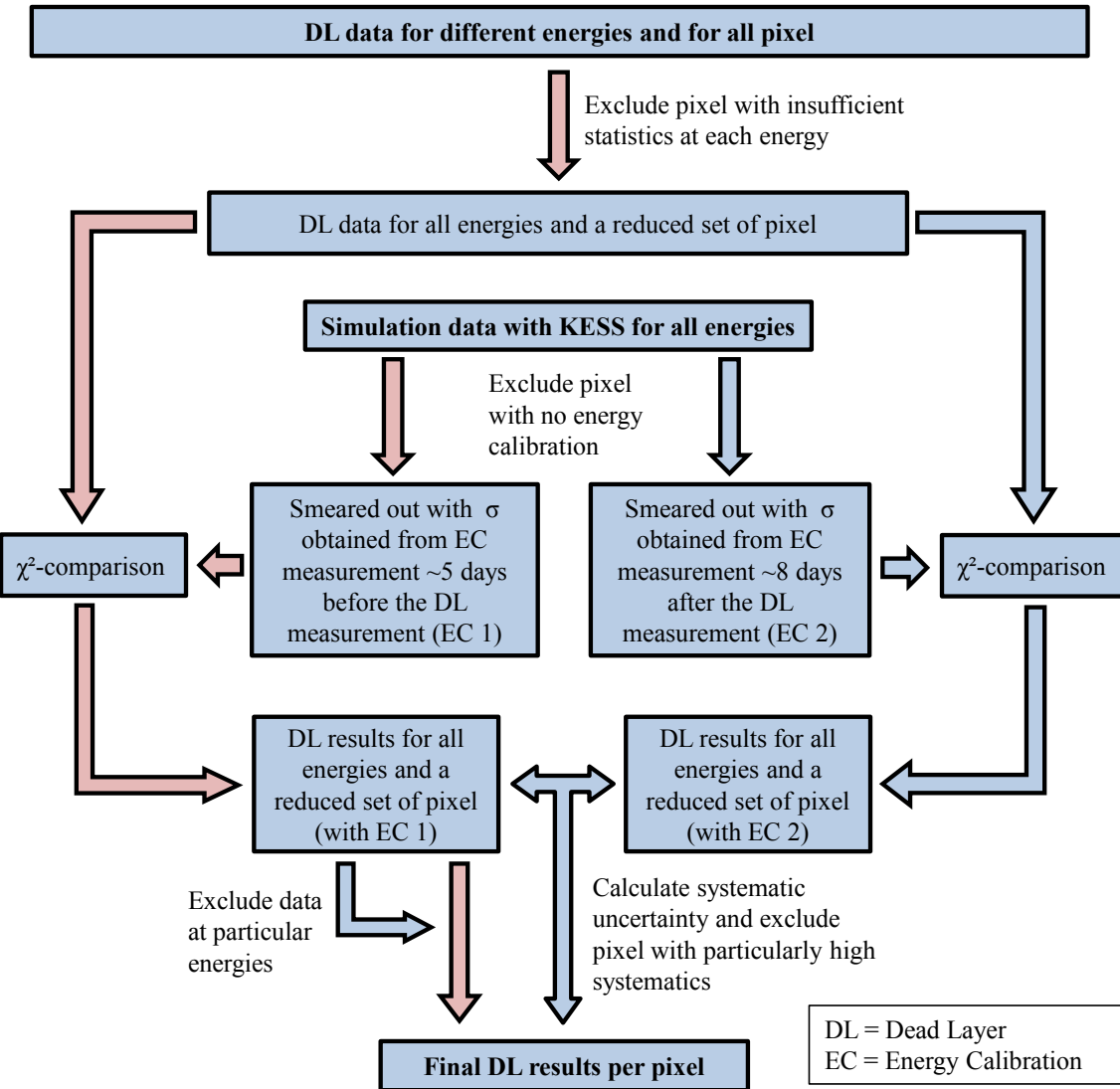


Figure 6.11.: **Flow-Chart of the Dead-Layer Analysis Procedure.** The red arrows trace the main part of the analysis.

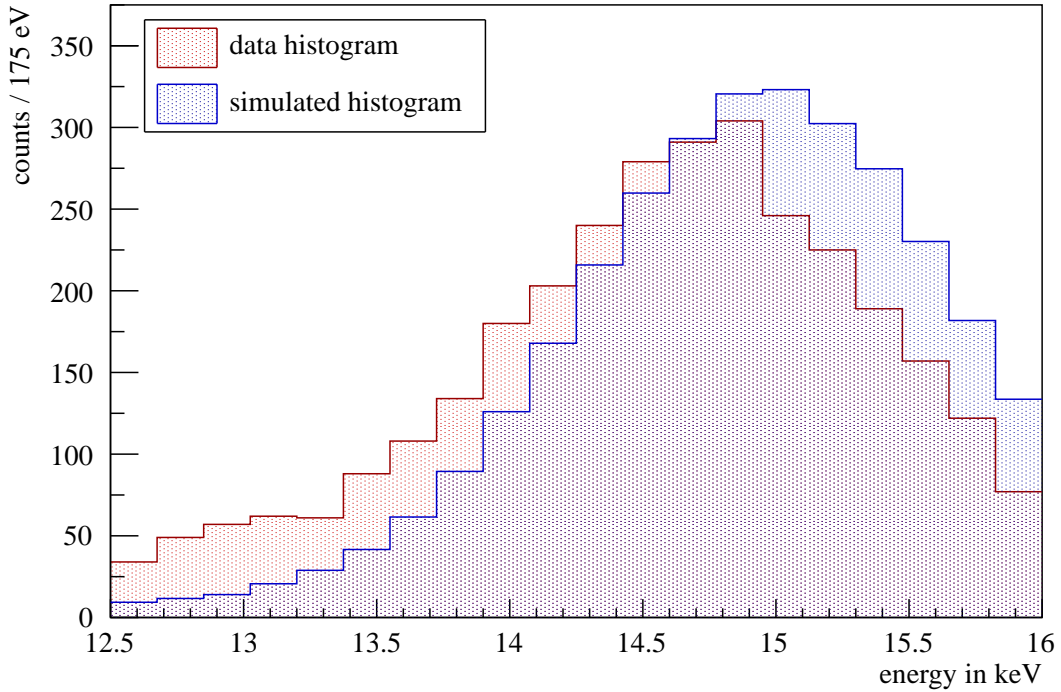


Figure 6.12.: The Spectra of the Measured and the Simulated Detector Response of Pixel 54 at an Energy of 15.12 keV are compared for a simulated dead layer of 40 nm. The number of events in the simulated spectrum is scaled to the number of events in the measured spectrum.

the simulation. It is clear that the simulation for a dead layer of 40 nm in figure 6.12 does not fit with the measured data. The energy range on which the χ^2 -test is applied to the spectra is set individually for each pixel, energy and dead layer, to minimize the number of bins with low statistics. With the use of the χ^2 -test a binning dependency is introduced into the analysis, which influences the statistical uncertainty of the dead layer in particular. To determine the correct bin width w for each χ^2 -comparison Scott's rule is applied in the assumption of a Gaussian-like shape for the peaks in the spectra [83]:

$$w = \frac{3.49 \cdot \sigma}{n^{1/3}} \quad (6.3)$$

Here, σ is the standard deviation obtained from the ^{241}Am calibration data and n is the number of events in the energy region where the χ^2 -test is applied. The χ^2 -test is done for each combination of pixels, energy and dead layer, and the resulting reduced χ^2 -values are plotted for each pixel and energy over the different dead layer depths as is shown in figure 6.13. To derive the exact value for the dead layer of each pixel at a given energy the data points are fitted with a 4th-order polynomial to get the minimum reduced χ^2 -value. A 4th-order polynomial is needed, since the peaks of the spectra are not symmetrically distributed around their mean and therefore, the derived χ^2 -values do not form a parabola. The upper and lower statistical uncertainties on the dead layer are derived from the curvature of the 4th-order polynomial close to the minimum according to:

$$\Delta\chi^2 = \chi^2 - \chi^2_{\min} = 1 \quad (6.4)$$

As described above the energy calibration in this analysis is done using a different calibration data than usual. This is due to a scattering of the 59.54-keV peaks ADC value per

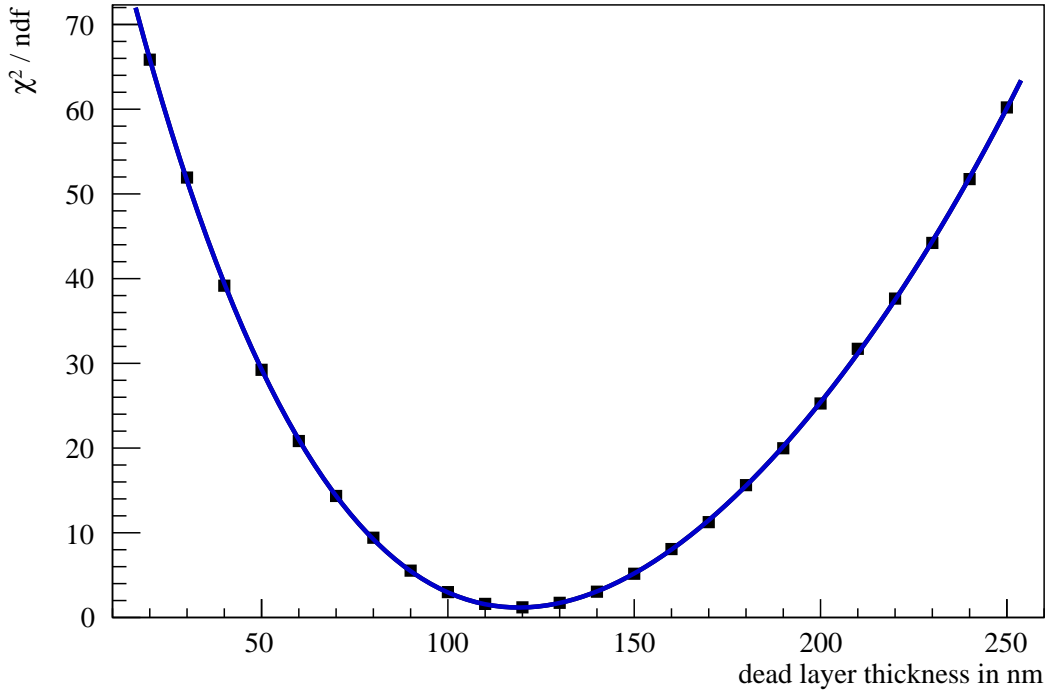


Figure 6.13.: The χ^2 Dependency on Dead Layer for Pixel 53 at an Energy of **15.12 keV** is fitted by a 4th-order polynomial (blue line) to determine the dead layer. The plot is representative for all pixels with a sufficient illumination.

pixel between different calibration measurements. The calibration data used for this analysis was taken ~ 5 days before the dead-layer-data was measured whereas the calibration data used in all other analyses was taken ~ 8 days afterwards. Therefore, the uncertainty regarding which is the correct energy calibration of the detector at the time when the dead-layer-data was taken, is represented by a systematic uncertainty on the dead-layer results. The influence of the calibration offset, which was not considered in the other analyses, is small enough to be assumed as included in this systematic. To determine the systematic uncertainty two different analyses of the dead-layer-data were performed. One with the use of the energy calibration data taken ~ 5 days before (λ_1) and one with the calibration data taken ~ 8 days after the measurement of the dead-layer-data (λ_2). This results in two different dead layer values for each pixel and energy where the difference between the dead layers $\Delta\lambda = \lambda_1 - \lambda_2$ is determined by the change of the ADC-to-energy conversion between the two different calibration data sets. Since the 59.54-keV peaks ADC values per pixel scatter in the range of a few ADC channels between different energy calibration measurements and do not show a clear drift with time (see section 6.2.1), the actual result for the dead layer cannot be interpolated from the results of the two analyses. Therefore, for a given energy the results on $\Delta\lambda$ for all pixels which were used in the analyses show a Gaussian-like distribution with the mean shifted a little bit towards negative values of $\Delta\lambda$. The mean and the standard deviation obtained from a fit of the distribution are used to calculate a systematic uncertainty for the dead layer of the detector at a given energy:

$$\begin{aligned} s_{\lambda,+} &= \Delta\lambda_{\text{mean}} + \sigma_{\Delta\lambda} \\ s_{\lambda,-} &= \Delta\lambda_{\text{mean}} - \sigma_{\Delta\lambda} \end{aligned} \quad (6.5)$$

Thus, the actual value of the dead layer and its statistical uncertainty for each pixel and energy is obtained with the use of the energy calibration that took place ~ 5 days before the

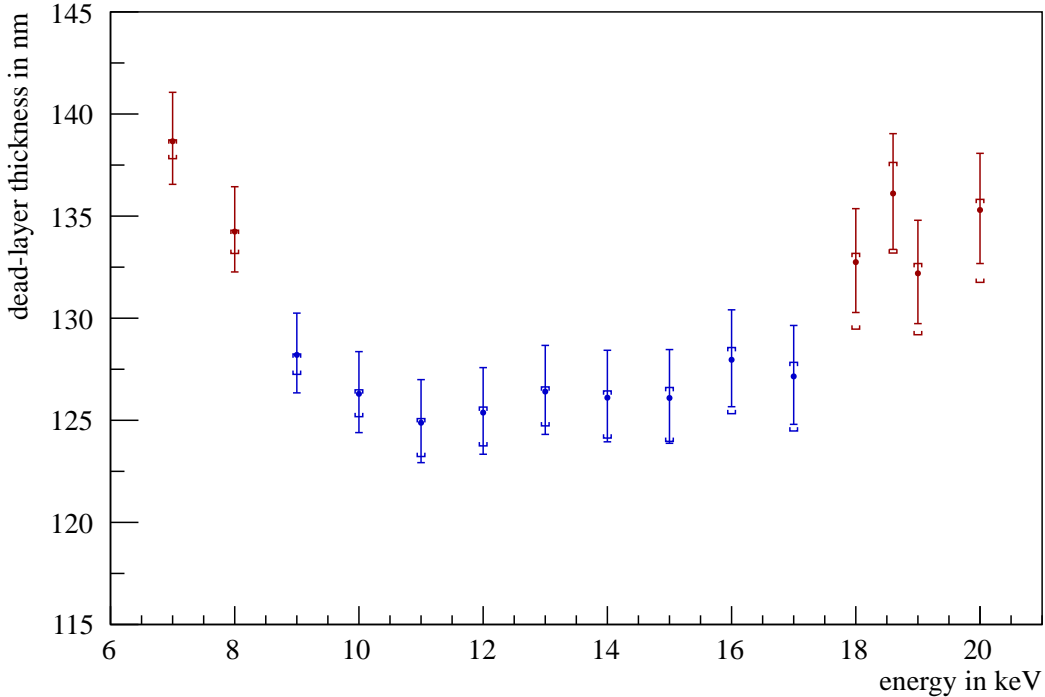


Figure 6.14.: **The Energy Dependency of the Global Detector Dead Layer** is shown with statistical error bars. Approximately two thirds of the pixels are excluded from the analysis because of insufficient illumination, high drifts in the energy calibration or the influence of Compton spectra in the energy calibration. For all other pixels the influence of the drift in the energy calibration is estimated as a systematic uncertainty (shown in brackets). The dead layer results for energies below 9 keV and above 17 keV (red dots) are excluded from the further analysis.

dead-layer-data was taken, while the systematic uncertainty on the dead layer is derived by the analysis of the dead-layer-data with both energy calibration data sets and the use of formula (6.5). Since the dead layer differences $\Delta\lambda$ of certain pixels are found to be significantly higher than for the majority of the pixels, these high values are not included in the Gaussian fit and the affected pixels are excluded in the further analysis. The number of pixels used in the analysis for each energy can be found in table A.5 in the appendix.

6.4.3. Dead Layer Results

The analysis described above is applied to the data of 15 measurements at different energies and in figure 6.14 the resultant global dead-layer thicknesses for the whole detector are plotted over the energy of the different measurements with statistical error bars and the systematic uncertainty shown in brackets. While there is no physical dependency of the dead-layer thickness to the energy of the electrons, a dependency is found at low and high energies. At energies below 9 keV the low energy tail of the detector response peak reaches the energy threshold of the detector which introduces an energy dependence in the χ^2 -comparison of the simulated and measured spectrum. This results in an increase of the dead-layer result at low energies. At energies above 17 keV the background effect described in section 6.3 significantly influences the detector response spectrum above the actual peak. This introduces an energy dependence into the χ^2 -comparison, as well and results in an increase of the obtained dead-layer results at high energies. To derive the final

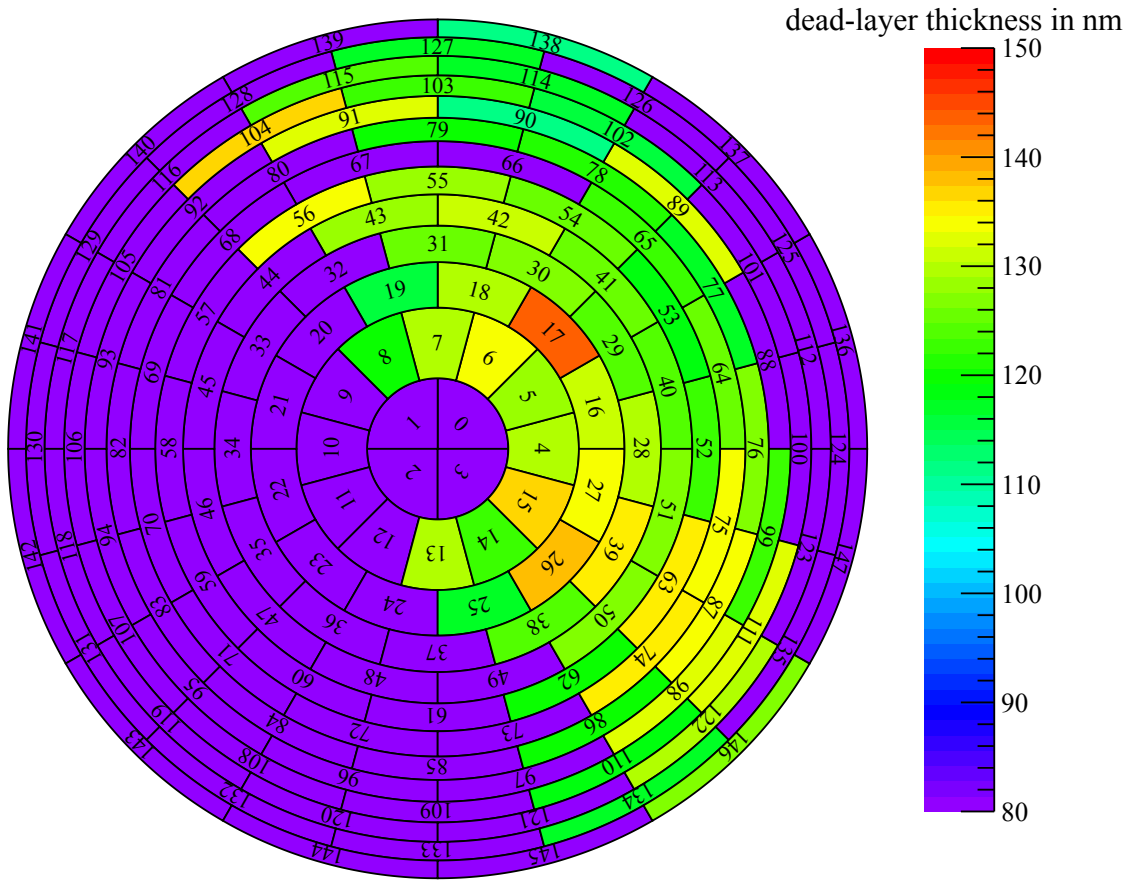


Figure 6.15.: **Dead Layers of the Detector Pixels** obtained by a combined analysis of the measurements at different energies. The exact values for each pixel with uncertainties can be found in table A.3 in the appendix. Approximately two thirds of the pixels are excluded from the analysis due to various reasons (purple pixels). In addition, the measurements with energies below 9 keV and above 17 keV are excluded.

results on the detector dead layer for each pixel the data from the measurements at energies above 17 keV and below 9 keV are excluded, while the results from the measurements with energies in between are averaged for each pixel. In figure 6.15 the dead-layer thicknesses of each pixel are shown. Note that statistical uncertainties as well as systematic uncertainties are not shown in the plot but can be found in table A.3 in the appendix together with the exact dead-layer result for each pixel. The mean dead layer for 61 pixels used in the analysis is given by:

$$\lambda_{\text{global}} = 126.4 \pm 0.8 \text{ (stat.)} {}^{+0.2}_{-1.2} \text{ (syst.) nm} \quad (6.6)$$

It is a little bit higher than the goal stated by the manufacturer of 100 nm. Nevertheless, since only approximately one third of the detector pixels are used for the analysis and impurities on the detector wafer cannot be ruled out, the result on the dead-layer thickness is reasonable. After the installation of upgrades to the FPD system in summer 2012, further measurements are planned to determine the wafer's dead layer. Additionally, a different analysis approach is intended where the detectors energy resolution for electrons is used as a second free parameter. This will allow a more accurate result on the energy resolution for electrons as well as an independency of the dead-layer results from the energy resolutions obtained with the ^{241}Am source.

7. Conclusion

The KArlsruhe TRItium Neutrino (KATRIN) experiment aims to probe the mass of the electron antineutrino by the detailed model-independent investigation of the tritium β -decay spectrum close to its endpoint energy of 18.6 keV. The β -electrons generated in a high intense source with an unsurpassed rate of 10^{11} per second are guided magnetic adiabatically through a transport section and two retardation spectrometers, the pre- and the main spectrometer, to a Focal-Plane Detector (FPD). While the high-resolution main spectrometer acts as a high energy-pass filter, it measures the integrated tritium β -spectrum with an energy resolution of $\Delta E = 0.93$ eV. Only a small number of β -electrons can pass its analyzing plane. This results in a count rate of a few mHz on the FPD, which therefore needs a high background reduction combined with a high detection efficiency. The FPD system was designed, built and tested by the KATRIN collaborators in Seattle, Washington, USA to meet these goals and was shipped to the Karlsruhe Institute of Technology (KIT) in summer 2011.

The objectives of this thesis were the assembly of the FPD system and the detailed investigation of its performance in the KATRIN main spectrometer hall. The findings gained in this process are listed in the following for each subsystem. In addition, the results from first measurements are presented of whom some are compared to Monte Carlo simulations.

Within the FPD system two superconducting magnets form the magnetic field which guides the β -electrons from the main spectrometer to the detector wafer. To ensure a lossless transport of the electrons the magnets have to achieve a stability of 0.1% per month. Besides a 'training' quench of the Detector Magnet during its first ramp-up at KIT, right after its shipment and installation, the magnets meet their performance specifications. They were successfully tested together at their maximum field of 6 T each. In addition, the drift of the magnetic flux density was measured inside the Pinch Magnet's warm bore with a nuclear magnetic resonance probe with both magnets at nominal fields ($B_{\text{Pinch}} = 6$ T, $B_{\text{Detector}} = 3.6$ T) and found to be 0.0015% per month, well within its design criteria.

To suppress the scattering probability of β -electrons on residual gas the beam tube of the FPD system has to be held at a pressure of 10^{-11} mbar like the pre- and main spectrometer. At KIT, a pressure of $3 \cdot 10^{-10}$ mbar in the beam tube has been reached, so far. In summer 2012, after the installation of various upgrades to the FPD system a long bake-out period for the beam tube is scheduled. It is expected that the pressure will reach its design goal afterwards. A separate High Vacuum (HV) chamber surrounds the beam tube and houses the FPD read-out electronics. The design pressure of 10^{-6} mbar in the chamber was reached at KIT.

A Post-Acceleration Electrode (PAE) forms the boundary between the beam tube and the HV chamber and was designed to provide potentials of up to 30 kV in order to boost the β -electron signal to energy regions with lower backgrounds. At KIT, the PAE was not able to run stably at more than 8 kV up until now. At higher voltages discharges occurred. During the installation of the system's upgrades the cause of the discharges was traced to a displaced gasket and was fixed. In addition, the original PAE was deformed by high mechanical stress and will be replaced by a more robust one. Therefore, after the re-assembly of the system a stable operation of the new PAE close to its design value is expected.

The PAE, the detector wafer and the in-vacuum read-out electronics of the FPD system are actively cooled by a pulse tube cooler. At KIT, the temperatures of the wafer and the electronics were found to be between 10 K and 40 K higher than in Seattle. This might be due to a bad thermal connection at some point and the increased heat inputs (17.4 W compared to a design value of 15 W) by a new set of read-out electronics which was installed for the first time. Because of a higher heat load of the new PAE a more efficient cooling system has been designed and built in Seattle. Once successfully tested, it will be installed to the system in summer 2012.

The FPD wafer is segmented into 148 pixels, each with an individual read-out electronics channel. During the measurement period of this thesis one detector quadrant was found to be cabled incorrectly inside the HV chamber. This results in 13 dead channels in this quadrant. In addition, 11 read-out channels of the detector showed a high noise level or crosstalk. During the installation of a new set of electronics in summer 2012, various tests are proposed to ensure a correct cabling and good electric connections of the in-vacuum electronics. In addition, shields (DONUTs) for the glass feedthroughs from the preamplifiers to the wafer will be installed and should reduce the intrinsic detector background by up to an order of magnitude.

To calibrate the FPD system in stand-alone mode a number of calibration systems are installed and were used during the measurement period relevant for this thesis. In this context two major problems occurred. On the one hand, a high-activity ^{241}Am source for a calibration of the FPD to monoenergetic γ -photons had not been shipped to KIT, yet. Thus, all measurements of this type had to be performed with a weaker source and a high statistics calibration of the detector was therefore not possible as often as was needed. On the other hand, during measurements of the detector response on monoenergetic electrons, an UV illumination device was used to generate photoelectrons on a titanium disc. These electrons were subsequently accelerated by a high electric field towards the detector wafer. The illumination of the disc was not uniform at KIT, resulting in a loss of approximately two thirds of the detector pixels for the analysis. At the moment the illumination device is revised and a better performance is expected to be achieved in summer 2012.

To reduce the background induced by cosmic muons hitting the detector wafer an active veto system is installed in the FPD system. It consists of six scintillator panels surrounding the detector wafer with their optical signals read-out by Multi Pixel Photon Counters (MPPCs) which are located together with the amplifying electronics in a separate box. After the veto system was assembled at KIT, its electronics were found to operate extremely unstably and were modified during this thesis. This was successfully done by the installation of additional grounding connections between the MPPCs and the electronics to avoid oscillations in the signal read-out. In addition, a new water cooling system was designed and installed to ensure stable operating temperatures of the MPPCs.

During a data-taking period in spring 2012, the linearity of the detector electronics was measured with the use of a pulsed red LED shining onto the FPD wafer with different intensities. In this way, the linearity of the detector response was found to be more than

sufficient. A higher result for the fractional deviation (5%) from linearity compared with the results from Seattle can be explained by the different analysis approach at KIT.

The energy calibration of the detector was performed with the ^{241}Am source and a non-neglectable scattering of the calibration results per pixel was found with time. This emphasizes the need for a high-activity source which would allow fast calibration measurements and thus, enable a calibration of the detector before each measurement.

The global energy resolution of the detector response to 59.54-keV γ -photons was found to be $\Delta E = 1.637 \pm 0.004$ keV (FWHM). For 18.6-keV electrons an energy resolution of $\Delta E = 1.8 \pm 0.2$ keV (FWHM) was obtained where the high statistical uncertainty is due to a broadening of the response spectrum by dead-layer effects. Since the detector wafer is operated at a higher temperature than in Seattle, a better energy resolution is expected after the installation of the numerous upgrades to the system in summer 2012. These include the new cooling system, a new set of electronics and the DONUT shields.

During calibration measurements with the titanium disc at high voltage, a previously unknown background effect was noticed and subsequently investigated in detail. A theory that explains this background by the emission of Auger electrons from the titanium disc is supported by the results of the investigations. Due to upgrades to the support structure of the disc, the background effect is expected to disappear when the next set of data is taken.

To achieve a better understanding of the FPD system and its influences to the KATRIN experiment the dead layer of the detector wafer was determined by a comparison of data and Monte Carlo simulations for the detector response to monoenergetic electrons. The simulations were performed with the software package KESS (KATRIN Electron Scattering in Silicon), which was developed by the KATRIN collaboration and tracks low-keV electrons in silicon. The mean dead layer of 61 pixels is found to be:

$$\lambda_{\text{global}} = 126.4 \pm 0.8 \text{ (stat.)} {}^{+0.2}_{-1.2} \text{ (syst.) nm}$$

Therefore, it is slightly higher than the 100 nm the manufacturer of the wafer aimed for. With the noted improvements in the illumination of the titanium disc a measure of the dead layer of the entire detector will be possible.

As a final conclusion it can be stated that the current setup of the FPD system meets the requirements for the Spectrometer-Detector-Section (SDS) commissioning. To further enhance its performance, needed for the final KATRIN setup, various upgrades to the system will be installed in summer 2012. Another data-taking period is planned were the new installations will be tested in detail and the measurements presented in this thesis will be repeated. Furthermore, the timing resolution of the system will be derived and extensive background measurements with and without the veto system will be performed to determine the figure of demerit for the FPD system. With the connection of the system to the main spectrometer in fall 2012, the possibility for different other measurements including an investigation of the charge sharing between pixels, a detailed channel mapping of the detector and a determination of the backscattering properties of electrons from the detector wafer are possible with the use of an angular resolving electron gun.

Bibliography

- [1] A. Beglarian *et al.*, *Prototype focal-plane detector system for the KATRIN experiment*, 2012, internes KATRIN Dokument. [Online]. Available: <https://fuzzy.fzk.de/bscw/bscw.cgi/d722700/FPD-System-Prototype-Jan2012.pdf>
- [2] J. Updike, “Telephone poles and other poems,” *Knopf*, 1960, originally in The New Yorker.
- [3] C. Amsler, *Kern- und Teilchenphysik*. vdf Hochschulverlag AG an der ETH Zürich, 2007.
- [4] W. Pauli, “Dear radioactive ladies and gentlemen,” *Phys. Today*, vol. 31N9, p. 27, 1978.
- [5] J. Chadwick, “The Existence of a Neutron,” *Proc. Roy. Soc. A*, vol. 136, pp. 692–708, 1932.
- [6] E. Fermi, “Versuch einer Theorie der β -Strahlen,” *Zeitschrift f. Phys. A*, 1934.
- [7] F. Reines, C. L. Cowan, F. B. Harrison, A. D. McGuire, and H. W. Kruse, “Detection of the free antineutrino,” *Phys. Rev.*, vol. 117, pp. 159–173, 1960. [Online]. Available: <http://link.aps.org/doi/10.1103/PhysRev.117.159>
- [8] G. Danby *et al.*, “Observation of high-energy neutrino reactions and the existence of two kinds of neutrinos,” *Phys. Rev. Lett.*, vol. 9, no. 1, pp. 36–44, 1962.
- [9] DONUT Collab., “Observation of tau neutrino interactions,” *Phys. Lett. B*, vol. 504, pp. 218 – 224, 2001.
- [10] S. Eidelman *et al.*, “Review of Particle Physics,” *Phys. Lett. B*, vol. 592, pp. 1+, 2004. [Online]. Available: <http://pdg.lbl.gov>
- [11] Particle Data Group ; Nakamura, K. *et al.*, *J. Phys. G* 37, 075021, 2010, and 2011 partial update for the 2012 edition. [Online]. Available: <http://pdg.lbl.gov>
- [12] M. Goldhaber, L. Grodzins, and A. W. Sunyar, “Helicity of neutrinos,” *Phys. Rev.*, vol. 109, pp. 1015–1017, 1958. [Online]. Available: <http://link.aps.org/doi/10.1103/PhysRev.109.1015>
- [13] Y. Fukuda *et al.*, “Evidence for oscillation of atmospheric neutrinos,” *Phys. Rev. Lett.*, vol. 81, pp. 1562–1567, 1998.
- [14] R. Davis, Jr., D. S. Harmer, and K. C. Hoffman, “Search for neutrinos from the sun,” *Phys. Rev. Lett.*, vol. 20, pp. 1205–1209, 1968.
- [15] SNO Collab., “Combined Analysis of all Three Phases of Solar Neutrino Data from the Sudbury Neutrino Observatory,” *arXiv*, 2011, arXiv:1109.0763v1 [nucl-ex].
- [16] B. Pontecorvo, “Electron and muon neutrinos,” 1959, zhETF 37.

- [17] F. P. An *et al.*, “Observation of Electron-Antineutrino Disappearance at Daya Bay,” *Phys. Rev. Lett.*, vol. 108, p. 171803, 2012. [Online]. Available: <http://link.aps.org/doi/10.1103/PhysRevLett.108.171803>
- [18] RENO Collaboration, “Observation of Reactor Electron Antineutrino Disappearance in the RENO Experiment,” *arXiv*, (2012), (submitted).
- [19] J. Angrik *et al.*, “KATRIN Design Report,” 2004, FZKA-7090.
- [20] R. S. H. G. Hinshaw, J. L. Weiland, “Five-Year Wilkinson Microwave Anisotropy Probe (WMAP1) Observations: Data Processing, Sky Maps, & Basic Results,” *Astrophysical Journal*, vol. 180, 2009.
- [21] K. Abazajian *et al.*, “The seventh data release of the Sloan Digital Sky Survey,” *Astrophys. Journal Suppl. Series*, vol. 182, pp. 543–558, 2008.
- [22] A. Riess *et al.*, “A Redetermination of the Hubble Constant with the Hubble Space Telescope from a Differential Distance Ladder,” *Astrophys. Journal*, vol. 699, pp. 539–563, 2009.
- [23] J. Schwarz, *Design zur Messung der elektro-optischen Eigenschaften der differentiellen Pumpstrecke DPS2-F des KATRIN-Experiments*, 2010, Diploma thesis, Karlsruhe Institute of Technology.
- [24] T. Kirsten and H. Müller, “Observation of ^{82}Se double-beta decay in selenium ores,” *Earth and Plan. Science Lett.* 4, vol. 6, pp. 271–274, 1969. [Online]. Available: [http://dx.doi.org/10.1016/0012-821X\(69\)90167-8](http://dx.doi.org/10.1016/0012-821X(69)90167-8)
- [25] S. Schonert *et al.*, “The GERmanium Detector Array (GERDA) for the search of neutrinoless beta beta decays of Ge-76 at LNGS,” *Nucl. Phys. Proc. Suppl.*, vol. 145, pp. 242–245, 2005.
- [26] The Majorana Collab., “The Majorana Ge-76 Double-Beta Decay Project,” *arXiv*, p. 051301, 2002. [Online]. Available: <http://arxiv.org/abs/hep-ex/0201021>
- [27] K. S. Hirata *et al.*, “Observation in the Kamiokande-II Detector of the Neutrino Burst from Supernova SN 1987a,” *Phys. Rev.*, vol. D38, pp. 448–458, 1988.
- [28] R. M. Bionta *et al.*, “Observation of a Neutrino Burst in Coincidence with Supernova SN 1987a in the Large Magellanic Cloud,” *Phys. Rev. Lett.*, vol. 58, p. 1494, 1987.
- [29] E. N. Alexeyev and L. N. Alexeyeva, “Detection of a Neutrino Signal from SN 1987A on february 23, 1987 at 7:35 UT: Data from the Baksan Underground Scintillation Telescope,” *Astr. Lett.* 11, vol. 34, pp. 745–752, 2008.
- [30] T. J. Loredo and D. Q. Lamb, “Bayesian analysis of neutrinos observed from supernova SN1987A,” *Phys. Rev.*, vol. D65, p. 063002, 2002.
- [31] K. Assamagan *et al.*, “Upper limit of the muon-neutrino mass and charged-pion mass from momentum analysis of a surface muon beam,” *Phys. Rev.* 11, vol. 53, 1996.
- [32] R. Barate *et al.*, “An upper limit on the τ neutrino mass from three- and five-prong tau decays,” *Europ. Phys. Journal C* 3, vol. 2, 1998.
- [33] C. Arnaboldi *et al.*, “Bolometric bounds on the anti-neutrino mass,” *Phys. Rev. Lett.*, vol. 91, p. 161802, 2003.
- [34] E. Andreotti *et al.*, “MARE, Microcalorimeter Arrays for a Rhenium Experiment: A detector overview,” *Nucl. Instr. and Meth. in Phys. Res. A*, vol. 572, pp. 208–210, 2007.

- [35] F. Gatti *et al.*, *MARE, Microcalorimeter Arrays for a Rhenium Experiment*, 2006. [Online]. Available: http://crio.mib.infn.it/wig/silicini/proposal/proposal_MARE_v2.6.pdf
- [36] E. W. Otten and C. Weinheimer, “Neutrino mass limit from tritium beta decay,” *Rept. Prog. Phys.*, vol. 71, pp. 086–201, 2008.
- [37] V. M. Lobashev *et al.*, “Direct search for mass of neutrino and anomaly in the tritium beta-spectrum,” *Phys. Lett. B*, vol. 460, pp. 227–235, 1999.
- [38] C. Kraus *et al.*, “Final results from phase II of the Mainz neutrino mass search in tritium β decay,” *European Physical Journal C*, vol. 40, p. 447, 2005. [Online]. Available: doi:10.1140/epjc/s2005-02139-7
- [39] W. Käfer *et al.*, “Monitoring of the properties of the KATRIN Windowless Gaseous Tritium Source,” 2012, submitted to New Journal of Physics. [Online]. Available: <http://arxiv.org/abs/1205.5421v1>
- [40] S. Fischer *et al.*, “Monitoring of Tritium Purity During Long-Term Circulation in the KATRIN Test Experiment LOOPINO Using Laser Raman Spectroscopy,” *Fusion Science and Technology*, vol. 60, no. 3, pp. 925–930, 2011.
- [41] S. Grohmann *et al.*, “Cryogenic Design of the KATRIN Source Cryostat,” *AIP Conf. Proc.*, vol. 985, pp. 1277 – 1287, 2008.
- [42] S. Lukic *et al.*, “Measurement of the gas-flow reduction factor of the KATRIN DPS2-F differential pumping section,” *Vacuum - Surface Eng., Surface Instr. and Vacuum Techn.*, vol. 86, pp. 1126 – 1133, 2012.
- [43] F. Eichelhardt *et al.*, “First Tritium Results of the KATRIN Test Experiment TRAP,” *Fusion Science and Technology*, vol. 54, p. 615, 2008.
- [44] W. Gil *et al.*, “The Cryogenic Pumping Section of the katrin Experiment,” *IEEE Trans. on app. supercond. 3*, vol. 20, pp. 316 – 319, 2010.
- [45] V. Lobashev and P. Spivak, “A Method for Measuring the Electron Antineutrino Rest Mass,” *Nucl. Inst. and Meth. in Phys. Res.*, vol. A240, pp. 305 – 310, 1985.
- [46] F. Fraenkle *et al.*, “Radon induced background processes in the KATRIN pre-spectrometer,” *Astroparticle Phys. Issue 3*, vol. 35, pp. 128 – 134, 2011.
- [47] S. Bauer, *Aufbau und Inbetriebnahme des zweiten Präzisions-Hochspannungsteilers bis 65 kV für das KATRIN-Experiment*, 2010, diploma thesis, Westfälische Wilhelms-Universität Münster.
- [48] M. Zbořil, *Vacuum Stability of $^{83}\text{Rb}/^{83m}\text{Kr}$ Electron Source for the Neutrino Experiment KATRIN*, 2006, Diploma thesis, Czech Technical University in Prague.
- [49] P. Doe *et al.*, “Neutrino research,” *Annual Report of the Center for Experimental Nuclear Physics and Astrophysics, University of Washington*, pp. 1 – 1
- [50] N. Wermes *et al.*, “New Results on DEPFET Pixel Detectors for Radiation Imaging and High Energy Particle Detection,” *IEEE Transactions on Nuclear Science*, vol. 51, no. 3, pp. 1121–1128, 2004.
- [51] F. Bloch, “Ueber die Quantenmechanik der Elektronen in Kristallgittern,” *Zeitschrift für Physik A Hadrons and Nuclei*, vol. 7-8, pp. 555 – 600, 1929.
- [52] S. Sze and K. Kwok, *Physics of Semiconductor Devices 3rd ed.* John Wiley & Sons Inc., 2007.

- [53] G. Knoll, *Radiation Detection and Measurement 4th ed.* John Wiley & Sons Inc., 2010.
- [54] B. VanDevender *et al.*, “Performance of a TiN-coated monolithic silicon pin-diode array under mechanical stress,” *Nucl. Inst. and Meth. in Phys. Res. A*, vol. 673, pp. 46 – 50, 2012.
- [55] O. Evrard *et al.*, “A novel photodiode array structure for gamma camera applications,” *Nucl. Instr. and Meth. in Phys. Res. A*, vol. 504, pp. 188 – 195, 2003.
- [56] P. Renschler, *KESS - A new Monte Carlo simulation code for low-energy electron interactions in silicon detectors*, 2011, dissertation, Karlsruhe Institute of Technology.
- [57] Hamamatsu Photonics K.K., Solid State Devision, *MPPC Catalogue*, 2009.
- [58] Hamamatsu Photonics K.K., Solid State Devision, *Manual for the S10362-11 series MPPC*, 2009.
- [59] J. Formaggio *et al.*, *Kassiopieia Users Guide 1.50*, Kassiopieia development group, KATRIN internal document.
- [60] K. Goto *et al.*, “True Auger spectral shapes: A step to standard spectra,” *Surface and Interface Analysis*, vol. 22, pp. 75–78, 1994.
- [61] J. Allison *et al.*, “Geant4 developments and applications,” *IEEE Transactions on Nuclear Science*, vol. 53/1, 2006.
- [62] F. Salvat, J. Fernández-Varea, and J. Sempau, *PENELOPE-2008: A Code System for Monte Carlo Simulation of Electron and Photon Transport*, 2008.
- [63] F. Salvat, A. Jablonski, and C. J. Powell, “ELSEPA Dirac partial-wave calculation of elastic scattering of electrons and positrons by atoms, positive ions and molecules,” *Comput. Phys. Commun.*, vol. 165, pp. 157–190, 2005.
- [64] D. R. Penn, “Electron mean-free-path calculations using a model dielectric function,” *Phys. Rev. B*, vol. 35, pp. 482–486, 1987.
- [65] P. Doe *et al.*, *Optimization Criterion for the Signal and Background in the KATRIN Focal-Plane Detector*, 2008, kATRIN Internal Documentation.
- [66] J. Fischer, *Entwicklung von Monitoring Tools für den KATRIN Pinch Magneten*, 2012, Bachelor Arbeit in Vorbereitung, Karlsruhe Institut of Technology.
- [67] J. Amsbaugh, *Detector Vacuum System - Users guide*, 2011, Internal documentation, CENPA, University of Washington, Seattle.
- [68] S. Wuestling, *KATRIN Main Detector (Focal Plane Detector) Electronics Design Description*, 2011, KATRIN internal documentation.
- [69] M. Kleifges, “The fluorescene detector electronics of the pierre auger observatory,” *Nucl. Inst. and Meth. in Phys. Res. A*, vol. 518, pp. 180–182, 2004.
- [70] A. Kopmann *et al.*, “FPGA-Based DAQ System for Multi-Channel Detectors,” *IEEE Nucl. Sci. Symposium Conference Record*, pp. 3186 – 3190, 2008.
- [71] M. Howe *et al.*, “Sudbury Neutrino Observatory Neutral Current Detector Acquisition Software Overview,” *IEEE Trans. Nucl. Sci.*, vol. 51, pp. 878–883, 2004.
- [72] R. Brun *et al.*, *Root Users Guide 5.26*, CERN, 2009, <http://root.cern.ch/>.
- [73] C. H. Lefhalm and V. Krieger, “A Full Featured Monitoring, Control and Data Management System for Liquid Metal Coolant Loops,” *Real Time Conference, 14th IEEE-NPSS*, pp. 570–573, 2005.

- [74] M. Steidl, *Manual for using the FPD Gamma Ray Source*, 2011, KATRIN internal manual.
- [75] J. Barrett, *Memorandum on Optics System for Photoelectron Production*, 2011, internal documentation, KATRIN Collaboration.
- [76] E. Martin, *Electron Source Users Manual*, 2011, internal documentation, CENPA, University of Washington, Seattle.
- [77] D. Peterson *et al.*, *Optical pulser for KATRIN focal plane detector*, 2012, Internal documentation, CENPA, University of Washington, Seattle.
- [78] Y. Akovali, “241am decay from 1994-98 (nsr),” *NDS 72,191*, 1994. [Online]. Available: <http://ie.lbl.gov/toi/nuclide.asp?iZA=950241>
- [79] G. Drexlin and F. Fraenkle, *Background from the titanium plate*, 2012, KATRIN internal communication.
- [80] A. Thompson *et al.*, *X-ray data booklet*. Center for X-ray optics and advanced light source, Lawrence Berkeley National Laboratory, 2009.
- [81] F. Salvat *et al.*, *PENELOPE-A code system for Monte Carlo simulations of electron and photon transport*, 2001, OECD Nuclear Energy Agency, Issy-les-Moulineaux, France.
- [82] N. Gagunashvili, “Comparison of weighted and unweighted histograms,” *Proceed. of Sience (ACAT)*, vol. 54, 2007. [Online]. Available: <http://arxiv.org/pdf/physics/0605123.pdf>
- [83] D. Scott, “On optimal and data-based histograms,” *Biometrika*, vol. 66 (3), pp. 605 – 610, 1979.

Appendix

A. Measurement Tables

Table A.1.: **Voltage Settings of the Linearity Measurements.** Note the difference between the set point voltages in column one and the actual measured voltages in column two (with statistical uncertainties).

Voltage Set Point in mV	Measured Voltage in mV
300	115 ± 1
350	132 ± 1
400	150 ± 2
450	170 ± 2
500	185 ± 2
550	210 ± 2
600	222 ± 2
650	240 ± 2
700	260 ± 2
750	276 ± 2
800	295 ± 2
850	312 ± 2
900	330 ± 2
950	347 ± 5
1000	375 ± 5
1100	420 ± 5
1200	445 ± 5
1300	487 ± 5
1400	522 ± 5
1500	560 ± 5
1600	597 ± 5
1700	640 ± 5
1800	680 ± 5
1900	695 ± 10
1000	372 ± 5

Table A.2.: Energy Calibration Results with the ^{241}Am Source. In the second and third column the energy calibration results used in most of the analyses are shown per pixel with statistical uncertainties whereas in column four and five the calibration data used in the dead-layer analysis is listed per pixel with statistical uncertainties. The ADC-to-energy conversion factor is denoted as C.

Pixel	Usual Calibration Data		Dead Layer Calibration Data	
	C in eV/ADC	FWHM in keV	C in eV/ADC	FWHM in keV
0	99.60 ± 0.03	1.42 ± 0.03	-	-
1	99.62 ± 0.03	1.51 ± 0.03	-	-
2	97.61 ± 0.03	1.53 ± 0.03	-	-
3	99.99 ± 0.03	1.50 ± 0.03	-	-
4	99.36 ± 0.03	1.51 ± 0.03	99.82 ± 0.06	1.54 ± 0.07
5	99.22 ± 0.03	1.45 ± 0.03	99.65 ± 0.05	1.45 ± 0.06
6	100.22 ± 0.03	1.59 ± 0.03	100.42 ± 0.05	1.47 ± 0.05
7	100.23 ± 0.03	1.52 ± 0.03	100.10 ± 0.06	1.52 ± 0.07
8	100.32 ± 0.03	1.45 ± 0.03	100.49 ± 0.05	1.40 ± 0.05
9	98.20 ± 0.03	1.56 ± 0.04	98.71 ± 0.07	1.88 ± 0.08
10	-	-	-	-
11	-	-	-	-
12	98.20 ± 0.03	1.59 ± 0.03	99.57 ± 0.07	1.91 ± 0.11
13	99.24 ± 0.03	1.58 ± 0.03	99.24 ± 0.05	1.49 ± 0.07
14	99.77 ± 0.03	1.63 ± 0.04	100.08 ± 0.06	1.66 ± 0.07
15	99.63 ± 0.03	1.53 ± 0.03	100.08 ± 0.05	1.44 ± 0.06
16	98.46 ± 0.03	1.58 ± 0.03	98.70 ± 0.06	1.47 ± 0.07
17	101.45 ± 0.03	1.55 ± 0.03	100.51 ± 0.07	1.72 ± 0.09
18	100.01 ± 0.03	1.53 ± 0.03	100.03 ± 0.05	1.41 ± 0.05
19	99.18 ± 0.03	1.53 ± 0.03	99.76 ± 0.05	1.34 ± 0.05
20	98.65 ± 0.03	1.54 ± 0.03	99.25 ± 0.05	1.38 ± 0.06
21	99.16 ± 0.03	1.58 ± 0.04	99.43 ± 0.06	1.55 ± 0.06
22	99.45 ± 0.07	3.13 ± 0.09	-	-
23	98.60 ± 0.03	1.54 ± 0.03	98.12 ± 0.05	1.54 ± 0.07
24	99.70 ± 0.03	1.64 ± 0.04	100.00 ± 0.06	1.66 ± 0.07
25	101.48 ± 0.03	1.71 ± 0.04	101.80 ± 0.07	1.85 ± 0.08
26	98.04 ± 0.03	1.49 ± 0.03	98.46 ± 0.05	1.33 ± 0.07
27	98.48 ± 0.03	1.57 ± 0.03	98.64 ± 0.06	1.58 ± 0.07
28	97.98 ± 0.03	1.55 ± 0.03	98.02 ± 0.05	1.43 ± 0.06
29	99.30 ± 0.03	1.47 ± 0.03	99.56 ± 0.05	1.49 ± 0.06
30	99.47 ± 0.03	1.55 ± 0.03	99.68 ± 0.05	1.56 ± 0.07
31	99.46 ± 0.03	1.54 ± 0.03	99.53 ± 0.06	1.46 ± 0.07
32	-	-	-	-
33	98.20 ± 0.03	1.54 ± 0.03	98.53 ± 0.05	1.51 ± 0.06
34	-	-	-	-
35	-	-	-	-
36	100.30 ± 0.03	1.56 ± 0.03	100.57 ± 0.06	1.51 ± 0.07
37	97.59 ± 0.03	1.58 ± 0.03	97.80 ± 0.05	1.57 ± 0.07
38	97.95 ± 0.03	1.64 ± 0.04	98.11 ± 0.05	1.51 ± 0.07
39	98.66 ± 0.03	1.54 ± 0.04	99.06 ± 0.06	1.56 ± 0.07
40	99.06 ± 0.03	1.56 ± 0.03	99.02 ± 0.05	1.44 ± 0.06

Pixel	Usual Calibration Data		Dead Layer Calibration Data	
	C in eV/ADC	FWHM in keV	C in eV/ADC	FWHM in keV
41	99.85 ± 0.03	1.51 ± 0.03	99.70 ± 0.06	1.55 ± 0.07
42	100.46 ± 0.03	1.52 ± 0.03	99.38 ± 0.06	1.44 ± 0.06
43	100.23 ± 0.03	1.84 ± 0.04	100.17 ± 0.06	1.77 ± 0.07
44	-	-	-	-
45	-	-	-	-
46	99.55 ± 0.03	1.56 ± 0.03	99.82 ± 0.05	1.50 ± 0.06
47	97.11 ± 0.03	1.67 ± 0.04	97.55 ± 0.06	1.59 ± 0.07
48	98.50 ± 0.03	1.70 ± 0.04	98.38 ± 0.05	1.49 ± 0.06
49	101.18 ± 0.03	1.63 ± 0.03	101.59 ± 0.06	1.66 ± 0.09
50	98.94 ± 0.03	1.53 ± 0.03	99.41 ± 0.06	1.58 ± 0.07
51	98.78 ± 0.03	1.43 ± 0.03	99.25 ± 0.05	1.48 ± 0.06
52	99.63 ± 0.03	1.56 ± 0.03	99.99 ± 0.06	1.62 ± 0.07
53	98.91 ± 0.03	1.54 ± 0.03	99.57 ± 0.05	1.59 ± 0.06
54	98.51 ± 0.03	1.60 ± 0.03	98.36 ± 0.05	1.49 ± 0.06
55	99.89 ± 0.03	1.59 ± 0.03	99.65 ± 0.06	1.49 ± 0.07
56	102.27 ± 0.03	1.55 ± 0.03	100.65 ± 0.05	1.52 ± 0.07
57	98.25 ± 0.03	1.56 ± 0.03	98.73 ± 0.06	1.63 ± 0.07
58	-	-	-	-
59	99.57 ± 0.03	1.59 ± 0.03	99.93 ± 0.05	1.55 ± 0.07
60	98.17 ± 0.03	1.78 ± 0.04	97.88 ± 0.06	1.62 ± 0.07
61	101.27 ± 0.03	1.64 ± 0.04	101.17 ± 0.06	1.48 ± 0.06
62	98.72 ± 0.03	1.56 ± 0.03	98.89 ± 0.05	1.51 ± 0.06
63	98.22 ± 0.03	1.60 ± 0.03	98.53 ± 0.05	1.51 ± 0.06
64	100.01 ± 0.03	1.51 ± 0.03	100.29 ± 0.06	1.45 ± 0.07
65	98.63 ± 0.03	1.62 ± 0.04	98.38 ± 0.05	1.52 ± 0.07
66	101.03 ± 0.03	1.49 ± 0.03	99.62 ± 0.06	1.59 ± 0.07
67	-	-	-	-
68	-	-	-	-
69	100.69 ± 0.03	1.68 ± 0.03	101.06 ± 0.06	1.64 ± 0.07
70	99.24 ± 0.03	1.54 ± 0.03	99.32 ± 0.05	1.46 ± 0.06
71	99.66 ± 0.03	1.58 ± 0.04	99.44 ± 0.06	1.66 ± 0.06
72	98.36 ± 0.03	1.67 ± 0.04	98.98 ± 0.06	1.85 ± 0.07
73	97.76 ± 0.03	1.64 ± 0.03	97.91 ± 0.06	1.64 ± 0.07
74	98.46 ± 0.03	1.60 ± 0.03	98.54 ± 0.05	1.53 ± 0.06
75	98.69 ± 0.03	1.59 ± 0.04	98.97 ± 0.05	1.51 ± 0.07
76	100.20 ± 0.03	1.56 ± 0.03	100.44 ± 0.06	1.54 ± 0.07
77	98.84 ± 0.03	1.51 ± 0.03	99.97 ± 0.05	1.42 ± 0.06
78	100.39 ± 0.03	1.63 ± 0.03	100.53 ± 0.05	1.48 ± 0.06
79	98.13 ± 0.03	1.61 ± 0.03	98.09 ± 0.06	1.61 ± 0.07
80	-	-	-	-
81	96.95 ± 0.03	1.64 ± 0.04	97.37 ± 0.06	1.72 ± 0.08
82	-	-	-	-
83	97.02 ± 0.03	1.54 ± 0.03	97.53 ± 0.06	1.60 ± 0.06
84	97.34 ± 0.03	1.70 ± 0.04	97.56 ± 0.06	1.58 ± 0.07
85	101.36 ± 0.03	1.63 ± 0.04	101.63 ± 0.06	1.60 ± 0.06
86	101.04 ± 0.03	1.68 ± 0.04	101.30 ± 0.06	1.63 ± 0.08
87	98.41 ± 0.03	1.60 ± 0.03	99.04 ± 0.06	1.60 ± 0.07
88	98.19 ± 0.03	1.68 ± 0.04	98.50 ± 0.06	1.56 ± 0.06
89	100.19 ± 0.03	1.58 ± 0.03	100.13 ± 0.06	1.61 ± 0.06

Pixel	Usual Calibration Data		Dead Layer Calibration Data	
	C in eV/ADC	FWHM in keV	C in eV/ADC	FWHM in keV
90	99.55 ± 0.03	1.53 ± 0.03	100.07 ± 0.05	1.54 ± 0.06
91	100.79 ± 0.03	1.66 ± 0.04	101.16 ± 0.06	1.57 ± 0.07
92	-	-	-	-
93	-	-	-	-
94	97.82 ± 0.03	1.74 ± 0.04	98.54 ± 0.06	1.60 ± 0.07
95	97.53 ± 0.03	1.67 ± 0.03	97.53 ± 0.06	1.57 ± 0.07
96	98.70 ± 0.03	1.77 ± 0.04	98.91 ± 0.06	1.62 ± 0.06
97	100.36 ± 0.03	1.65 ± 0.03	100.95 ± 0.07	1.85 ± 0.09
98	99.21 ± 0.03	1.59 ± 0.04	99.40 ± 0.06	1.70 ± 0.07
99	98.89 ± 0.03	1.54 ± 0.03	99.44 ± 0.06	1.54 ± 0.06
100	98.37 ± 0.03	1.61 ± 0.04	98.71 ± 0.06	1.65 ± 0.07
101	98.40 ± 0.03	1.49 ± 0.03	98.53 ± 0.05	1.32 ± 0.05
102	96.94 ± 0.03	1.66 ± 0.03	97.34 ± 0.06	1.67 ± 0.08
103	98.68 ± 0.03	1.61 ± 0.03	98.78 ± 0.05	1.55 ± 0.07
104	99.27 ± 0.03	1.49 ± 0.03	98.81 ± 0.05	1.40 ± 0.07
105	100.18 ± 0.03	1.70 ± 0.03	100.41 ± 0.06	1.74 ± 0.08
106	-	-	-	-
107	99.59 ± 0.03	1.66 ± 0.04	99.21 ± 0.06	1.66 ± 0.06
108	97.17 ± 0.03	1.74 ± 0.04	98.43 ± 0.06	1.67 ± 0.07
109	97.36 ± 0.03	1.69 ± 0.04	97.70 ± 0.06	1.70 ± 0.08
110	98.47 ± 0.03	1.62 ± 0.03	98.67 ± 0.06	1.71 ± 0.08
111	99.62 ± 0.03	1.74 ± 0.04	99.89 ± 0.06	1.56 ± 0.07
112	99.97 ± 0.03	1.65 ± 0.03	100.32 ± 0.06	1.75 ± 0.08
113	98.92 ± 0.03	1.78 ± 0.04	98.90 ± 0.06	1.74 ± 0.08
114	98.61 ± 0.03	1.60 ± 0.04	98.90 ± 0.05	1.51 ± 0.07
115	98.65 ± 0.03	1.56 ± 0.04	98.65 ± 0.06	1.58 ± 0.07
116	-	-	-	-
117	-	-	-	-
118	98.46 ± 0.03	1.66 ± 0.04	98.83 ± 0.07	1.80 ± 0.08
119	100.02 ± 0.03	1.72 ± 0.04	100.32 ± 0.06	1.62 ± 0.07
120	97.40 ± 0.03	1.76 ± 0.04	97.98 ± 0.06	1.79 ± 0.08
121	98.28 ± 0.03	1.77 ± 0.04	98.83 ± 0.06	1.63 ± 0.08
122	97.84 ± 0.03	1.59 ± 0.03	98.36 ± 0.06	1.73 ± 0.08
123	99.60 ± 0.03	1.65 ± 0.04	99.69 ± 0.06	1.54 ± 0.07
124	98.91 ± 0.03	1.64 ± 0.04	99.24 ± 0.06	1.55 ± 0.07
125	100.16 ± 0.03	1.47 ± 0.03	100.78 ± 0.05	1.46 ± 0.07
126	99.91 ± 0.03	1.69 ± 0.04	100.12 ± 0.06	1.52 ± 0.07
127	99.04 ± 0.03	1.65 ± 0.04	99.18 ± 0.06	1.62 ± 0.08
128	99.33 ± 0.03	1.63 ± 0.04	99.34 ± 0.06	1.64 ± 0.08
129	100.87 ± 0.03	1.64 ± 0.04	101.18 ± 0.06	1.64 ± 0.06
130	-	-	-	-
131	98.83 ± 0.03	1.72 ± 0.04	99.21 ± 0.06	1.61 ± 0.08
132	100.03 ± 0.03	1.70 ± 0.04	98.90 ± 0.07	1.76 ± 0.07
133	99.11 ± 0.04	1.75 ± 0.04	99.56 ± 0.07	1.74 ± 0.08
134	97.12 ± 0.03	1.74 ± 0.04	97.30 ± 0.07	1.85 ± 0.09
135	97.74 ± 0.03	1.67 ± 0.04	99.63 ± 0.06	1.73 ± 0.07
136	99.70 ± 0.03	1.76 ± 0.04	99.93 ± 0.05	1.51 ± 0.07
137	98.44 ± 0.03	1.71 ± 0.04	98.96 ± 0.06	1.76 ± 0.07
138	98.12 ± 0.03	1.63 ± 0.04	98.45 ± 0.06	1.75 ± 0.07

Pixel	Usual Calibration Data		Dead Layer Calibration Data	
	C in eV/ADC	FWHM in keV	C in eV/ADC	FWHM in keV
139	98.14 ± 0.03	1.59 ± 0.04	98.34 ± 0.06	1.57 ± 0.07
140	99.79 ± 0.03	1.80 ± 0.04	100.02 ± 0.06	1.62 ± 0.08
141	-	-	-	-
142	100.02 ± 0.03	1.72 ± 0.04	101.04 ± 0.07	1.78 ± 0.08
143	96.56 ± 0.03	1.83 ± 0.04	97.30 ± 0.06	1.63 ± 0.07
144	100.01 ± 0.04	1.91 ± 0.05	100.19 ± 0.06	1.81 ± 0.07
145	98.13 ± 0.04	1.95 ± 0.05	98.44 ± 0.07	2.01 ± 0.08
146	99.38 ± 0.03	1.74 ± 0.04	99.81 ± 0.07	1.85 ± 0.09
147	99.16 ± 0.03	1.61 ± 0.04	99.78 ± 0.06	1.66 ± 0.06

Table A.3.: **Dead-Layer Results per Pixel.** Pixels without an entry have either not enough statistics for a dead-layer analysis or they are affected strongly by systematics and are therefore excluded. The values are a combination of the results from all analyses of energies between 9 keV and 17 keV.

Pixel	Dead Layer in nm
0	-
1	-
2	-
3	-
4	129.9 ^{+5.3} _{-5.0} (stat.) ^{+0.9} _{-4.8} (syst.)
5	127.9 ^{+5.4} _{-5.1} (stat.) ^{+0.9} _{-4.8} (syst.)
6	133.5 ^{+6.4} _{-5.9} (stat.) ^{+0.9} _{-4.8} (syst.)
7	129.0 ^{+7.6} _{-6.9} (stat.) ^{+0.9} _{-4.8} (syst.)
8	120.6 ^{+7.9} _{-7.2} (stat.) ^{+0.9} _{-4.8} (syst.)
9	-
10	-
11	-
12	-
13	129.8 ^{+18.0} _{-16.4} (stat.) ^{+4.6} _{-24.8} (syst.)
14	122.8 ^{+8.0} _{-7.3} (stat.) ^{+0.9} _{-4.8} (syst.)
15	136.8 ^{+5.2} _{-4.9} (stat.) ^{+0.9} _{-4.8} (syst.)
16	130.5 ^{+4.6} _{-4.3} (stat.) ^{+0.9} _{-4.8} (syst.)
17	143.7 ^{+11.5} _{-10.6} (stat.) ^{+4.6} _{-24.8} (syst.)
18	130.2 ^{+6.6} _{-6.1} (stat.) ^{+0.9} _{-4.8} (syst.)
19	115.5 ^{+7.3} _{-6.7} (stat.) ^{+0.9} _{-4.8} (syst.)
20	-
21	-
22	-
23	-
24	-

Pixel	Dead Layer in nm
25	$116.6^{+10.8}_{-9.7}$ (stat.) $^{+0.9}_{-4.8}$ (syst.)
26	$137.6^{+4.8}_{-4.5}$ (stat.) $^{+0.9}_{-4.8}$ (syst.)
27	$134.1^{+4.4}_{-4.2}$ (stat.) $^{+0.9}_{-4.8}$ (syst.)
28	$129.7^{+3.6}_{-3.4}$ (stat.) $^{+0.9}_{-4.8}$ (syst.)
29	$124.4^{+4.8}_{-4.5}$ (stat.) $^{+0.9}_{-4.8}$ (syst.)
30	$127.5^{+6.6}_{-6.1}$ (stat.) $^{+0.9}_{-4.8}$ (syst.)
31	$124.9^{+7.3}_{-6.8}$ (stat.) $^{+0.9}_{-4.8}$ (syst.)
32	-
33	-
34	-
35	-
36	-
37	-
38	$124.3^{+7.0}_{-6.4}$ (stat.) $^{+0.9}_{-4.8}$ (syst.)
39	$135.5^{+3.9}_{-3.7}$ (stat.) $^{+0.9}_{-4.8}$ (syst.)
40	$123.7^{+3.7}_{-3.5}$ (stat.) $^{+0.9}_{-4.8}$ (syst.)
41	$125.6^{+5.5}_{-5.2}$ (stat.) $^{+0.9}_{-4.8}$ (syst.)
42	$130.7^{+13.1}_{-11.8}$ (stat.) $^{+8.5}_{-45.5}$ (syst.)
43	$127.9^{+10.1}_{-9.1}$ (stat.) $^{+0.9}_{-4.8}$ (syst.)
44	-
45	-
46	-
47	-
48	-
49	-
50	$127.2^{+4.2}_{-4.0}$ (stat.) $^{+0.9}_{-4.8}$ (syst.)
51	$126.5^{+2.9}_{-2.8}$ (stat.) $^{+0.9}_{-4.8}$ (syst.)
52	$122.4^{+3.6}_{-3.5}$ (stat.) $^{+0.9}_{-4.8}$ (syst.)
53	$118.7^{+4.9}_{-4.6}$ (stat.) $^{+0.9}_{-4.8}$ (syst.)
54	$125.9^{+6.1}_{-5.7}$ (stat.) $^{+0.9}_{-4.8}$ (syst.)
55	$128.1^{+7.2}_{-6.7}$ (stat.) $^{+0.9}_{-4.8}$ (syst.)
56	$134.0^{+30.5}_{-27.1}$ (stat.) $^{+24.1}_{-128.7}$ (syst.)
57	-
58	-
59	-
60	-
61	-
62	$120.6^{+5.2}_{-4.9}$ (stat.) $^{+0.9}_{-4.8}$ (syst.)
63	$135.1^{+2.8}_{-2.8}$ (stat.) $^{+0.9}_{-4.8}$ (syst.)
64	$126.2^{+5.6}_{-5.3}$ (stat.) $^{+0.9}_{-4.8}$ (syst.)
65	$122.9^{+5.3}_{-5.0}$ (stat.) $^{+0.9}_{-4.8}$ (syst.)

Pixel	Dead Layer in nm
66	-
67	-
68	-
69	-
70	-
71	-
72	-
73	-
74	$135.8^{+3.1}_{-3.0}$ (stat.) $^{+0.9}_{-4.8}$ (syst.)
75	$133.6^{+2.9}_{-2.8}$ (stat.) $^{+0.9}_{-4.8}$ (syst.)
76	$126.3^{+6.4}_{-5.9}$ (stat.) $^{+0.9}_{-4.8}$ (syst.)
77	$117.2^{+8.0}_{-7.4}$ (stat.) $^{+2.2}_{-11.5}$ (syst.)
78	$121.4^{+5.6}_{-5.2}$ (stat.) $^{+0.9}_{-4.8}$ (syst.)
79	$119.5^{+9.0}_{-8.1}$ (stat.) $^{+0.9}_{-4.8}$ (syst.)
80	-
81	-
82	-
83	-
84	-
85	-
86	$119.7^{+5.6}_{-5.2}$ (stat.) $^{+0.9}_{-4.8}$ (syst.)
87	$133.3^{+3.0}_{-2.9}$ (stat.) $^{+0.9}_{-4.8}$ (syst.)
88	-
89	$132.6^{+7.0}_{-6.5}$ (stat.) $^{+0.9}_{-4.8}$ (syst.)
90	$111.5^{+5.9}_{-5.5}$ (stat.) $^{+0.9}_{-4.8}$ (syst.)
91	$133.2^{+22.9}_{-20.4}$ (stat.) $^{+8.5}_{-45.5}$ (syst.)
92	-
93	-
94	-
95	-
96	-
97	-
98	$132.9^{+3.3}_{-3.2}$ (stat.) $^{+0.9}_{-4.8}$ (syst.)
99	$122.3^{+4.3}_{-4.1}$ (stat.) $^{+0.9}_{-4.8}$ (syst.)
100	-
101	-
102	$115.9^{+9.0}_{-8.2}$ (stat.) $^{+0.9}_{-4.8}$ (syst.)
103	$122.7^{+9.2}_{-8.3}$ (stat.) $^{+0.9}_{-4.8}$ (syst.)
104	$136.1^{+11.7}_{-10.6}$ (stat.) $^{+1.6}_{-8.8}$ (syst.)
105	-
106	-

Pixel	Dead Layer in nm
107	-
108	-
109	-
110	$118.8^{+5.3}_{-5.0}$ (stat.) $^{+0.9}_{-4.8}$ (syst.)
111	$132.6^{+3.3}_{-3.2}$ (stat.) $^{+0.9}_{-4.8}$ (syst.)
112	-
113	-
114	$117.6^{+3.8}_{-3.7}$ (stat.) $^{+0.9}_{-4.8}$ (syst.)
115	$124.8^{+11.0}_{-10.0}$ (stat.) $^{+1.3}_{-6.9}$ (syst.)
116	-
117	-
118	-
119	-
120	-
121	-
122	$129.1^{+3.4}_{-3.3}$ (stat.) $^{+0.9}_{-4.8}$ (syst.)
123	-
124	-
125	-
126	-
127	$117.5^{+3.6}_{-3.5}$ (stat.) $^{+0.9}_{-4.8}$ (syst.)
128	-
129	-
130	-
131	-
132	-
133	-
134	$117.8^{+5.7}_{-5.4}$ (stat.) $^{+0.9}_{-4.8}$ (syst.)
135	-
136	-
137	-
138	$112.0^{+8.5}_{-7.7}$ (stat.) $^{+0.9}_{-4.8}$ (syst.)
139	-
140	-
141	-
142	-
143	-
144	-
145	-
146	$126.9^{+4.6}_{-4.4}$ (stat.) $^{+0.9}_{-4.8}$ (syst.)
147	-

Table A.4.: **Measurements with the Electron Disc at Different Voltages** and the ramped magnets at nominal fields. In column one, the voltage set point for the electron disc is listed whereas in column two the measured voltage (from Slow Controls) is shown. The total rate on the detector can be found in column three and the number of pixels, excluded from the analysis, is listed in column four.

Voltage Set Point in kV	Measured Voltage in kV	Rate in Hz	Excluded Pixels
20	19.992	975	86
19	18.990	880	87
18.6	18.594	827	85
18	17.994	775	85
17	16.995	748	86
16	15.993	735	87
15	14.991	720	86
14	13.995	704	86
13	12.993	698	85
12	11.994	691	87
11	10.995	678	88
10	9.993	672	89
9	8.991	674	90
8	7.995	559	94
7	6.993	520	103

Table A.5.: Overview of the Excluded Pixels in the Dead-Layer Analysis at different voltage settings of the electron disc (first column). In the second column the number of pixels for which an energy calibration out of the ^{241}Am data was not possible is listed. In the third column, the number of pixels with insufficient statistics due to the inhomogeneous illumination of the electron disc is listed. The number of pixels with a high influence of the scattering in the ADC-to-energy conversion factors is listed in column four. These pixels are excluded from the dead-layer analysis as well. In the last column, the total number of excluded pixels is listed for a given voltage setting of the electron disc.

Voltage in kV	Number of Pixels Excluded in the Analysis				Total
	No Energy Calibration	Insufficient Statistics	High Systematics		
7	24	79	2		105
8	24	70	2		96
9	24	66	3		93
10	24	65	3		92
11	24	64	4		92
12	24	63	4		91
13	24	61	4		89
14	24	62	6		92
15	24	62	6		92
16	24	63	6		93
17	24	62	6		92
18	24	61	5		90
18.6	24	61	4		89
19	24	63	6		93
20	24	62	7		93

Table A.6.: Overview of the Detector-Response Simulation Settings in KESS. The simulations are performed without the tracking of secondaries inside the silicon. Their energy is deposited at their point of creation.

Parameter	Value
Lower energy limit for the simulation	100 eV
Distance from start point to detector	1 mm
Max. polar starting angle	78.4°
Detector thickness	500 μm
Detector radius	45 mm
Silicon entrance electron affinity	4.05 eV
Silicon exit electron affinity	4.05 eV
Energy of silicon conduction band minimum	0.56 eV
Simulation step size outside the detector	100 cyclotron fractions

Danksagung

Abschließend möchte ich der KATRIN Kollaboration und allen Mitarbeitern des Instituts für Kernphysik, sowie den Mitarbeitern des Tritium Labors Karlsruhe und des Instituts für Prozessdatenverarbeitung und Elektronik für ihre Hilfe und Unterstützung während des letzten Jahres danken. Es war eine spannende und sehr interessante Zeit in der ich enorm viel, auch über die experimentelle Physik hinaus, lernen konnte. Im Besonderen möchte ich hierbei folgenden Personen danken:

- Prof. Dr. Guido Drexlin, der mir die Möglichkeit gegeben hat ein Jahr lang am KATRIN Experiment mitzuwirken. Vielen Dank für die Unterstützung und die interessanten und spannenden Erfahrungen, die ich sammeln konnte.
- Prof. Dr. Günter Quast für die Zweitkorrektur dieser Arbeit.
- Dr. Markus Steidl für die sehr gute Betreuung, sowie die vielen hilfreichen Tipps und Anregungen zu dieser Arbeit.
- Prof. Dr. Peter Doe and all colleagues from the US collaboration partners, for their support and help during the assembly of the FPD system and their hints and corrections during the write-up of this thesis.
- Johannes Schwarz für die tolle Zusammenarbeit und die Beantwortung meiner vielen Fragen während des letzten Jahres.
- Dem ganzen Entwicklerteam von KASSIOPEIA/KESS/KALI für die Hilfe bei den Simulationen. Im Besonderen Stefan Groh(meister) und Marco Haag für ihre offene Art während meiner ersten Wochen in ihrem Büro.
- Bernard Bender, Luisa La Cascio, Hendrik Weingärtner, Monika Kaiser und allen anderen Ingenieuren und Technikern die uns beim Aufbau des FPD Systems unterstützt haben.
- Allen Young Scientists des KATRIN Experiments für die tolle Zeit während und außerhalb der Arbeit.

Der größte Dank geht an meine Eltern und meine Schwester, die mich während meines gesamten Studiums in allen Belangen unterstützt haben und immer für mich da waren. Sowie an meine Verlobte Verena Roßwag, die sämtliche Hochs und Tiefs meiner Studienzeit miterlebt hat und auch während meines Auslandsaufenthaltes und der stressigsten Zeiten der Diplomarbeit stets zu mir gehalten und mich unterstützt hat.